



The 11th MR in RT Symposium

CONFERENCE LOCATION

NEW YORK CITY

April 14-16, 2025

ORGANIZED BY





THE 11TH ANNUAL SYMPOSIUM ON MAGNETIC RESONANCE IN RADIATION THERAPY

Dear Colleagues,

It is our great pleasure to welcome you to the 11th MR in RT Symposium, held this year in New York City. As the role of MRI in radiotherapy continues to evolve at an extraordinary pace, this symposium provides a great opportunity to learn recent advances, exchange ideas, and brainstorm new directions for the future of MR-guided radiation therapy.

The fast-paced advancement of technology, combined with the increasing integration of MRI into clinical radiotherapy workflows, represents one of the most dynamic and challenging developments in radiation oncology. This evolution has sparked transformative changes in imaging, planning, and treatment guidance. With this scientific symposium, we aim to create a collaborative space that brings together clinicians, physicists, engineers, and researchers from across the world. Our goal is not only to showcase cutting-edge research and clinical innovation, but also to stimulate thoughtful dialogue about the continued development and consolidation of this rapidly maturing field.

We are truly excited to host you in New York City, a hub of science, culture, and energy. We look forward to engaging discussions, new collaborations, and meaningful connections that will carry beyond the symposium.

Warm regards,

The 11st MR in RT Symposium Organizing Committee

Meeting Venue and Campus Map

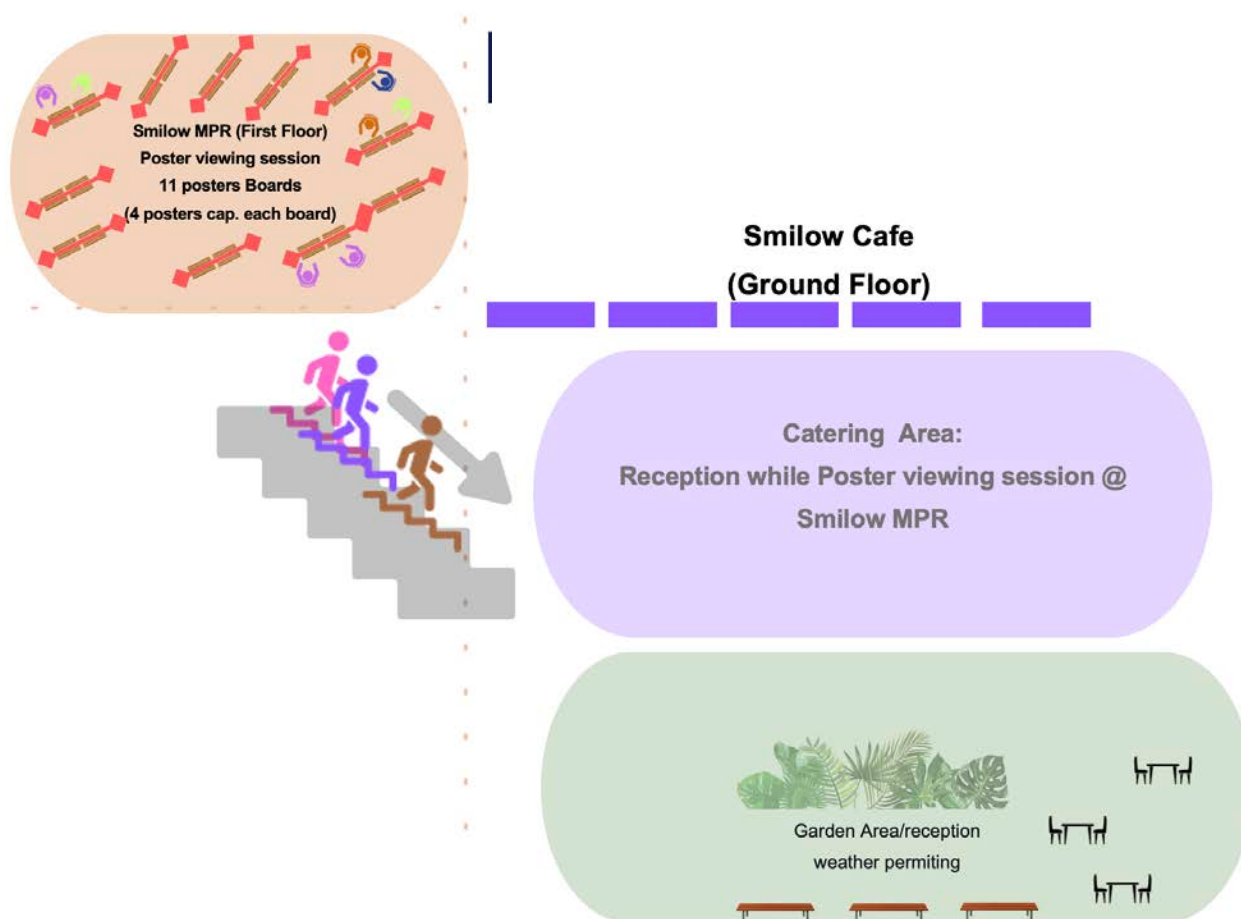


1 Security Check

2 Conference Room
Vendors Area

3 Catering
Poster Exhibition

Poster Setup and Catering Area





THE 11TH ANNUAL SYMPOSIUM ON MAGNETIC RESONANCE IN RADIATION THERAPY

Connecting to Wi-Fi at NYU Langone Health

Here's how to connect to the internet via Wi-Fi:

- **Select the Network:** On your device (laptop, tablet, or smartphone), open the Wi-Fi settings and look for the available networks. Choose the network named **NYULHguest**.
- **Accept Terms and Conditions:** Once connected to the **NYULHguest** network, open any web browser (e.g., Chrome, Safari, Firefox). You should be automatically redirected to a page displaying the terms and conditions for using the guest Wi-Fi. Carefully review these terms and then click the "Accept" or "Agree" button. After accepting the terms and conditions, you should now have internet access.
- **Assistance:** Please visit the registration table and ask the event staff for assistance.



THE 11TH ANNUAL SYMPOSIUM ON MAGNETIC RESONANCE IN RADIATION THERAPY

YOUNG INVESTIGATORS AWARD JUDGE PANEL

James Balter, PhD

University of Michigan

Eric Paulson, PhD

Medical College of Wisconsin

Rob Tijssen, PhD

Catharina Hospital, Eindhoven

David Waddington, PhD

The University of Sydney

Tufve Nyholm, PhD

Umea University

Yue Cao, PhD

University of Michigan



Elektta Unity

More than confident—certain

Elektta Unity's anatomy-specific MR imaging and uncompromised design give you the platform to transform treatment, outcomes, and efficiency.

Our market-leading Comprehensive Motion Management capabilities deliver true dose optimization and allow you to adapt therapy for every patient and every fraction, as well as increasing volume through stereotactic radiotherapy.

We help you to deliver it all from day one, through comprehensive onboarding, dedicated support and a community of your peers sharing knowledge.

Talk to us and find out how Elektta Unity empowers you to move beyond confidence and treat with certainty.

elektta.com/unity

LADMRL240206 © 2024 The Elektta Group. All rights reserved.
*Elektta Unity has CE mark and 510(k) clearance. Not available in all markets



Philips BlueSeal RT: dedicated for the needs of Radiation Oncology

PHILIPS

Learn more



C	C	K	S	M	I	E	T	N	E	M	T	A	E	R	T
A	B	R	A	I	N	N	S	Y	M	P	O	S	I	U	M
N	Y	G	O	L	O	C	N	O	N	P	E	L	V	I	S
I	N	Y	U	L	A	N	G	G	N	E	H	A	N	C	K
L	E	R	S	A	H	D	I	O	V	T	H	E	E	R	Y
R	R	A	M	P	E	Y	M	R	C	A	T	M	A	S	P
M	S	I	A	M	A	M	B	I	E	N	T	P	P	U	A
R	E	P	R	O	D	U	C	I	B	I	L	I	T	Y	R
E	N	A	T	T	A	H	N	A	M	A	L	R	O	L	E
K	O	C	S	A	N	T	I	O	R	I	I	E	N	N	H
R	I	C	P	C	D	O	N	T	H	R	F	S	I	C	T
A	T	U	E	D	N	E	N	P	M	N	C	T	E	A	O
M	C	R	E	T	E	E	R	T	S	L	L	A	W	N	I
O	A	A	D	W	C	P	R	O	S	T	A	T	E	I	D
I	R	C	I	T	K	H	B	L	U	E	S	E	A	L	A
B	F	Y	A	I	S	I	M	U	L	A	T	I	O	N	R

ACCURACY
AMBIENT
BIOMARKER
BLUSEAL
BRAIN
CENTRALPARK
EMPIRESTATE
FRACTION
HEADANDNECK
INNOVATION
LINAC
MANHATTAN
MRCAT
MRI
MRLINAC
MSKCC
NYULANGONE
ONCOLOGY
PELVIS
PHILIPS
PROSTATE
RADIOTHERAPY
REPRODUCIBILITY
SIMULATION
SMARTSPEED
SYMPORIUM
TREATMENT
WALLSTREET

--	--	--	--	--	--	--

--	--	--	--	--	--	--	--

--	--	--	--	--	--	--	--

--	--	--	--	--

--	--

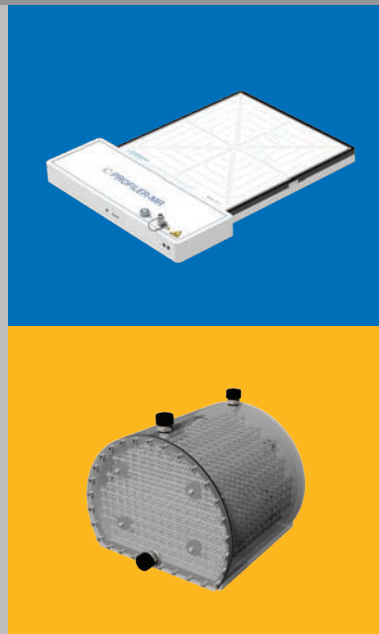
Name: _____

Hand in your solution at the Philips stand, you might be the lucky prize winner!

Comprehensive MR-Guided RT QA Solutions

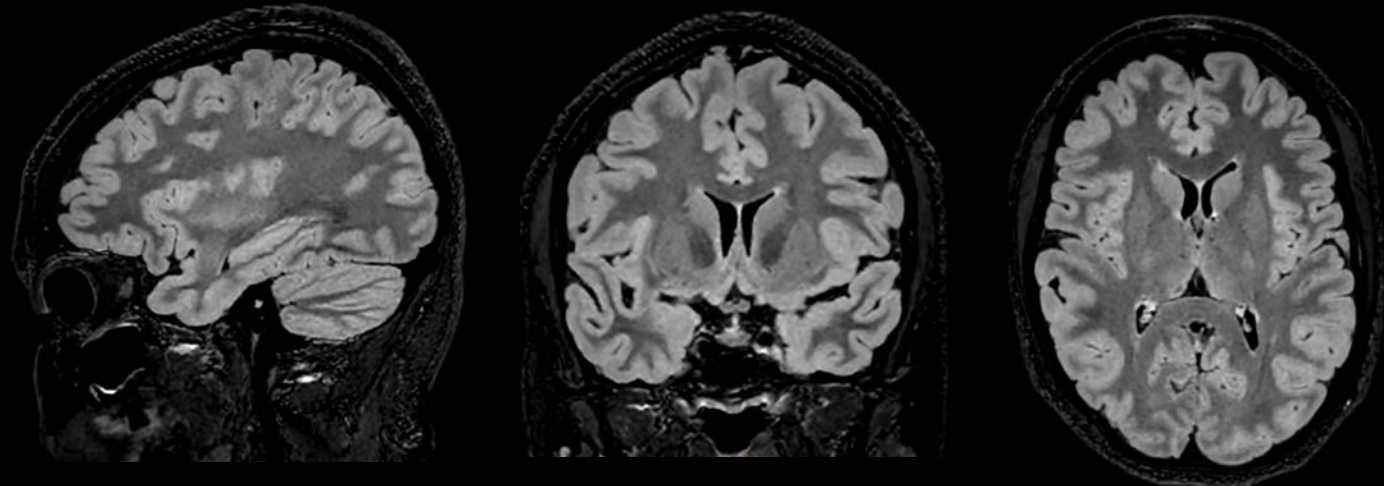
Address the unique challenges magnetic fields present with proven, efficient and effective QA solutions.

For user insights,
key publications
and product updates,
visit sunnuclear.com.





GE HealthCare



Want to learn more about GE HealthCare MR-RT solutions?

GE HealthCare advances precision health in radiation therapy

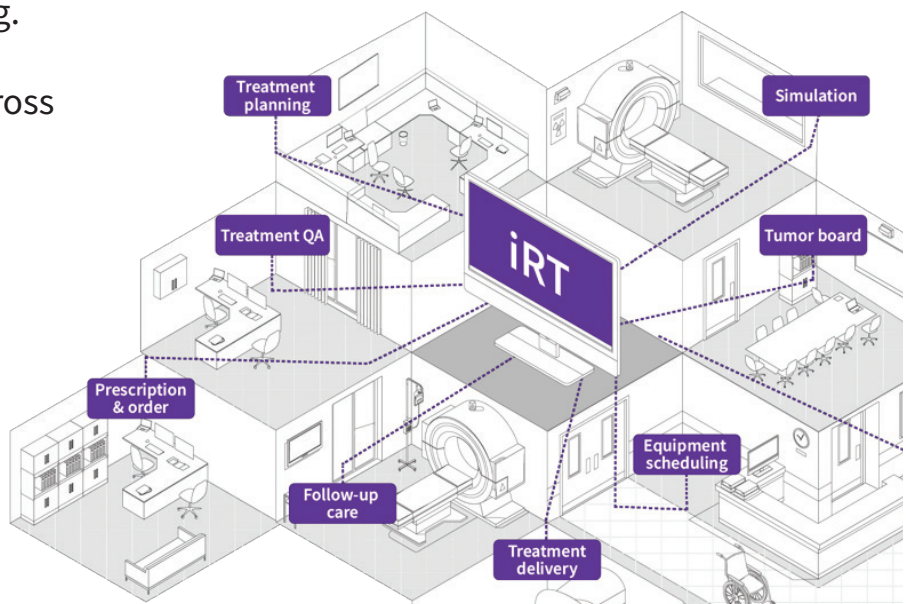
Empowering patient-centric radiation oncology with intelligent, AI-driven solutions.

GE HealthCare's AIR RT Suite and AI-powered software enhances image quality, streamlines MR simulation and treatment planning. Enables seamless care coordination—advancing precision and efficiency across radiation oncology workflows.

Scan here:



www.gehealthcare.com



MAGNETOM Free.Max RT Edition

Breaking barriers in MRI for RT

14975 0224



Detailed

MAGNETOM Free.Max RT Edition can help you take your treatment to a new level. New clinical insights await you thanks to the power of MRI.

Flexible

MAGNETOM Free.Max RT Edition allows you to perform MR imaging on your own terms. You decide who, when, and how you want to scan, thereby elevating your radiation therapy workflow.

Affordable

Installing an MR system typically requires elaborate planning, and subsequent operating costs can drain your department's budget. MAGNETOM Free.Max RT Edition, though, allows you to bring MR imaging to radiation therapy in an affordable and simple way.



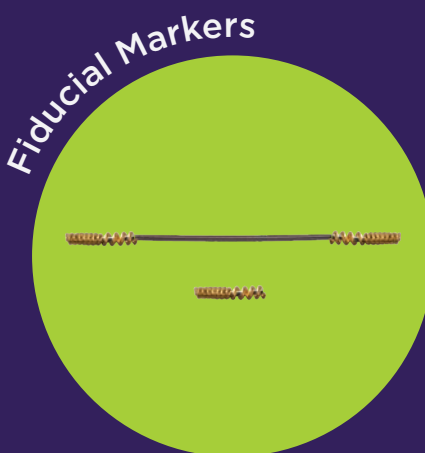
[siemens-healthineers.com/
magnetom-free-max-rt-edition](https://siemens-healthineers.com/magnetom-free-max-rt-edition)

The information shown herein refers to products of 3rd party manufacturers and thus are in their regulatory responsibility. Please contact the 3rd party manufacturer for further information.

SIEMENS
Healthineers

Simplifying MR Treatment Workflows

Discover our healthcare innovations that advance precision and enhance technology



Learn how to #CareSmarter at CQmedical.com

Copyright ©2025 CQ Medical. All rights reserved. CQ Medical is a trademark of Medtec LLC.
All products may not be licensed in accordance with Canadian law. CQCATALOG Rev.1

CQ MEDICAL®
Care Smarter

Poster Viewing session. Poster Placement Directory

Poster #. Presenter name: Title

1. **Andrew Godley:** Internal Target Volume Estimation for Liver Cancer Radiation Therapy Using an Ultra Quality 4D MRI
2. **Andrew Milewski:** Exploring respiratory-motion irregularities over 30 minutes and 1 week and enhancing external-to-internal correlation for respiratory-gated radiotherapy
3. **Ayesha Das:** Quantifying longitudinal changes in tumor habitats during radiotherapy via multiparametric MRI in a murine glioma model: Preliminary results
4. **Chiara De-Colle:** Daily adapted pancreas SBRT with target intrafraction tracking and gating by means Comprehensive Motion Management with 1.5T MR-Linac
5. **Chiara De-Colle:** Initial clinical experience of stereotactic body radiotherapy (SBRT) for liver metastases with target intrafraction tracking and gating by means Comprehensive Motion Management with 1.5T MR-Linac
6. **Chiara De-Colle:** Daily adapted prostate re-SBRT with significant PTV margin reduction and intrafraction drift checking and compensation by means of Comprehensive Motion Management
7. **Chiara De-Colle:** Implementation of T2 weighted Turbo Spin Echo MR-sequences as new pelvic protocol for Comprehensive Motion Management with 1.5T MR-linac
8. **Claire van Vliet:** MRI-guided stereotactic radiotherapy for multiple kidney tumors within a solitary kidney
9. **Cornelius Eichner:** Deep Learning Based Correction of Patient-Specific Distortions from Neuro to Uro
10. **Elodie Luge:** Real-Time Prediction of Target Displacements Using LightGBM to Mitigate MR-LINAC Latencies
11. **Emilia Persson:** Motion management in MR-guided prostate radiotherapy are the technical advancements living up to the expectations?
12. **Emilie Alvarez Andres:** DVH performance evaluation of commercially available synthetic CT for proton therapy of prostate cancer
13. **Evangelia Kaza:** Repeatability of apparent diffusion coefficient (ADC) and feasibility of diffusion-weighted prostate imaging at a 0.35T MRIdian MR-Linac.
14. **Faisal Mahmood:** Feasibility of reduced contrast dosing for MRI-guided adaptive radiotherapy in glioblastoma
15. **H Michael Gach:** FID navigator for unwrapping phase in real-time field mapping in a 0.35 T MRI-Linac
16. **Haoyang Pei:** Hybrid Learning: A Novel Combination of Self-Supervised and Supervised Learning for Joint MRI Reconstruction and Denoising without High-Quality Training Reference
17. **Huiming Dong:** 3D Wideband Late Gadolinium-Enhanced MRI for Radiotherapy of Ventricular Tachycardia: A Preliminary Study
18. **Jessica Scholey:** Clinical commissioning and validation of a deep learning-based synthetic CT algorithm for MRI-only prostate radiotherapy
19. **Jonathan Goodwin:** Deep-Learning-Enabled Segmentation of Intraprostatic Gold Fiducial Markers for MR-only Radiotherapy Planning

- 20. Jonathan Goodwin:** Computed diffusion-weighted imaging and apparent diffusion coefficient for monitoring treatment response in prostate cancer: an MR-Linac feasibility study
- 21. Joshua Kim:** Installation and Initial Evaluation of a New Low Field MR Simulator for Radiotherapy
- 22. Jue Jiang:** A large foundation models for MRI abdominal OARs segmentation
- 23. Koen Kuijter:** Patient-specific deep learning for daily adaptive MRI-guided radiotherapy of rectal cancer
- 24. Lucas McCullum:** Feasibility of Longitudinal Relaxation Rate Mapping with Non-Cartesian Sampling and Compressed Sensing on a 1.5T MR-Linac
- 25. Magali Nuixe:** Correcting k-space trajectory errors and slice profile imperfections to improve the accuracy of T1 and T2 mapping with MR fingerprinting on a 1.5 T MR-Linac
- 26. Maja Sohlin:** Enhancing accuracy and precision of IVIM estimates as imaging biomarkers for radiation therapy
- 27. Marte Kåstad Høiskar:** Deep-learning based intravoxel incoherent motion magnetic resonance imaging with fewer b-values: simulation and evaluation in head and neck cancer
- 28. Minna Lerner:** Exploring imaging biomarkers from tensor-valued diffusion-MRI for predicting treatment response in brain metastases during stereotactic radiotherapy
- 29. Minoo Gandomi:** Evaluating Geometric Distortion Correction Effects on ADC in Head and Neck Diffusion MRI: Applications in Radiotherapy
- 30. Natalia Lutsik:** MRidian Multiparametric MRI Working Group Assessment of Diff
- 31. Nima Hassan Rezaeian:** MR-Guided Adaptive Radiotherapy in Prostate Cancer Patients: Deformable Dose Accumulation and Toxicity Analysis
- 32. Patrik Brynolfsson:** Advanced denoising enables high-resolution diffusion MRI in radiotherapy
- 33. Samuel Rusu:** Beam modelling and performance evaluation of RadCalc for the Elekta Unity MRI-Linac
- 34. Silvia Fabian:** Combining CBCT-based treatment delivery with offline MRI-guided adaptive radiotherapy: a virtual MR-linear accelerator
- 35. Sirisha Tadimalla:** Quantitative MRI Biomarker Development for Personalised and Adaptive Stereotactic Body Radiation Therapy (SBRT) of Hepatocellular Carcinoma
- 36. Tanxia Qu:** Determine the isocenter and its size for MR Linac UNITY Part2: (u v) of BB and isocenter position and size
- 37. Tanxia Qu:** Determine the isocenter and its size for MR Linac UNITY Part1: (U V) of CAX
- 38. Tufve Nyholm:** Automatic segmentation of prostate and urethra on T2w MRI
- 39. Uffe Bernchou:** Balancing target dose coverage and treatment delivery efficiency during automatic beam gating in MR-guided radioablation of pancreatic tumours
- 40. Ramin Jafari:** Enhancing MRI in Radiation Therapy (RT) Applications with Deep Learning Image Reconstructions
- 41. Yu Gao:** Synthesis of 3T T2-weighted MRI from TrueFISP MRI acquired on a 0.35T MR-Linac system



THE 11TH ANNUAL SYMPOSIUM ON MAGNETIC RESONANCE IN RADIATION THERAPY

Young Investigator Award Finalist Presentations

Patient-specific imaging modality agnostic virtual digit twins modeling temporally varying digestive motion

Jorge Tapias Gomez¹, Nishant Nadkarni¹, Lando Bosma², Ergys Subashi³, William Segars⁴, James Balter⁵, Harini Veeraraghavan¹, Neelam Tyagi¹

¹Memorial Sloan Kettering Cancer Center, New York City, USA. ²Utrecht University, Utrecht, Netherlands. ³MD Anderson, Houston, USA. ⁴Duke University, Durham, USA. ⁵University of Michigan, Ann Harbor, USA

Abstract

Purpose: Develop patient-specific virtual digital twin (VDT) cohorts modeling physically realistic spatio-temporal anatomic variations of gastrointestinal organs such as the stomach and duodenum from digestive motion.

Methods: Patient-specific VDTs as 4D image sequences consisting of 14 phases modeling various GI motions were generated from patient-specific 3D static images using published analytical models of GI digestive motion. A semi-automated pipeline to incorporate user input was created that included the following steps: (a) AI generated organs (liver, stomach, duodenum, spleen, kidneys, small and large bowel, and external body) segmentation masks with visual manual verification on a reference image set (MR or CT); (b) organ-specific skeleton graph extraction performed using morphological thinning, (c) longest medial axis skeleton extraction through interactive selection of start and end points on the graph to remove branches; (d) non-uniform rational B-spline (NURBS) surface extraction; (e) multi-phase motion simulation on the NURBS surfaces using analytical models implemented as traveling waves followed by (f) extraction of deformable vector fields (DVF); and (g) creation of 4D MRI/ 4D CT sequence simulating patient-specific motion. Five datasets including 2 T2 weighted fast spin echo [T2WI FSE], 2 T1 weighted radial golden angle stack of stars [T1WI gaSOS] 4DMRI (Zhang et al., 2021), and 1 contrast-enhanced CT [CECT], were analyzed. An amplitude motion within the timescales comparable to adaptive RT planning were used to generate GI motion patterns.[\[VH1\]](#) The 3D images from phase 14 were deformably aligned to 3D images from phase 0 using multiple deformable image registration (DIR) methods, including evolution multimodality (EVO), Elastix, iterative demons, and a horn-schnuck optical flow-based (HSOF) method. The evaluation involved calculating the root-mean-squared error (RMSE) between the phase 14 DVFs produced by each DIR method and the available ground truth DVF.

Results: A travelling wave equation with an amplitude=3mm, wavelength=55mm, speed=50mm/sec were applied to all five patient scans to generate a 4D image sequence of stomach & duodenum contraction phases along with the DVFs. The average RMSE of the algorithm computed DVFs

compared to the simulated ground truth DVF_s, evaluated within the stomach and duodenum masks across all five datasets, were: HSOF=0.026mm, EVO=0.029mm, Elastix=0.037mm, and Demons=0.038mm.

Conclusion: Patient-specific digital twins along with ground truth DVF_s modeling a variety of realistic GI motion enable the creation of synthetic MRIs that can be used for validation of deformable image registrations and eventually provide training dataset for deep learning models.

Towards a clinically-relevant computational platform for systematically adapting radiation therapy for treating glioma

Hugo Miniere¹, David Hormuth¹, Ernesto Lima¹, T.J. Whitaker², Maguy Farhat², Bikash Panthi², Holly Langshaw², Mihir Shanker^{2,3}, Wasif Talpur², Sara Thrower², Jodi Goldman², Caroline Chung², Thomas Yankeelov^{1,2}

¹The University of Texas, Austin, USA. ²MD Anderson Cancer Center, Houston, USA. ³The University of Queensland, Brisbane, Australia

Abstract

Purpose: The long-term goal of this project is to optimize the spatial delivery of radiation to maximally maintain tumor control in patients with high-grade glioma. High-grade gliomas are aggressive brain tumors with poor prognoses despite an aggressive standard-of-care (SOC) chemoradiation protocol. Current guidelines for radiotherapy mandate static and uniform dose maps (2 Gy per daily fraction) that do not account for local heterogeneities and disregard areas of tumor progression over the six weeks of radiation treatment. In the present study, we seek to guide radiation delivery by using quantitative analysis of MRI data to identify highly proliferative areas of the tumor early in the course of therapy and use this knowledge to prescribe clinically relevant dose escalations to those regions. We then use mathematical modeling to simulate and compare the newly optimized treatments to the SOC.

Methods: This study involved 21 patients with high-grade gliomas treated per the Stupp protocol. Contrast-enhanced T_1 -weighed, T_2 -weighted Fluid Attenuated Inversion Recovery (FLAIR), and Diffusion-Weighted MRI are gathered at baseline and during the third week of treatment. These data are used to generate cell density maps that allow for accurately quantifying regions of high proliferation and increased cellularity. Regions experiencing a 20% or greater growth in cell count between baseline and week 3 of treatment are prescribed a dose boost up to 5 Gy per fraction. The resulting adapted dose map is then validated by a trained radiation physicist to ensure feasibility of delivery using clinically available radiation treatment systems and compliance with toxicity constraints for organs at risk. Given the adapted dose map, we then use our biology-based models which are calibrated to each individual patient to predict the spatiotemporal evolution of cell count in the contrast-enhancing and the T_2 -hyperintense non-enhancing regions on a patient-specific basis. This model is first calibrated using imaging data acquired prior to the dose adaptation time point, and is then used to predict and compare outcomes between the SOC uniform dose map, and the dose-adapted clinically validated map. Figure 1 provides an overview of the proposed adaptation pipeline.

Results: Our mathematical model shows good agreement between the predicted and measured tumor cell counts, with concordance correlation coefficients and Dice values above 0.82 and 0.84, respectively, for the entire patient cohort. Figure 2 provides an example of dose adaptation for one patient, with panel A recapitulating the dose adaptation pipeline. Model predictions of total tumor cell count are shown on panel B. Our model predicts that the dose-adapted, clinically validated map results in a 36%

decrease in total tumor cell count for this patient compared to the uniform map, one month post-therapy. The spatial distribution for each prediction is shown on panel C, demonstrating the ability of our framework to identify and successfully eliminate the targeted areas of rapid proliferation.

Conclusions: Our clinical-computational platform, integrating mathematical modeling, dose painting, and adaptive radiotherapy shows promise for practically identifying and targeting areas of progression in glioma patients, thereby increasing tumor control to maximize favorable outcomes.

Highly-Accelerated, Time-Resolved 4D Golden-Angle Radial MRI with Self-Supervised Learning

Haoyang Pei^{1,2,3}, Ding Xia⁴, Yao Wang³, Hersh Chandarana^{1,2}, Daniel K Sodickson^{1,2}, Li Feng^{1,2}

¹Bernard and Irene Schwartz Center for Biomedical Imaging, Department of Radiology, New York University Grossman School of Medicine, New York, USA. ²Center for Advanced Imaging Innovation and Research (CAI2R), Department of Radiology, New York University Grossman School of Medicine, New York, USA. ³Department of Electrical and Computer Engineering, NYU Tandon School of Engineering, New York, USA. ⁴Icahn School of Medicine at Mount Sinai, Biomedical Engineering and Imaging Institute, New York, USA

Abstract

Purpose

4D MRI is a valuable tool in MR-guided radiotherapy (MRgRT) for treating upper abdominal malignancies impacted by respiratory motion. It can be performed using two approaches: respiratory-resolved (or correlated) 4D MRI and time-resolved 4D MRI.

Respiratory-resolved 4D MRI assumes that breathing motion is pseudo-periodic and relies on an explicit motion detection step to guide data sorting for generating motion-resolved images. However, this assumption is often invalid due to the unpredictable breathing patterns commonly observed in cancer patients. In contrast, time-resolved 4D MRI offers several advantages, including greater robustness to variations in breathing patterns and the elimination of the need for an explicit motion detection step, which can be challenging to implement. However, time-resolved 4D MRI requires highly accelerated data acquisition to achieve both high spatial and temporal resolution (e.g., <1 second per volume). This remains a significant challenge, even with state-of-the-art reconstruction techniques.

This work aimed to develop a self-supervised learning-based approach for time-resolved 4D MRI reconstruction that eliminates the need for reference images, which are challenging to obtain for dynamic imaging. In addition, a low-rank subspace model-assisted training strategy is proposed to improve image reconstruction quality and accelerate training. The performance of this technique is demonstrated for highly accelerated, time-resolved 4D MRI using a novel navigator-embedded stack-of-stars (navi-stack-of-stars) golden-angle radial acquisition scheme.

Methods

Our approach builds upon the 4D Golden-angle Radial Sparse Parallel (GRASP) MRI framework, referred to as DeepGrasp. A novel navi-stack-of-stars sampling trajectory was implemented (details provided in the supporting document), where a 2D navigator is periodically acquired to enable subspace-based reconstruction. This allows for network training in a low-dimensional subspace to effectively exploit temporal correlations in 4D MRI, which not only improves reconstruction quality but also the network training speed. Dynamic image reconstruction was performed based on self-supervised training (details

outlined in the supporting document) to enable both highly-accelerated data acquisition and efficient image reconstruction.

The performance of DeepGrasp was demonstrated in highly-accelerated, free-breathing, time-resolved 4D MRI of the liver. A total of 76 4D MRI datasets were included in this study (56 datasets for training and validation, and 20 datasets for evaluation). Each dataset was acquired over 2:19 minutes, dynamic images were reconstructed with only 2 spokes for each temporal frame in each slice, resulting in 496 temporal frames with a temporal resolution of 0.28 seconds/volume. To simulate additional acceleration, all datasets were further truncated to acquisition times of 1:24 minutes and 0:56 minutes, resulting in 300 and 200 temporal frames, respectively.

Results

Representative images of time-resolved 4D MRI of the liver with a temporal resolution of 0.28 seconds are shown in the figure in the supporting document. Using DeepGrasp, time-resolved 4D MRI at this temporal resolution was achieved with an acquisition time of less than one minute.

Conclusion

This work proposes a self-supervised learning-based approach for free-breathing, time-resolved 4D MRI. Self-supervised learning plays a critical role, as fully sampled reference images cannot be acquired for conventional supervised training in time-resolved 4D MRI. This approach holds significant potential for applications in MRgRT.

A Longitudinal Study of Functional Connectivity Changes of Patients with Diffuse Glioma After Chemoradiotherapy using Aberrancy Parcel Map Analysis of Resting-state Functional MRI

Zhihua Liu¹, Kay Park², Timothy Mitchell¹, Chongliang Luo³, Joshua Shimony⁴, Robert Fucetola⁵, Abraham Snyder⁴, Jiayi Huang¹, Tong Zhu¹

¹Department of Radiation Oncology, Washington University School of Medicine, St Louis, USA.

²Department of Neurological Surgery, Washington University School of Medicine, St Louis, USA.

³Department of Surgery, Division of Medical Oncology, Washington University School of Medicine, St Louis, USA. ⁴Department of Radiology, Washington University School of Medicine, St Louis, USA.

⁵Department of Neurology, Washington University School of Medicine, St Louis, USA

Abstract

Purpose: This prospective observational study investigates aberrant changes in brain functional connectivity (FC) using resting-state functional MRI (rs-fMRI) in patients with diffuse glioma following radiotherapy (RT) compared to healthy controls. We aim to identify not only subject-specific FC disruptions but also dominant group-level disturbances that correlate with neurocognitive function (NCF) changes post-RT.

Methods: 35 adult patients (age: 48.1 ± 14.2 , Male/Female: 17/18) underwent NCF testing using the NIH Toolbox Cognitive Function Battery (NIHTB-CFB) at baseline and 6 months post-RT, specifically the five fluid cognition tests: dimension change card sort test (executive function), flanker test (attention), picture sequence test (episodic memory), list sorting test (working memory), and pattern comparison test (processing speed). The scores from the five tests are combined into an age-normalized composite score (NCF_{comp}), from which the percent change of composite (ΔNCF_{comp}) at 6 months is calculated relative to the baseline. rs-fMRI was acquired over 12 minutes on 3T MRI coinciding with the NCF tests. To quantify tumor- and treatment-induced changes in brain FC, aberrancy parcel maps (APM) were generated for each patient by comparing the pattern of FC within each of 1000 gray matter (GM) parcellations to those from 136 age- and gender-matched normal subjects through a rigorous Kolmogorov-Smirnov (KS) test. D statistical values from KS tests were adapted as aberrancy scores to quantify FC abnormalities. Larger D value indicated more FC deviations in patients compared to healthy controls. For example, the global aberrancy score computed as the mean aberrancy within GM could reveal the overall extent of FC disruption across GM.

Results: 19 patients had improved NCF at 6 months post-RT ($\Delta NCF_{comp} = 11.2\% \pm 10.4\%$), 13 had declined NCF ($\Delta NCF_{comp} = -9.8\% \pm 6.7\%$) scores and additional 3 patients either missed NCF tests or had no NCF changes. Several unique characteristics of tumor- and treatment-induced FC changes were observed from APMs. (1) Although different patients had different tumor locations, FC disruptions extended far beyond tumor regions. Among all GM regions, disruptions in central and peripheral visual network and central sensorimotor network were commonly observed among more than 80% of all patients. (2) APM captured subject-specific FC changes. Patients with tumors in similar brain regions could have quite different disruption of brain connectivity and different cognitive performances, indicating the heterogeneity of tumor and treatment effects. (3) Although not statistically

significant yet ($p=0.06$), there was a consistent trend between longitudinal changes of global aberrancy score and NCF scores post-RT: in general, patients with more areas of abnormal FC experienced more NCF decline. Group-based frequency maps of aberrancy changes showed that, for the NCF-declining group, there were more brain regions ($>20\%$) with increased FC abnormality post-RT compared to those from the NCF-improved group.

Conclusion: Aberrancy parcel maps from rs-fMRI could quantify subject-specific and global changes in brain functions among glioma patients. The global aberrancy changes in FC correlated with NCF decline post-RT, suggesting its potential as an imaging biomarker. Specifically, the extended disruption of FC in regions far from tumors, such as visual and sensorimotor networks, highlights the global impact of RT on brain functions.

Correlation of histopathological cell density and hypoxic fraction with time-dependent diffusion MRI in glioblastoma

Minea Jokivuolle^{1,2}, Henrik Lundell^{3,4}, Kristoffer Hougaard Madsen^{3,5}, Frantz Rom Poulsen^{2,6,7}, Jeanette Krogh Petersen⁸, Mads Hjordtal Grønhøj^{2,6,7}, Martin Wirenfeldt^{7,9,10}, Frederik Severin Gråe Harbo¹¹, Jesper Dupont Ewald^{2,8}, Anne Louise Højmark Bisgaard^{1,2}, Faisal Mahmood^{1,2}

¹Laboratory of Radiation Physics, Department of Oncology, Odense University Hospital, Odense, Denmark. ²Department of Clinical Research, University of Southern Denmark, Odense, Denmark.

³Danish Research Centre for Magnetic Resonance, Department of Radiology and Nuclear Medicine, Copenhagen University Hospital - Amager and Hvidovre, Hvidovre, Denmark. ⁴Department of Health Technology, Technical University of Denmark, Kongens Lyngby, Denmark. ⁵Department of Applied Mathematics and Computer Science, Technical University of Denmark, Kongens Lyngby, Denmark. ⁶Department of Neurosurgery, Odense University Hospital, Odense, Denmark. ⁷BRIDGE (Brain Research Interdisciplinary Guided Excellence), University of Southern Denmark, Odense, Denmark. ⁸Department of Pathology, Odense University Hospital, Odense, Denmark. ⁹Department of Pathology, University Hospital of Southern Denmark, Esbjerg, Denmark. ¹⁰Department of Regional Health Research, University of Southern Denmark, Odense, Denmark. ¹¹Department of Radiology, Odense University Hospital, Odense, Denmark

Abstract

Purpose

Tumor heterogeneity, such as differences in cell density and hypoxic fraction, can affect the efficacy of radiation therapy (RT). [1, 2] Imaging methods to determine tumor heterogeneity are increasingly investigated in RT. [3] The apparent diffusion coefficient (ADC) derived from diffusion-weighted MRI (DW-MRI) reflects the degree of diffusion restriction in tissue, and a low ADC has been linked to high cell density. [4, 5] Furthermore, as high cell density regions can be prone to developing hypoxia, [6] low ADC has been investigated as a surrogate measure for hypoxia. [7, 8] However, ADC can be confounded by diffusional exchange, potentially hindering the usability of ADC for tumor microstructure characterization. [9] Time-dependent diffusion MRI (TDD-MRI) utilizes time-dependent differences in the DW-MRI signal to detect both restricted diffusion and diffusional exchange, [9] potentially providing less confounded measures of tumor microstructure. The current study aims to determine the association between TDD-MRI and histopathological cell density as well as hypoxic fraction in glioblastoma.

Methods

Seven patients with glioblastoma (IDH-wildtype) were pre-operatively scanned with TDD-MRI on a 1.5 T MRI system (Ingenia, Philips HealthCare). During gross-tumor resection, 2-3 neuronavigated biopsies

with known locations in TDD-MRI were obtained per patient and histologically processed for hematoxylin and eosin (HE), and hypoxia-inducible factor 1 alpha (HIF1A) staining. Cell density and hypoxic fraction were determined from the HE and HIF1A stainings respectively using threshold-based classifiers (Visiopharm). To quantify the time-dependent diffusion (TDD) effects, we calculated *TDD contrast* by subtracting two normalized TDD-MRI signals acquired with the same b-value and two different effective diffusion times (Table 1). [10] ADC maps were calculated as voxel-wise mono-exponential fits to a DW-MRI signal. Associations between TDD contrast and the histopathological measures were determined using Spearman's rank correlation coefficient (ρ_s) with a significance level of $p < 0.025$ (Bonferroni corrected for two comparisons). For comparison, associations between ADC and the histopathological measures were also determined.

Results

Of the 18 obtained biopsies, 12 contained viable tumor tissue and were used for cell density analysis. Eight of these 12 samples expressed HIF1A and were used for hypoxia analysis. Figure 1 shows two examples of the analysed biopsy locations. The TDD contrast was more strongly coupled to cell density ($\rho_s = 0.61, p = 0.04$) than ADC ($\rho_s = -0.25, p = 0.4$), although neither of the correlations were statistically significant (Figure 2). Neither TDD contrast nor ADC showed significant correlation with the hypoxic fraction (Figure 2).

Conclusions

TDD contrast seemed to be linked to cell density more strongly than ADC. This supports the hypothesis that TDD contrast might be a less confounded measure of cell density than ADC. However, a larger sample is required to demonstrate statistical significance. There was no correlation between either TDD contrast or ADC and the hypoxic fraction. While previous research has correlated ADC to other hypoxia markers, [7, 8] HIF1A has an ambiguous reputation which could contribute to our results. [11, 12] The results show some promise for characterizing tumor microstructure based on TDD contrast on clinical MRI systems for individualized RT.

Deducing Cardiorespiratory Motion of Cardiac Substructures Using a Novel 5D-MRI Workflow for Radiotherapy

Chase Ruff^{1,2}, Tarun Naren¹, Oliver Wieben^{1,3}, Prashant Nagpal³, Kevin Johnson^{1,3}, Jiwei Zhao⁴, Carrie Glide-Hurst^{1,2}

¹University of Wisconsin-Madison, Department of Medical Physics, Madison, WI, USA. ²University of Wisconsin-Madison, Department of Human Oncology, Madison, WI, USA. ³University of Wisconsin-Madison, Department of Radiology, Madison, WI, USA. ⁴University of Wisconsin-Madison, Department of Biostatistics and Medical Informatics, Madison, WI, USA

Abstract

Purpose: A complication of thoracic radiotherapy is cardiotoxicity, where development of cardiovascular disease post-treatment is associated with cardiac substructure dose. Protecting these radiosensitive cardiac substructures is challenging due to substantial intra-fraction cardiorespiratory motion, which cannot be adequately characterized in current radiotherapy imaging protocols. We propose and validate a novel 5D-MRI workflow to decouple cardiorespiratory motion, yielding precise substructure-specific motion for radiotherapy applications.

Methods: Our 5D-MRI workflow uses a 3D, radially sampled, bSSFP free-breathing sequence, which was first optimized for 80,000 projections (TE/TR of 0.9/3.6 ms, 35° flip angle, and 40 cm FOV). Data were binned using respiratory bellows/pulse oximeter signals and reconstructed for 10 cardiac and 4 respiratory (end/active-exhale and end/active-inhale) phases via offline local low rank reconstruction to mitigate the effects of undersampling, achieving an isotropic image resolution of 1.56x1.56x1.56 mm³. Our workflow was then evaluated in a cohort of 10 healthy volunteers (23 to 65 years) including a volunteer with an LADA stent. Motion assessment was conducted for the chambers, coronary arteries, and great vessels. A geometric model was applied for the cardiac valves/conduction nodes. Contours were reviewed and verified by a cardiovascular radiologist. Centroid/bounding box displacement, 95% Hausdorff distance (HD95), and mean-distance-to-agreement (MDA) were measured between cardiorespiratory phases. Isolated cardiac motion was defined between end-diastole and end-systole, while respiratory motion was defined between end-exhale and end-inhale. Hysteresis was measured across active-exhale and active-inhale. Kruskal-Wallis tests (0.05 significance level) with Bonferroni correction/Dunn's post-hoc test were conducted between substructure pairings/groupings across 8 distance metrics (R-L/A-P/S-I/vector centroid, mean/max bounding box displacement, MDA/HD95) to quantify statistically significant differences in motion.

Results: 5D-MRI scan time for all volunteers was ~5 minutes. For cardiac motion, the coronary arteries, particularly the RCA, were most mobile, with centroid displacements >5 mm and bounding box displacements exceeding 1-2 cm. The chambers experienced centroid motion <5 mm, but bounding box displacements >5 mm, with the right ventricle/atrium having greatest excursion. Geometric regions for the mitral/tricuspid valve and AV node exhibited centroid displacements >5 mm. Cardiac motion for all

great vessels was <5 mm. Respiratory motion was >5 mm for all substructures (greatest for the LV/IVC), with the heart apex experiencing greater excursion than the base. Hysteresis-induced centroid/bounding box motion was <5 mm on average but exceeded 5 mm for 3 volunteers for the RCA, LADA/LCX, and LA/PVs/IVC, respectively. Cardiac motion was statistically significant ($p<0.05$) between all physiological substructure groupings (5/8-8/8 metrics), right/left heart (6/8 metrics), and coronary arteries/respective chambers (7/8-8/8 metrics). Statistically significant differences were also found for respiratory motion between the heart apex/base (6/8 metrics).

Conclusions: We have demonstrated that our 5D-MRI workflow successfully decouples cardiorespiratory motion with a single ~5-minute acquisition. Across volunteers, cardiac motion was >5 mm for the coronary arteries/chambers, while respiratory motion was >5 mm for all substructures. Future work includes extension to a thoracic cancer patient cohort and comprehensive margin analysis to facilitate highly effective cardiac sparing.

Distortion-Free Diffusion-Weighted Imaging of the Prostate Using TGSE-Based Golden-Angle PROPELLER Acquisition and Deep Learning Denoising

Jingjia Chen^{1,2}, Kun Zhou³, Mary Bruno^{1,2}, Hersh Chandarana^{1,2}, Daniel Sodickson^{1,2}, Qiuting Wen⁴, Li Feng^{1,2}

¹Bernard and Irene Schwartz Center for Biomedical Imaging, Department of Radiology, New York University Grossman School of Medicine, New York, USA. ²Center for Advanced Imaging Innovation and Research (CAI2R), Department of Radiology, New York University Grossman School of Medicine, New York, USA. ³Siemens Shenzhen Magnetic Resonance Ltd, Shenzhen, China.

⁴Department of Radiology and Imaging Sciences, Indiana University School of Medicine, Indianapolis, USA

Abstract

Purpose

Diffusion-weighted imaging (DWI) play an essential role in the detection, characterization, and staging of prostate cancer. While there has been longstanding interest in utilizing DWI to guide radiotherapy, its application has been largely limited by the widespread use of single-shot echo-planar imaging (SS-EPI) for DWI, which is highly susceptible to image distortion caused by susceptibility artifacts from rectal gas, the bladder, and surrounding structures. These distortions significantly affect the fidelity of DWI, thereby compromising the accuracy of treatment planning.

Non-EPI such as turbo spin echo (TSE) offers a promising alternative for DWI, effectively eliminating susceptibility-induced distortions. However, traditional diffusion-sensitized TSE imaging faces several major limitations. First, the long echo train in TSE can cause significant T2 blurring. Second, and more critically, the extended diffusion sensitization disrupts the Carr-Purcell-Meiboom-Gill (CPMG) condition. A straightforward approach to address this issue is to discard signals that do not meet the CPMG condition^{3,4}, which results in a substantial reduction in SNR.

This work proposes a novel Turbo Gradient Spin Echo (TGSE)-based DWI technique to overcome these limitations. Our technique incorporates a unique acquisition strategy using a multi-shot golden-angle PROPELLER sampling with complementary k-space coverage to combine different diffusion directions and shots while minimizing T2 blurring. It also employs a novel reconstruction approach to compensate for SNR loss through self-supervised image denoising. The performance of our technique, TGSE-PROPELLER-DWI, was demonstrated in prostate imaging, with comparisons against clinical SS-EPI-based DWI protocols (referred to as SS-EPI-DWI).

Methods

To achieve distortion-free, high-resolution prostate DWI within the same or shorter scan time as the clinical routine, we developed a novel golden-angle-rotated TGSE-PROPELLER-DWI acquisition scheme for prostate imaging. Detailed acquisition scheme can be found in the supporting document (Figure S1)

Ten subjects were recruited under IRB approval with written consent. MRI scans were conducted on a 3T scanner (Prisma, Siemens Healthineers). For each subject, prototype TGSE-PROPELLER-DWI was acquired at two resolutions ($1\times 1\times 3$ mm 3 and $1.54\times 1.54\times 3$ mm 3), using seven shots, three orthogonal diffusion directions, and two b-values (b50 and b1000). Clinical SS-EPI-DWI and T2-weighted images were also acquired for comparison and distortion assessment.

Results

In the supporting document, Figure S2 presents SS-EPI-DWI and TGSE-PROPELLER-DWI prostate images of three cases. Figure S2A compares high-resolution SS-EPI-DWI and TGSE-PROPELLER-DWI images in a healthy volunteer, highlighting distortion (red arrows) in the EPI-DWI images from large B0 variations near the anterior endo-rectal wall, absent in the TGSE-PROPELLER-DWI images. In Figure S2B, a suspected lesion (yellow arrows) is clearly delineated without distortion or signal loss in TGSE-PROPELLER-DWI, whereas SS-EPI-DWI shows visible signal dropouts at the edges and anterior portion of the prostate. Figure S2C shows a prostate cancer patient post-radiotherapy, currently under surveillance. Metal fiducial markers were placed inside the prostate for radiotherapy, which cause severe distortion (green arrows) in SS-EPI-DWI, while TGSE-PROPELLER-DWI remains unaffected.

Conclusion

This study proposes a novel MRI method for distortion-free prostate DWI with higher than clinical spatial resolution, offering a promising tool for guiding precise treatment planning.

Modality-AGnostic Image Cascade: Cross-Modality MAGIC for improved MR-Linac Cardiac Segmentation

Nicholas Summerfield^{1,2}, Qisheng He³, Joshua Pan¹, Chase Ruff^{1,2}, Ming Dong³, Carri Glide-Hurst^{1,2}

¹University of Wisconsin-Madison, Department of Human Oncology, Madison, USA. ²University of Wisconsin-Madison, Department of Medical Physics, Madison, USA. ³Wayne State University, Department of Computer Science, Detroit, USA

Abstract

Purpose- Cardiac substructure dose is more strongly associated with radiation-induced cardiac toxicities than the traditional whole heart metrics. MR-guided adaptive radiation therapy (MRgART) enables more enhanced daily cardiac sparing with improved visualization of substructure location. Building on our prior art, we present a state-of-the-art Modality AGnostic Image Cascade (MAGIC) pipeline for rapid cardiac substructure segmentation in MRgART, capable of conserving overlapping volumes for dosimetric evaluation and integrating complimentary high resolution multi-modality datasets to bolster segmentation performance in a single lightweight model.

Methods- Eighteen patients who underwent thoracic radiation therapy on a clinical 0.35 T MR-Linac were retrospectively evaluated, including both simulation and fractionated datasets (n=57) where MR-Linac fractionated images were used as training augmentation. Multi-modality datasets from two institutions including simulation CT (sim-CT, n=83) and diagnostic cardiac CT angiography (CCTA, n=52) images were also included to train (~70%), validate (~10%), and test (~20%) MAGIC. All images were labeled with 13 cardiac substructures and divided into three groups: Group 1, Whole Heart; Group 2, Chambers and Great Vessels including right/left atrium/ventricle, inferior/superior vena cava, pulmonary artery/vein, and ascending aorta; Group 3, Coronary Arteries including left anterior descending, left main, and right coronary arteries. For MAGIC, each group was targeted by separate segmentation deep learning layers in a cascaded structure, where predictions from prior, easier-to-segment groups are provided as input to later layers, facilitating informed multi-structure segmentation. Furthermore, modality-specific image encoders paired with single, shared decoders and prediction encoders were implemented to enable cross-modality learning, improving segmentation performance while remaining generalized to all included training modalities. For comparison, equivalent and separate MR-Linac only models (Unimodal) for each structure group were trained, resulting in 3 separate models. MAGIC was quantitatively benchmarked using the Dice Similarity Coefficient (DSC) and 95% Hausdorff distance (HD95) against reference contours, using paired t-tests to determine significance ($p<0.05$). Qualitative assessment was performed of the predictions against reference contours and underlying anatomy.

Results- MAGIC performed with an average \pm standard deviation DSC and HD95 of 0.68 ± 0.23 and $8.78\pm4.75\text{mm}$ respectively for MR-Linac, 0.71 ± 0.21 and $8.38\pm3.65\text{mm}$ respectively for sim-CT, and 0.87 ± 0.11 and $7.85\pm12.96\text{mm}$ respectively for CCTA images. Comparing MAGIC against Unimodal

methods for MR-Linac images, MAGIC significantly ($p<0.01$) improved both DSC and HD95 (DSC, 0.62 ± 0.31 ; HD95, 13.89 ± 13.90 mm). Notably, MAGIC had significant improvements for the great vessels and the coronary arteries where MAGIC predicted all coronary arteries, yet the Unimodal counterpart failed to predict 6/15 structures. MAGIC outperforms Unimodal for 11/13 structures for both DSC and HD95. Qualitative review demonstrated that MAGIC outperformed the equivalent MR-Linac models with fewer false predictions and more visual consistency with underlying anatomy.

Conclusion- Integrating multi-modality complimentary datasets enabled via a single lightweight model, MAGIC, improves cardiac substructure segmentation on low-field MR-Linac images, resulting in statistically significant improvements compared to unimodal, separate models, particularly for the coronary arteries. Furthermore, MAGIC remains generalized to enable concurrent segmentation on other imaging modalities included in training while handling organ overlap, offering potential for generalizability to other disease sites and applications.

Segmentation Regularized Registration Training Improves Multi-Domain Generalization of Deformable Image Registration for MR-Guided Prostate Radiotherapy

Sudharsan Madhavan¹, Lando Bosma², Josiah Simeth¹, Jue Jiang¹, Nicolas Côté¹, Nima Hassan Rezaeian¹, Chengcheng Gui¹, Daniel Gorovets¹, Sean McBride¹, Victoria Brennan¹, Michael Zelefsky³, Neelam Tyagi¹, Harini Veeraraghavan¹

¹Memorial Sloan Kettering Cancer Center, New York, USA. ²University Medical Center Utrecht, Utrecht, Netherlands. ³NYU Langone Health, New York, USA

Abstract

Purpose Deep learning models have reduced robustness when applied to datasets with different imaging characteristics than the training dataset. Hence, the goal of this work was to (a) improve the performance of a registration network by using a segmentation subnetwork to provide supervision for regularizing training, and (b) evaluate multi-domain generalization capability using datasets of prostate cancer patients acquired with two different MR platforms, namely, Unity hybrid 1.5T MR-Linac system and Philips 3T MR system.

Materials and Methods The study analyzed two types of MR images: 3T T2-weighted (T2WI) MR-simulation (MRSim) images (TR: 4740 ms, TE: 100 ms) from 34 patients, and 1.5T MR-Linac (MRL) images (TR: 1300 ms, TE: 87 ms) from 95 patients. All images were preprocessed using standardized preprocessing with intensity normalization and resampling to 192×192×128 dimensions. A previously published progressively refined joint registration segmentation (ProRSeg) method combining segmentation subnetwork to regularize registration network training was used to align T2WI MRI pairs. The network was trained using MRSim 3D images (training: 262, validation: 52), with weighted segmentation losses (bladder: 0.40, rectum: 0.30, prostate: 0.30), mean squared error for image similarity, and deformation smoothness penalty. We evaluated registration performance against the open-source SyN algorithm and Evolution methods, while also comparing ProRSeg results across two domains: same-domain (52 MRSim pairs) and different-domain (42 MRL pairs) testing. An MRL-MRL ProRSeg model (training: 288, validation: 72) provided benchmark performance. Registration accuracy used Dice similarity coefficient (DSC) and 95th percentile Hausdorff distance (HD95) for bladder, rectum, and prostate (CTV), with statistical significance evaluated using a two-sided, paired, Wilcoxon signed-rank test ($p < 0.005$).

Results ProRSeg produced high accuracy in same-domain registration, achieving mean DSC values of 0.88, 0.86, and 0.85 for bladder, rectum, and prostate respectively on MRSIM pairs. When evaluating

cross-domain performance, the MRSIM-trained model with segmentation supervision maintained statistically similar performance on MRL-to-MRL registration with DSC values of 0.87, 0.89, and 0.89. In contrast, without segmentation subnetwork supervision, the same MRSIM-trained model showed lower performance on cross-domain MRL-to-MRL pairs, with DSC values dropping to 0.70, 0.69, and 0.73 respectively, demonstrating the importance of segmentation supervision for cross-domain generalization. The MRL-MRL model, trained on MRL data, provided a benchmark for our method with DSC values of 0.91, 0.88, and 0.88, confirming the strong cross-domain performance of our MRSIM-trained model.

Conclusions This study demonstrates that deep learning-based deformable registration can achieve consistent performance across different MR platforms used in radiotherapy. While registration accuracy showed some expected degradation when applied across different scanner types, the network with segmentation supervision maintained HD95 under 3.5 mm. The inclusion of segmentation-based supervision during training significantly improved cross-domain generalization, particularly for the bladder where DSC improved from 0.70 to 0.87 in cross-scanner registration. These findings support the feasibility of using deep learning-based registration for organ tracking across different MRI platforms in radiotherapy.



THE 11TH ANNUAL SYMPOSIUM ON MAGNETIC RESONANCE IN RADIATION THERAPY

Proffered 1: Clinical Studies and Applications in MRgRT Part 1

Simulation and Pre-Planning Omitted Radiation Therapy (SPORT): Advancing MR-Guided Adaptive Radiotherapy for Prostate Cancer

Tsuicheng Chiu¹, Chris Kabat¹, Tingliang Zhuang¹, Justin Visak¹, Viktor Iakovenko¹, Sean Domal¹, Arnold Pompos¹, Roberto Pellegrini², David Sher¹, Shahed Badiyan¹, Raquibul Hannan¹, Mu-Han Lin¹

¹UT Southwestern Medical Center, Dallas, USA. ²Elekta, Milan, Italy

Abstract

Purpose: MR-guided adaptive radiotherapy (MRgART) has revolutionized treatment planning by enabling on-the-fly plan creation, paving the way to eliminate traditional simulation and pre-planning phases. This innovative approach leverages treatment-day imaging and advanced segmentation techniques to develop personalized treatment plans without the need for patient-specific simulations or pre-planning. In this study, we introduce Simulation and Pre-Planning Omitted Radiation Therapy (SPORT), a transformative workflow where curated preplans are directly adapted on-couch to match the patient's anatomy. This method streamlines the treatment process, delivering high-quality IMRT plans with significantly accelerated initiation while maintaining precise tumor coverage and optimal sparing of organs-at-risk (OARs).

Method: The SPORT procedure involves three key components: a generic plan library, automated segmentation, and robust planning strategies. First, the study developed three generic SBRT 5-fraction prostate plans corresponding to prescription schemes of 36.25 Gy, 40 Gy, and 45/40 Gy (simultaneous boost). One of these plans was selected as the preplan for treatment-day adaptation based on the medical directive. These generic plans were created without patient-specific imaging, incorporating only essential contours with predefined electron density (ED) and layering configurations. Second, treatment images were segmented automatically to minimize manual adjustments and streamline the workflow. Finally, planning objectives and optimization parameters were carefully designed to ensure robust adaptability and efficient optimization within a clinically practical timeframe. To validate the approach, each dose scheme was retrospectively tested on five randomly selected prostate cancer patients.

Results: After the prescription was entered into the record-and-verify (R&V) system, the corresponding generic plan was imported as a pre-plan into the treatment planning system (TPS) before the patient's treatment. IMRT quality assurance (QA) was performed on the selected generic plan. On the day of treatment, daily MR images were acquired and sent to an AI server for segmentation, with a processing time of approximately 30 seconds from image reception to readiness for use in the TPS. Optimization began with dose fluence followed by sequencing optimization, as patient anatomy often differed significantly from the generic plan. The initial dose fluence from the generic plan was typically suboptimal for the patient-specific geometry on the day of treatment. Optimization times for the different dose schemes averaged 321.41 seconds for the 45/40 Gy prescription, 107.96 seconds for the 40 Gy prescription, and 51.97 seconds for the 36.25 Gy prescription. The longer optimization time for the 45/40 Gy scheme was attributed to its emphasis on significant OAR sparing, which required a longer optimization process.

Conclusion: The feasibility study establishes a workflow designed to fully leverage adaptive radiotherapy capabilities, eliminating the need for traditional simulation and planning phases. By streamlining the treatment process, this approach not only simplifies the course of therapy by enabling a faster turnaround between the initial consultation and the start of treatment. This improved efficiency saves patients from additional visits for simulation and the typical one-week waiting period for planning. This allows for optimized resource utilization and ensures timely, precise, and effective treatment delivery.

A Super-Resolution model for auto-segmentation of low-resolution Prostate MR-Linac data

Funmilayo E.O. Olugbega^{1,2}, Marcel Breeuwer^{2,3}, Rob H.N. Tijssen^{1,2}

¹Dept. of Radiation Oncology, Catharina Hospital, Eindhoven, Netherlands. ²Dept. of Biomedical Engineering, Eindhoven University of Technology, Eindhoven, Netherlands. ³Dept. of Electrical Engineering, Eindhoven University of Technology, Eindhoven, Netherlands

Abstract

Purpose

Magnetic Resonance Imaging (MRI)-guided radiotherapy (MRgRT) for prostate cancer is effective, but challenged by long, resource-intensive, treatment workflows. Deep learning (DL)-based auto-segmentation can accelerate the contouring step [1]. However, existing methods have been developed using high-resolution (HR) MRI scans, which are optimized for manual contouring and typically require acquisition times on the order of minutes. With appropriate enhancement, low-resolution (LR) scans could potentially enable much shorter scan times. In this work, we investigate whether adding a super-resolution (SR) model can enable accurate auto-segmentation of LR MRI scans. A DL-based SR model was developed to improve the spatial resolution of LR scans, followed by the application of an auto-segmentation model.

Materials & Methods

The dataset included 250 prostate cancer patients who underwent MRgRT on a 0.35T ViewRay MRIdian. For each patient, high-resolution ($1.5 \times 1.5 \times 1.5 \text{ mm}^3$) simulation and first-fraction MRI scans with corresponding prostate contours were used, totaling 500 scans. A synthetic LR dataset was generated by reducing the extent of k-space by a factor of two, achieving the same voxel size as the LR survey scans (Figure 1).

The SR network employed a 2D U-Net architecture with residual learning and was trained on paired LR and HR scans. The model was optimized using a combination of mean absolute error loss and VGG-19 perceptual loss [2]. The image quality of the generated SR scans was assessed visually. For segmentation, a 3D U-Net model was independently trained on LR, SR, and HR MRI scans, each with corresponding prostate contours, resulting in three distinct models. The segmentation models were optimized using Dice Focal Loss [3]. Segmentation accuracy was evaluated using the Volume Dice Similarity Coefficient (VDSC), Surface Dice Similarity Coefficient (SDSC), 95% Hausdorff Distance (HD 95%), and Relative Volume Difference (RVD).

Results

The SR model successfully enhanced the spatial resolution of synthetic LR scans, as shown in Figure 1. Segmentation evaluation scores (Table 1) indicated minimal differences in performance between the three segmentation models trained on LR, SR, and HR scans. A statistically significant difference was observed only in the Relative Volume Difference (RVD) between the LR and HR segmentation models.

Conclusions

The proposed SR model effectively enhances the spatial resolution of synthetic LR MRI scans. Surprisingly, the auto-segmentation model performed similarly well on the synthetic LR data, suggesting that SR enhancement may not be necessary for our auto-segmentation network. In the near future, we plan to evaluate the model's performance on acquired LR survey scans. Furthermore, we will assess the feasibility of using LR or SR data for the visual assessment and adaptation of DL-generated contours in cases requiring manual adjustments.

[1] Comelli, Albert, et al. *Applied Sciences* 11.2 (2021): 782.

[2] Johnson, Justin, Alexandre Alahi, and Li Fei-Fei. *Computer Vision–ECCV 2016: Amsterdam, The Netherlands*

[3] Zhu, Wentao, et al. *Medical physics* 46.2 (2019): 576-589.

31

Liver Function Preservation after Feraheme-Enhanced MRI-Guided SBRT on 1.5T MR-Linac in Patients with HCC and Advanced Hepatic Cirrhosis.

Parisa Shamsesfandabadi¹, Vladmira Kirichenko², Danny Lee¹, Seungjong Oh¹, Allen Chen¹, Lorenzo Machado¹, Tadahiro Uemura¹, Alexander Kirichenko¹

¹Allegheny Health Network, Pittsburgh, USA. ²Thomas Jefferson University, Philadelphia, USA

Abstract

Purpose: Liver SBRT using MRI-guided radiotherapy for patients with hepatocellular carcinoma (HCC) and Child-Pugh B (CP-B) cirrhosis has shown promise. However, data on the safety and efficacy of using Ferumoxytol (Feraheme™), a superparamagnetic iron oxide nanoparticle (SPION) contrast agent, in conjunction with MRI-guided SBRT on a 1.5T MR-Linac remain sparse. This study evaluates the outcomes of ablative SBRT with SPION-enhanced MRI for localized HCC in patients with CP-B cirrhosis, focusing on liver function preservation and precision targeting.

Methods: This prospective study included 17 patients (21 lesions) with CP-B cirrhosis treated with ablative SBRT (median dose: 44 Gy in 3–5 fractions). SPION-MRI images enabled per-fraction adaptive treatment planning on the Unity MR-Linac (Elekta, Stockholm, Sweden). Functional liver volumes (FLV) derived from SPION-enhanced MRI were compared to anatomical liver volumes, and dosimetric parameters were adjusted to preserve residual FLV in cirrhotic liver. Follow-up evaluations included imaging, liver function assessments, and toxicity monitoring.

Results: With a median follow-up of 19 months (range: 4–26 months), 17 patients (21 lesions) with CP-B cirrhosis completed ablative SBRT to a median dose of 44 Gy (3–5 fractions). An automated contouring algorithm was applied to facilitate delineation of functional hepatic parenchyma and its guided avoidance using SPION-enhanced MRI. The prolonged retention of SPION contrast within hepatic parenchyma after single injection of Feraheme enabled per-fraction adaptive treatment planning throughout the treatment course, with a median duration of 15 days (range: 5–28 days).

Loss of functional hepatic parenchyma was observed in all patients with advanced cirrhosis when comparing predicted liver volumes to FLVs. Despite delivering ablative doses to tumors, the mean dose to residual FLV was consistently maintained below the liver's tolerance threshold in all cases. Four patients with intrahepatic progression underwent successful re-irradiation with SPION-MRI-guided liver SBRT during follow-up.

Seven patients successfully underwent liver transplantation at 3, 5, 6, and 7 months post-SBRT. A 100% in-field local control rate was achieved, with all transplant patients alive at the time of reporting. Treatment toxicity was limited to Grade ≤2 fatigue, and no cases of radiation-induced liver disease (RILD) or significant deterioration in MELD or ALBI liver function scores were observed beyond six months post-SBRT.

In one case, a patient who underwent orthotopic liver transplantation (OLT) three months after SBRT provided direct evidence of treatment effects. The explanted liver demonstrated classic morphological features of radiation-induced damage within the high-dose target volume (≥ 50 Gy) and complete regeneration of parenchyma outside the 25-Gy isodose region. This was confirmed by gross and histological examination, highlighting sharp demarcation between treated and unaffected regions. These findings align with our recent *in-vitro* studies showing that SPION agent Feraheme™, may confer radioprotective effects or enhance regeneration in liver parenchyma exposed to lower radiation doses.

Conclusions: SBRT with functional treatment planning allows identification and guided avoidance of residual functionally active hepatic parenchyma in patients with advanced cirrhosis. We report high local control and low toxicity leading to satisfactory pre- and post-liver transplant outcomes.

Study supported by the Elekta Research Grant: NCT04682847



THE 11TH ANNUAL SYMPOSIUM ON MAGNETIC RESONANCE IN RADIATION THERAPY

Proffered 2: MRI for Treatment Planning

Evaluating MR based ultra-hypofractionated focal boost to intraprostatic lesions for high-risk localized prostate cancer with histological reference

Erik Nilsson¹, Joakim Jonsson¹, Adalsteinn Gunnlaugsson², Lars Olsson², Karin Söderkvist¹, Tufve Nyholm¹

¹Umeå University, Umeå, Sweden. ²Lunds University, Lund, Sweden

Abstract

Purpose/Objective

Hypofractionated radiotherapy with focal boosts for prostate cancer (PCa) has been shown to increase five-year biochemical disease-free survival with acceptable toxicity levels¹. In the present study, we evaluated properties of optimized dose distributions by using whole-slide histopathology as reference standard.

Material/Methods

Fifteen high-risk (ISUP grade group (IGG) ≥ 4) radical prostatectomy patients with preoperative [⁶⁸Ga]PSMA-PET/mpMRI and [¹¹C]Acetate-PET/CT were included.

Prostate molds were 3D printed for each patient, based on the prostatic contour on T2-weighted (T2w) images. Ex-vivo T2w were obtained for resected prostates within the molds, followed by histopathological preparation and evaluation. Prostates were sectioned into 5 mm blocks, from which 5 μm thick microtome sections were taken such that sections coincided with ex-vivo T2w image slices. Microtome sections were digitized, and Gleason graded, resulting in detailed annotations of lesions with IGGs. The graded microtome sections were registered to ex-vivo images, which in turn were registered to the in-vivo T2w. The in-vivo T2w also served as a common frame of reference for co-registering PSMA-PET/mpMRI and CT.

Treatment planning was performed in Raystation (RaySearch Laboratories, Sweden) and image analysis in Hero (Hero Imaging AB, Sweden). We delineated organs at risk, seminal vesicles and lymph nodes. For each patient, four radiation oncologists independently contoured visible tumor on PSMA-PET/mpMRI as gross tumor volume (GTV). Ultra-hypofractionated treatment plans were generated to deliver 42.7 Gy to the prostate gland in 7 fractions, with a simultaneously integrated focal boost up to 49 Gy to the GTV, 29.4 Gy to lymph nodes and 31.2 Gy to seminal vesicles.

Results

The optimization resulted in 60 treatment plans, one for each patient and observer. The median fraction of histopathologically confirmed tumor also defined as GTV was estimated to be 0.61 (0.48–0.77)².

The average median dose to GTV was 48.8 (IQR: 48.5–48.8) Gy. Here, the median was taken across patients and the average over observers. The corresponding value for the highest-grade regions was 48.6 (IQR: 47.5–48.9) Gy, and for the lowest-grade regions, 43.0 (IQR: 42.8–43.5) Gy. Dose-volume histograms for GTV and all grades are shown in Figure 1.

No significant correlations were observed between mean dose to regions of varying IGG and Fleiss' kappa between observer delineations, see Fig. 2

Conclusion

Our results indicate that challenges in intra-prostatic tumor delineation led to underdosage of actual tumor, mainly in lower-grade regions. Observer agreement did not correlate with dose coverage, making it a poor quality-indicator.

References

1. Draulans C, et al. Stereotactic body radiotherapy with a focal boost to the intraprostatic tumor for intermediate and high risk prostate cancer: 5-year efficacy and toxicity in the hypo-FLAME trial. *Radiotherapy and Oncology* **201**, 110568 (2024).

2. Grefve J, et al. Histopathology-validated gross tumor volume delineations of intraprostatic lesions using PSMA-positron emission tomography/multiparametric magnetic resonance imaging. *Physics and Imaging in Radiation Oncology* **31**, 100633 (2024).

LONGITUDINAL PER FRACTION LESION SEGMENTATION AND TRACKING VIA FEW-SHOT DEEP LEARNING FOR MR-GUIDED RADIO THERAPY OF PROSTATE CANCER PATIENTS

Josiah Simeth, Sean McBride, Victoria Brennan, Harini Veeraraghavan, Neelam Tyagi

Memorial Sloan Kettering Cancer Center, New York, USA

Abstract

Purpose: MR images exhibit substantial variations due to different scanners and acquisition protocols. Hence, improving generalizability of automated segmentation models to such differences is essential for clinical and multi-institutional studies. We studied a deep learning model's robustness to imaging acquired on diagnostic, MR simulation, and MR Linac scanners. We also improved the capability of the method using few-shot learning for segmenting prostate cancers from pretreatment across 5 fractions of treatment (MR-Sim and MR-Linac).

Materials/Methods: The initial multi-resolution residually connected network (MRRN) model was created using a dataset of 151 patients with clinically significant lesions delineated on apparent diffusion coefficient (ADC) maps acquired on diagnostic MR (3.0T GE) with endorectal coil. the data was divided for 5-fold cross validation training with 26 patients withheld for final model selection.

Testing was conducted on a set of ten patients with 5 MR-Linac (1.5T Philips) scans corresponding to 5 fractions of treatment and one scan corresponding to pre-treatment MR-Sim (3T Philips) for a total of 59 images (1 instance missing). Each image included lesion designations

In order to enhance model performance in MR-Linac data after training on diagnostic scanners we utilized a few-shot fine tuning approach, wherein the MRRN model was fine-tuned on the MR-Linac data from two patients and then applied to the remaining 3 patients. Nested and stratified cross validation with early stopping was used to improve model generalizability to unseen data variations. Stratification was performed to ensure similar number of peripheral zone (PZ) and transition zone (TZ) as well as large and small lesions in the training and testing sets. Model finetuning was conducted by freezing all but the last layer of the MRRN for 10 epochs before unfreezing the final residual unit

Results: MRRN fine-tuned with few-shot training was more accurate than denovo MRRN model with a higher median lesion DSC (0.26 to 0.36, p=0.0001), higher lesion detection rate from 44 compared to 36 detected lesions out of 59 lesions total. Mean ADC values with segmented tumor gross tumor volume (GTV) by both models were moderately correlated with manually delineated GTVs ($R=0.53$ for MRRN and $R=0.51$ with fine-tuning). Median ADC extracted using AI methods were lower than median ADC extracted from manual delineations (Figure 1). Largest reduction in

estimated median ADC occurred with the fine-tuned model (173×10^{-6} manual to 152×10^{-6} mm²/s model). Figure 2 shows qualitative results of generating AI based segmentations using both models compared to the manual delineation.

Conclusions: Few-shot training with as few as 3 patients significantly improves model performance on treatment data. Median ADC from AI models show moderate correlation to the same values extracted from manual clinical segmentations. Study on larger and multi-institutional cohort is necessary to establish capability of such a training approach.

Identification of Radiotherapy Target Volumes in Glioblastoma using Advanced MRI and 18F-DOPA PET/CT

Eyesha Younus¹, Jing Qian¹, Derek Johnson¹, Deanna Pafundi², Shadi Chitsazzadeh³, Timothy Kaufmann¹, Daniel Trifiletti², Jennifer Peterson², Michelle Kim⁴, Sujay Vora³, Ugur Sener¹, Michael Ruff¹, Paul Brown¹, Jann Sarkaria¹, Anita Mahajan¹, Elizabeth Yan¹, Yue Cao⁴, Aiming Lu¹, Nadia Laack¹, Roman Kowalchuk¹, Debra Brinkmann¹, William Breen¹

¹Mayo Clinic, Rochester, MN, USA. ²Mayo Clinic, Jacksonville, FL, USA. ³Mayo Clinic, Phoenix, AZ, USA. ⁴University of Michigan, Ann Arbor, MI, USA

Abstract

Purpose: Standard of care gross tumor volume (GTV) definition for radiotherapy of glioblastoma includes gadolinium-enhancing tumor and resection cavity. However, it has been established that biologically relevant, non-enhancing tumor extends beyond this contrast-enhanced volume. Recent work at various institutions has shown that the non-enhancing tumor, outside and within the T2-FLAIR abnormality, can be identified using advanced imaging techniques of 18F-DOPA PET/CT and advanced MRI (aMRI); the latter utilizing dynamic contrast enhanced perfusion MRI and high b-value diffusion MRI. This work is the first to quantitatively compare the GTV volumes delineated using these advanced imaging modalities and to compare these with the GTV obtained using conventional MRI (GTV_convMRI) within the same patients. We hypothesized advanced imaging would identify non-enhancing tumor outside GTV_convMRI in the majority of patients and that the advanced imaging methods provide complimentary information.

Methods: Patients enrolled on a prospective study underwent 18F-DOPA PET/CT and aMRI along with standard MRI sequences. GTV was delineated using each of the advanced imaging modality, using methods established in prior work. GTV_PET was delineated using a predetermined threshold of > 2.0 based on the mean standard uptake value in normal contralateral brain, targeting the most aggressive regions of disease. GTV_Diffusion was delineated on high b-value images by thresholding the T2-FLAIR abnormality region with the mean signal intensity in the mirrored-up T2-FLAIR abnormality region. GTV_Perfusion was delineated, within the T2-FLAIR abnormality, on the cerebral blood volume (CBV) image obtained by fitting Tofts model to the perfusion data, using a CBV threshold from the frontal gray matter. A high dose GTV (HGTV) was then defined by adding GTV_PET, GTV_Diffusion, and GTV_Perfusion to GTV_convMRI. To compare the HGTV to the current glioblastoma radiotherapy volume delineation standards, isotropic 10-, and 20-mm expansions were applied to the GTV_convMRI and compared against HGTV and advanced imaging sub-volumes (GTV_PET, GTV_Diffusion, and GTV_Perfusion) to quantify the volume outside of these expansions. A threshold of 0.03cc was used to determine if a given GTV volume was outside another one.

Results: Of the 97 patients enrolled to-date, 4 had GTV_perfusion unavailable due to technical difficulties, 4 did not undergo aMRI due to MRI related contraindications, and 3 withdrew consent. In the 86 subjects included in the analysis, 7 patients had no abnormal uptake above the PET tumor-to-background ratio of 2.0 on 18F-DOPA image; the median (inter-quartile range) volume, in cm³, of

GTV_convMRI, GTV_PET, GTV_Diffusion, and GTV_Perfusion were 23 (11.6-34.6), 5.5 (0.84-16.0), 1.5 (0.7-3.4) and 9.4 (4.2-18.3), respectively. In this cohort, the HGTV was outside the GTV_convMRI+10mm in 45 (52%), and the GTV_convMRI+20mm in 18 (21%) patients. GTV_Diffusion and GTV_Perfusion were found to be outside of GTV_PET in 95% and 100% of patients, respectively, while GTV_PET was outside GTV_Diffusion and GTV_Perfusion in 88% and 87% patients, respectively.

Conclusion: 18F-DOPA PET and advanced MRI techniques identify tumor over one centimeter beyond contrast enhancement in over half of cases. These imaging modalities provide complementary information in the majority of patients. Follow-up data are needed to demonstrate how altering target volumes impacts patient outcomes.

A simplified online adaptive workflow for long-course MR-guided radiotherapy in esophageal cancer

Koen Kuijter, Roel Bouwmans, Lando Bosma, Gert Meijer, Stella Mook

University Medical Centre Utrecht, Utrecht, Netherlands

Abstract

Purpose

Online adaptive magnetic resonance-guided radiotherapy (MRgRT) offers the potential for high-precision radiotherapy for patients with esophageal cancer, aiming to reduce toxicity or enable dose escalation. However, the prolonged fraction durations currently limit the feasibility of daily online adaptive treatment for long-course treatment of esophageal cancer. In this study, we conducted an in-silico assessment of a simplified online adaptive MRgRT workflow, ATS-lite, in which deformable propagated contours are not modified, and assessed its feasibility.

Materials and Methods

This study included nine esophageal cancer patients previously treated with standard adapt-to-shape (ATS) workflow on a 1.5T MR-linac (Unity, Elekta AB, Sweden), where structures were manually corrected if needed. The CTV was expanded with a 6-mm isotropic margin, except for a 3 mm axial margin above the esophageal hiatus. A pre-treatment step-and-shoot IMRT plan prescribed a dose of 41.40 Gy in 23 fractions.

The ATS-lite workflow was simulated for each treatment fraction. All contours were deformably propagated onto the online MR-scan. A treatment plan was created using the unadjusted contours and the pre-treatment planning objectives and constraints. Intra- and interfraction dose accumulation were performed to evaluate target coverage per fraction and across the entire treatment. For individual fractions, coverage of the manually corrected CTV from the ATS workflow (clinical-ATS CTV) was considered adequate if $V95\% > 98\%$ and $V90\% > 99.5\%$. Additionally, heart and lung doses were compared between the delivered doses from ATS and ATS-lite, and a back-up CBCT plan with a 10-mm isotropic CTV-to-PTV margin.

Feasibility was assessed by recording treatment times in the initial patients treated with the ATS-lite workflow.

Results

The ATS-lite workflow achieved complete target coverage over the entire treatment for all patients, with sufficient coverage in 91% of the 177 fractions analyzed (Table 1). Except for patient 3, adequate coverage was achieved in at least 90% of the fractions for all other patients. Closer inspection revealed that inadequate target coverage in individual fractions was mainly due to substantial enlargement of the clinical-ATS CTV, which served as ground truth, rather than poor contour propagation in the ATS-lite workflow (Figure 1). For Patient 3, the clinical-ATS CTV length exceeded the reference CTV by over 6 mm in half of the fractions, with a maximum increase of 18 mm.

The ATS-lite workflow substantially reduced heart and lung doses compared to the CBCT plans, and was comparable to the standard ATS workflow (Figure 2). Specifically, a mean reduction of 79% in the heart V40 Gy (average from 6.6% to 1.4%) and 67% in the lungs V20 Gy (average from 7.4% to 2.6%) was observed.

In the first seven patients treated with the ATS-lite workflow, all 176 fractions were completed successfully on an MR-linac. Treatment times were recorded for 132 fractions, yielding a median treatment time of 23:00 minutes (interquartile range: 3:42 min).

Conclusions

The ATS-lite workflow provides adequate target coverage while substantially reducing heart and lung doses compared to conventional CBCT-guided plans. Additionally, this simplified workflow is feasible within 30-minute time slots, enabling online adaptive MRgRT for long-course treatments of esophageal cancer.

Investigating artefact-free online MR imaging during actively scanned proton therapy using a bi-directional whole-body in-beam MRI scanner

Emely Weichert^{1,2,3}, Franciska Lebbink^{3,4}, Sergej Schneider^{1,3}, Brad Oborn^{1,5,6}, Thomas Herrmannsdörfer², Aswin Hoffmann^{1,3,7}

¹Helmholtz-Zentrum Dresden-Rossendorf, Institute of Radiooncology-OncoRay, Dresden, Germany. ²Helmholtz-Zentrum Dresden-Rossendorf, High Magnetic Field Laboratory (HLD-EMFL), Dresden, Germany. ³OncoRay-National Center for Radiation Research in Oncology, Faculty of Medicine, and University Hospital Carl Gustav Carus, Technische Universität Dresden, Dresden, Germany. ⁴National Center for Tumor Diseases (NCT/UCC), Dresden, Germany; German Cancer Research Center (DKFZ), Heidelberg, Germany; Medizinische Fakultät and University, Hospital Carl Gustav Carus Technische Universität Dresden, Germany; Helmholtz-Zentrum Dresden-Rossendorf (HZDR), Dresden, Germany. ⁵Centre for Medical Radiation Physics, University of Wollongong, Wollongong, New South Wales, Australia. ⁶Illawarra Cancer Care Centre, Wollongong, New South Wales, Australia. ⁷Department of Radiotherapy and Radiation Oncology, Faculty of Medicine and University Hospital Carl Gustav Carus, Technische Universität Dresden, Dresden, Germany

Abstract

Purpose

A bidirectional open whole-body 0.5T MR scanner was recently combined with our horizontal proton pencil beam scanning (PBS) research beam line. This MR system allows for static and real-time imaging during simultaneous proton beam irradiation with the main MR magnetic field oriented either parallel or perpendicular to the proton beam central axis. The dynamic magnetic fringe fields produced by the nearby PBS scanning magnets in the nozzle could distort the MR magnetic fields, thus causing severe image artefacts [1]. The aim of this study was to assess whether artefact-free imaging is feasible during operation of the PBS scanning magnets.

Materials

A cylindrical homogeneous phantom was imaged once with the main magnetic field of the in-beam MR scanner oriented parallel to the proton beam, and once oriented perpendicular to the beam (Figure 1). To avoid activation of the MR magnet, proton beam irradiation over the maximum radiation field size of $40 \times 30 \text{ cm}^2$ was emulated by energizing the PBS scanning magnets without transporting the proton beam. The delivery of 9 dose spots was emulated either on the central horizontal (X), vertical (Y) or diagonal axis of the radiation field. The total irradiation time was adjusted to match the image

acquisition time. A fluxgate magnetometer was positioned close to the nozzle to monitor PBS scanning magnet operation.

Methods

Reference MR images were acquired prior to operating the scanning magnets. During PBS magnet operation, different clinically relevant MR sequences were acquired with different sets of repetition (TR) and echo times (TE) (Table 1). For dynamic imaging, a balanced steady state free precession (bSSFP) sequence was used to acquire single-slice images at 4 Hz. The MR images with and without PBS scanning magnet operation were compared by their central image intensity profiles and background noise levels. The percent signal ghosting ratio was evaluated according to the ACR accreditation protocol.

Results

For most of the sequences, there was no visible difference between the reference and the image acquired during PBS operation, and varying the TR and TE did not change this. For the bSSFP sequence with the main magnetic field oriented parallel, banding artefacts in the phantom were visible in the reference image (Figure 2). Only during PBS along the X-axis, the intensity level of these banding artefacts increased.

For real-time imaging, artefacts were visible in the reference image which are common for bSSFP sequences. The image quality did not deteriorate during PBS for both magnetic field orientations.

Conclusions

For the first time, artefact-free MR imaging using clinically relevant pulse sequences was performed during PBS for both parallel and perpendicular main magnetic field orientations. For all static MR images, image quality was maintained during PBS for both magnetic field orientations. Solely for the bSSFP sequence an enhancement of the observed image artefacts has been noted for the parallel magnetic field orientation during operation of the X-scanning magnets.

[1] Gantz et al. "Characterization of magnetic interference and image artefacts during simultaneous in-beam MR imaging and proton pencil beam scanning." Phys Med Biol. 2020;65(21):215014.

Initial clinical experience of stereotactic body radiotherapy (SBRT) for lung metastases with target intrafraction tracking and gating by means 1.5T MR-Linac

Michele Rigo, Chiara De-Colle, Andrea Gaetano Allegra, Luca Nicosia, Niccolò Giaj-Levra, Edoardo Pastorello, Francesco Ricchetti, Carolina Orsatti, Andrea Romei, Nicola Bianchi, Riccardo Filippo Borgese, Antonio De Simone, Davide Gurrera, Stefania Naccarato, Gianluisa Sicignano, Ruggero Ruggieri, Filippo Alongi

Advanced Radiation Oncology Department, Negrar di Valpolicella, Italy

Abstract

Purpose/Objective

The clinical introduction of Comprehensive Motion management (CMM) on 1.5T MR-Linac allows for target intrafraction tracking and gating, increasing the sparing of normal tissue without fiducials placement, ensuring the delivery of highly focused radiation to the tumor while further limiting the dose to adjacent OARs.

Clinical trials have shown lung SBRT is burdened by a not negligible risk of G \geq 3 toxicity. The continuous tracking allowed by CMM might reduce the volume of normal lung and chest wall irradiated, potentially decreasing toxicity without the need for oppressive immobilization. Moreover, it doesn't require additional radiation exposure compared to conventional Linacs. Lastly, the target gating eliminates the need to define an internal target volume (ITV) which could increase the volume of normal lung irradiated and only take into account a small part of tumor motion observed over tens of seconds in a 4D CT leading to potential under dosing in case of sudden large breathing motion, whereas MR-guided treatment with target intrafraction tracking and gating ensures greater precision.

Materials/Methods

In September 2023 CMM was installed at our Institution and used for all lung SBRT on the MR-linac. Patients included in this report had the following characteristics: 1) age > 18 years; 2) radiological diagnosis of lung metastases. Exclusion criteria were clinical contraindications to MRI.

Herein we report the treatments of the first five patients who met the inclusion criteria. The SBRT schedules ranges from 5 to 8 fractions with a total dose up to 60 Gy. The following variables were reported: patients and treatment characteristics, beam-on time, beam-hold (time of beam interruption due to gating) duty cycle (% of the total beam-on time of the entire delivery phase), positioning shifts.

Results

Between November 2023 and May 2024, 5 patients with lung metastases were treated with SBRT on 1.5T MR-linac using daily CMM.

ATS workflow was applied for 9 fractions and adapt-to-position ATP for the remaining 23 sessions.

All patients completed the planned treatment. The mean duty cycle for the 27 treatment fractions was 95.63% (95%CI 93.41-97.85). The mean beam-on time was 608.9 seconds (95%CI 552.4-665.4 seconds).

Globally, beam-hold occurred in all treatment fractions for a mean beam-hold count of 41.3 instances (95%CI 37.3-56.9). The mean beam-hold time of those treatment fractions was 201 seconds (95%CI 132-291). No baseline shift plan was performed due to persistent target drifts.

Acute treatment-related toxicity (acc. CTCAEv5.0) was very low: only 1 case (25%) of grade 1 cough. No G \geq 2 toxicity occurred.

Conclusion

This is our first experience on clinical application of CMM in a series of 5 consecutive patients with lung metastases treated with SBRT on 1.5T MR-linac. The implementation of CMM might lead to reduce PTV margins, decreasing the amount of lung healthy tissue within the high dose region without significant beam-on time increase. In conclusion, CMM was efficaciously implemented in our daily clinical routine also in lung SBRT. Treatment duration was minimally increased and the procedure was well tolerated by patients. Moreover, the acute toxicity rates reported by patients were very low.



THE 11TH ANNUAL SYMPOSIUM ON MAGNETIC RESONANCE IN RADIATION THERAPY

Proffered 3: MRI-Based Motion Management and Assessment

Optimizing Motion Management in Spine SBRT on the MR-Linac: Enhancing Delivery Efficiency with Real-Time Cine Imaging and Baseline Shift Corrections

Yao Ding¹, Travis Salzillo¹, Debra Yeboa¹, Martin Tom¹, Zhiheng Wang¹, Ergys Subashi¹, Jinzhong Yang¹, Fabienne Lathuilière², Sneha Cloake², Eun Young Han¹

¹MD Anderson Cancer Center, Houston, USA. ²Elekta AB, Stockholm, Sweden

Abstract

Purpose: This study aims to evaluate a comprehensive motion management system for spine stereotactic body radiation therapy (SBRT) on the MR-Linac (MRL). The research focuses on analyzing patient motion dynamics, establishing displacement thresholds, and assessing the effectiveness of baseline shift (BLS) simulations for correcting intrafraction motion, with the goal of enhancing delivery efficiency for spine SBRT.

Methods and Materials: Twelve patients underwent two MR imaging sessions on the MRL, each consisting of two 3D T2-weighted scans separated by 25 minutes of real-time 2D cine imaging. The optimal registration structure was determined, and intrafraction motion was quantified. Delivery efficiency was assessed based on a pre-defined displacement threshold. BLS simulations were performed to improve delivery efficiency in cases showing low performance. The dosimetric impact of BLS corrections was also analyzed.

Results: For optimal registration, motion tracking in the superior-inferior (SI) direction was most stable when using a structure that included the spinal canal and three adjacent vertebrae. Real-time cine imaging revealed average intrafraction motion (95%-5% range) of 0.8 ± 0.5 mm in the right-left (RL) direction, 0.9 ± 0.6 mm in the anterior-posterior (AP) direction, and 0.7 ± 0.5 mm in the SI direction. In comparison, 3D MRI analysis showed averages of 0.6 ± 0.4 mm (RL), 0.6 ± 0.7 mm (AP), and 0.6 ± 0.3 mm (SI). BLS simulations improved delivery efficiency to above 80 % in all but one case with a displacement threshold tolerance of ± 1 mm. While target coverage remained intact following BLS, cord dose (D0.01cc) increased by more than 14 Gy in three cases.

Conclusion: Optimizing registration structures and defining appropriate displacement thresholds are critical for improving the efficiency of spine SBRT workflows on the MR-Linac. Real-time cine imaging and BLS simulations are effective in reducing intrafraction motion and enhancing delivery efficiency. However, some patients may still experience challenges due to motion, highlighting the need for individualized BLS protocols to balance treatment efficiency with dosimetric safety.

Characterization of a Cartesian Self-Gated 4D-MR Imaging Sequence for SBRT

Stefan Dorsch^{1,2,3}, Cedric Beyer^{1,2}, Cornelius Eichner⁴, Alina Elter⁴, Sebastian Klüter^{1,2}

¹Department of Radiation Oncology, University Hospital Heidelberg, Heidelberg, Germany.

²National Center for Radiation Research in Oncology (NCRO), Heidelberg Institute for Radiation Oncology (HIRO), Heidelberg, Germany. ³German Cancer Research Center, Heidelberg, Germany.

⁴Cancer Therapy Imaging, Siemens Healthineers AG, Forchheim, Germany

Abstract

Purpose: Accurate motion management is critical for MRI in radiation therapy and diagnostic applications. Four-dimensional (4D) MRI captures volumetric motion data for example by reconstructing 3D images into multiple motion states (MS). Understanding and compensating for motion is especially important in Stereotactic Body Radiation Therapy (SBRT) due to the high radiation dose applied in a single treatment fraction. In this context, 4D MRI can be beneficial for accurately defining the internal target volume, which accounts for tumor motion throughout the respiratory cycle. Conventionally, 4D MRI acquisitions are achieved using radial acquisition schemes – due to their inherent motion sensitivity. However, such radial acquisitions suffer from image blurring and ill-circumscribed image artifacts. Further, radial sampling constitutes substantial oversampling of the k-space center, which limits the potential for acceleration. This study employs and evaluates a highly accelerated cartesian acquisition 4D-MRI sequence. Performance of both radial and Cartesian 4D sequences with self-gating was assessed using phantom and in-vivo measurements, with a focus on image quality and motion-state accuracy.

Methods: Measurements were performed on a 1.5 T MRI-scanner (MAGNETOM Sola, Siemens Healthineers, Forchheim, Germany) using a 4D motion phantom (Quasar MRI^{4D}, IBA Dosimetry, Schwarzenbruck, Germany) simulating a \cos^4 breathing pattern (amplitude: ± 15 mm, respiratory rate: 15 breaths/min). Two 4D sequences were investigated: (1) radial VIBE (8 MS) and (2) a prototype Cartesian VIBE (10 MS) with compressed sensing (CS) and Superior-Inferior projected navigation for motion capture. Phantom acquisitions were repeated five times with each sequence for statistical analysis. An automated MATLAB code evaluated the phantom position across MS. In-vivo measurements of healthy volunteers ($n=4$) used the same sequences and were performed within a diagnostic setup. A cine MR sequence (~ 1 min) was acquired before and after each 4D acquisition to estimate motion and validate the captured MS. For 4D sequences, liver motion was evaluated by delineating the organ in the first and last MS and calculating the center of mass displacement. For cine sequences, liver motion was assessed by tracking the liver cap at the diaphragm.

Results: Phantom measurements revealed good agreement between the sequences, with peak-to-peak distances of (1) (27.55 ± 1.2) mm and (2) (28.07 ± 0.7) mm (Figure1). In-vivo studies confirmed the finding that the Cartesian sequence is comparable to the radial acquisition (Table1), the alignment across motion states was less consistent for smaller breathing

amplitudes for both sequences. Further image quality assessments (Figure2) highlighted advantages of the Cartesian sequence: the radial VIBE images were affected by typical radial streaking artefacts and had lower SNR (radial: 14, Cartesian: 24), whereas the Cartesian VIBE achieved a better image quality.

Conclusion: Both sequences accurately captured phantom and respiratory motion, confirming their utility for 4D-MRI in motion management. The Cartesian sequence provided improved image quality compared to the radial VIBE. With compressed sensing, the Cartesian VIBE showed potential for $\sim 2x$ reduced scan time (down to 3:20 compared to 6:20 for the radial VIBE), making it a promising candidate for clinical 4D-MRI applications. The next step is to compare the 4D-MR sequences to the clinical gold standard 4D-CT.

Longitudinal Acceleration of Time-Resolved 4D MRI Exploiting Multi-Fraction Temporal Correlations

Jingjia Chen^{1,2}, Daniel Sodickson^{1,2}, Li Feng^{1,2}

¹Bernard and Irene Schwartz Center for Biomedical Imaging, Department of Radiology, New York University Grossman School of Medicine, New York, USA. ²Center for Advanced Imaging Innovation and Research (CAI2R), Department of Radiology, New York University Grossman School of Medicine, New York, USA

Abstract

Introduction

MRI-guided radiotherapy (MRgRT) typically involves multiple treatment fractions, during which precise patient alignment is performed, and the same MR images are repeatedly acquired across fractions. These longitudinal treatment fractions inherently provide extended temporal correlations over days or weeks, offering a valuable resource for accelerating MRI reconstruction as treatment progresses. However, current MRI reconstruction techniques rarely utilize this wealth of data information.

Dynamic MRI reconstruction has long been a vibrant research area within the MRI community. In a typical dynamic MRI reconstruction task, image correlations over seconds or minutes are commonly exploited by enforcing a temporal constraint. Building on this concept, we hypothesized that longitudinal MRI reconstruction can also be performed in a similar manner, considering an extended temporal scale spanning days or months rather than seconds or minutes. This new reconstruction strategy allow us to rethink accelerating MRI acquisition in longitudinal studies or treatment (e.g., MRgRT) by leveraging our decades of experience in standard rapid dynamic MRI.

To test this hypothesis, we developed an acquisition and reconstruction framework tailored for accelerated longitudinal dynamic MRI. The performance of this new framework has been demonstrated in the context of time-resolved 4D MRI of the liver within a longitudinal MRI setting.

Methods

Each subject underwent three successive free-breathing 4D MRI scans using navi-stack-of-star sampling on a 3T scanner. The longitudinal reconstruction (Figure S1) was performed by concatenating consecutive imaging spokes from three fractions. Rigid transformations were applied to the raw k-space data to correct for the misalignment between fractions. The structural similarity index measure (SSIM) and normalized root of mean squared error (NRMSE) were calculated for 4D volumes of each fraction against the references 4D volumes containing 600 spokes per fraction. Detailed imaging parameters and experiment setup are in the supporting document.

Results and Discussion

Figure S2 shows representative slices of dynamic liver images reconstructed from a subject with a liver lesion (red arrow). We demonstrated the concept of progressive acceleration by incorporating a long initial scan and two accelerated follow up scans. Multi-fraction reconstruction preserved high image quality even for later fractions with as few as 200 imaging spokes, while separate reconstruction showed blurring and under-sampling artifacts. The inclusion of two short scans improves the image quality of the first fraction as well. The liver lesion close to the diaphragm was delineated clearly even while moving substantially during breathing. SSIM and NRMSE confirm the improvement of the image quality using the multi-fraction reconstruction compared to the separately reconstructed images.

We have shown that the rich longitudinal correlations can be leveraged to improve image reconstruction and to push for progressive accelerations as longitudinal information accumulates. In MRgRT, 3D fast spin echo (FSE) is often used for obtaining accurate tumor positions due to its superior tissue contrast. However, FSE requires an order-of-magnitude increase in scan time compared to 3D GRE acquisition due to its longer TR. Though this work used gradient echo acquisition for purposes of demonstration, future work can adapt the longitudinal reconstruction framework to progressively accelerate 3D FSE acquisition in MRgRT.

Optimizing gated MR-linac treatments using 4D-MRI for motion-compensated daily imaging

Katrinus Keijnemans¹, Maarten Terpstra¹, Pim Borman¹, Bas Raaymakers¹, Eric Paulson², Martin Fast¹

¹University Medical Center Utrecht, Utrecht, Netherlands. ²Medical College of Wisconsin, Milwaukee, USA

Abstract

Purpose: Accurate radiotherapy requires that the 3D daily image used for plan adaptation captures the anatomy in a position representative of the treatment delivery. However, typical 3D-MRI acquisitions in free-breathing are susceptible to motion blurring. To overcome this problem, 3D-MRI on the MR-linac is typically acquired using respiratory-triggering on exhalation or with breath-holding, which may prolong scan times or result in non-representative anatomies for treatment delivery. This study investigates the feasibility of deriving high-definition daily 3D-MRIs from respiratory-correlated 4D-MRI acquired in free-breathing, offering a potential solution for motion-compensated imaging in gated MR-linac workflows.

Methods: A 3D fat-suppressed pseudo-golden angle balanced gradient echo radial stack-of-stars sequence (FOV = 420x420x208 mm³, FA = 50°, matrix size = 256x256x104, T_{acq} = 4:15 min:s) was acquired in three healthy volunteers on a 1.5 T Unity MR-linac (Elekta AB, Sweden). Two workflows were implemented to process the data into motion-compensated daily images that could be imported into the treatment planning system (TPS), which we here refer to as “4D-Baseline” and “4D-Accelerated”.

For the 4D-Baseline workflow, MIM Software 7.2.8 (MIM Software Inc., Cleveland, OH) was used to launch a MATLAB extension to sort k-space data and subsequently obtain a respiratory-correlated 4D-MRI using a conventional conjugate gradient SENSE reconstruction. The 4D-Accelerated workflow used a deep-learning model (MODEST) to accelerate the 4D-MRI data reconstruction. Next, deformable image registration (DIR) was performed using either MIM (multi-modality algorithm) or EVolution (an edge-based DIR algorithm) for the 4D-Baseline and 4D-Accelerated workflows, respectively. DIR-warped 4D phase images were combined to derive a high-definition daily 3D-MRI of the end-exhale, mid-position, or end-inhale anatomy. Gradient non-linearity corrections and DICOM header adjustments were performed to meet the TPS input requirements (Figure S1).

Analyses involved the time required for the two workflows to derive high-definition 3D-MRIs suitable for the TPS. Furthermore, the image quality was assessed using normalized cross-correlation (NCC) between images derived from both 4D reconstruction methods. A stack of 10 coronal slices through the liver was used for these pairwise comparison of 4D-MR images and high-definition 3D-MRIs derived from both methods. Lastly, the position of the liver-lung interface was determined in individual 4D-MRI phase images and high-definition 3D-MRIs and compared between workflows.

Results: The total processing times were 408 seconds and 213 seconds for the 4D-Baseline and 4D-Accelerated workflows, respectively, with the main difference being a 190-second faster 4D-MRI

reconstruction in the 4D-Accelerated workflow (Table S1). The median (min:max) NCC was 0.95 (0.93:0.97) between 4D-MRI phases and 0.98 (0.97:0.98) between high-definition 3D-MRIs. The liver-lung interface position in the deep-learning based reconstructions was more cranially positioned for some comparisons than the 4D-Baseline reconstructions. However, a maximum difference of only 2 mm (equaling one slice) was found.

Conclusions: This work showed the feasibility of acquiring 4D-MRIs and processing them into motion-compensated, high-definition daily 3D-MRIs suitable for gated treatments on the MR-linac. Including image acquisition, this workflow took either 8 minutes (4D-Accelerated) or 11 minutes (4D-Baseline). Further acceleration, either through shorter acquisitions with more undersampling, and/or fast reconstructions and processing are desirable.

Characterizing contractile motion along the stomach medial axis from dynamic MRI

Robert Jones^{1,2}, Daekeun You², Jeffrey Fessler¹, James Balter²

¹Department of Electrical and Computer Engineering, University of Michigan, Ann Arbor, USA.

²Department of Radiation Oncology, University of Michigan, Ann Arbor, USA

Abstract

Purpose

Characterizing the temporal and spatial sparsity of stomach contractile motions will support investigations of motion modeling and prediction. A study was performed to model antral contractions as traveling sinusoidal waves along the length of the stomach medial axis from dynamic MRI data.

Methods

A hierarchical motion model extracted from golden-angle radial dynamic abdominal MRI data of patients provided 21 canonical gastrointestinal (GI) motion states at phase angles of antral contraction which were deformably aligned to the first state, from which the outer stomach wall was delineated and the stomach medial axis was extracted. The registration transforms were applied to map the stomach to each phase angle image. The reference image and all subsequent contraction angle images were transformed to a medial axis coordinate space by sampling planes every 1mm along the centerline of the stomach, yielding 21 “centerline” GI phase angle images and corresponding stomach delineations.

To quantify stomach diameter as a function of position along the medial axis, the equivalent diameter (ED) of the outer stomach wall was computed in each slice of the centerline images as $ED = \sqrt{4S/\pi}$ where S is the area of the delineation in the given slice. The relative changes in outer-wall ED (ED_{rel}) were obtained by min-max normalizing the ED from all phase angles t at each spatial position x:

$$ED_{rel}(x,t) = (ED(x,t) - ED_{min}(x)) / (ED_{max}(x) - ED_{min}(x))$$

Outer stomach wall diameter change was then modeled as a function of spatial position, x, and phase angle, t, using a sinusoidal traveling wave:

$$ED_{rel}(x,t) = A \cdot \sin(kx + bt + \varphi) + c$$

where A, k, b and φ are, respectively, the wave amplitude, spatial frequency, temporal frequency and phase, and c is an additive constant. The spatiotemporal model was fitted to outer stomach-wall ED_{rel} values using an iterative nonlinear least-squares algorithm.

Results

The sinusoidal traveling wave model accurately fitted the outer stomach ED_{rel} and described the spatiotemporal trends of contractile motion observed in the canonical GI phase angle images. Model fitting yielded an RMSE of 0.155 and an r-squared of 0.81. The largest residual errors were observed between phase angles 8-11, where there was a jump/discontinuity in outer wall ED_{rel} data due to an artifact arising from the current phase angle reconstruction methodology. Overall, the fitted model resembled the observed dominant spatiotemporal trends in the outer wall ED_{rel} data.

Conclusions

A spatiotemporal sinusoidal traveling wave model was used to characterize contractile motion in terms of 5 parameters. This model accurately represented the contractile motion observed in canonical motion states. Future work will extend the model to analyze spoke-wise contractile motions, incorporate deformation vector fields to study contractile velocity and investigate spatiotemporal dynamics of the stomach inner wall and wall thickness. We plan to modify the current phase angle reconstruction to ameliorate the discontinuity artifacts present in the contractile motion data.

Combination of Pseudo-Golden-Angle Radial Acquisition and Deep Learning Reconstruction for Motion-Resolved 4D MRI on a 1.5T MR-Linac

Can Wu¹, Syed Siddiq¹, Sandeep Jogi¹, Victor Murray¹, Ricardo Otazo^{1,2}

¹Department of Medical Physics, Memorial Sloan Kettering Cancer Center, New York, USA.

²Department of Radiology, Memorial Sloan Kettering Cancer Center, New York, USA

Abstract

Purpose:

Online motion-resolved 4D MRI is crucial for adaptive radiotherapy of mobile tumors affected by respiratory motion, particularly on MR-Linac systems. While stack-of-stars acquisitions with golden-angle (GA) radial sampling provide high-quality 4D MRI, pseudo-golden-angle (PGA) sampling is commonly employed in clinical practice, making PGA-based 4D MRI the ideal candidate for clinical implementation. Fast 4D MRI reconstruction is also required, as compressed sensing methods like XD-GRASP take several minutes, whereas deep learning techniques like Movienet enable sub-second reconstruction. This study aimed to develop and validate an online 4D MRI workflow using a combination of PGA radial sampling and Movienet reconstruction for routine clinical use on a 1.5T MR-Linac.

Methods:

GA and PGA sampling: In GA sampling, the angle between consecutive spokes is 111.25° . In PGA sampling, the angle between adjacent spokes is fixed at $180^\circ/N$ (N : the total number of spokes). GA sampling provides relatively uniform k-space coverage when N is a Fibonacci number. For $N = 13$, GA sampling has the smallest and largest gaps of 10.03° and 16.23° , while PGA sampling maintains a constant gap of 13.85° .

Phantom scan: A Quasar MRI^{4D} phantom with a moving sphere was used to validate 4D MRI for motion measurements. Two sinusoidal waveforms with 4-second periods and amplitudes of 20/40 mm in the superior-inferior direction were tested. Stack-of-stars acquisitions using both GA and PGA radial sampling were performed for each waveform on a 1.5T MR-Linac (Elekta).

Volunteer scan: A healthy volunteer was scanned to compare 4D MRI image quality and abdominal motion using GA and PGA radial sampling. Fat suppression techniques, including spectral presaturation with inversion recovery (SPIR) and spectral attenuated inversion recovery (SPAIR), were utilized during approximately 5-minute scans.

4D MRI reconstruction: The k-space data were streamed in real-time via ReconSocket to a high-performance computer, where 4D MRI reconstruction was performed using Movienet with amplitude binning into 10 motion states.

Motion evaluation: 4D images were uploaded to MIM software for motion assessment. The maximum displacement (mm) of the moving sphere (phantom) and diaphragm (volunteer) along the superior-inferior direction was measured for each 4D MRI scan. Ground truth (GT) motion from the input waveform was used to calculate measurement errors in the phantom scans.

Results:

4D reconstruction time using Movienet was approximately 0.75 seconds. Image quality and motion differences between GA and PGA 4D MRI were minimal for both phantom and volunteer scans. Fat suppression was successful using SPIR and SPAIR in volunteer scans. Phantom scans showed accurate motion measurements, with errors of -2.0% and -3.8% for GA, and -5.5% and -2.3% for PGA at 20 mm and 40 mm. The measurement differences between PGA and GA were -3.6% (20 mm) and 1.6% (40 mm). In the volunteer scan, motion differences between GA and PGA were 5.7% (SPAIR) and 9.8% (SPIR).

Conclusions:

This work demonstrates that motion-resolved 4D MRI with PGA radial sampling performs similarly to GA sampling. The combination of PGA sampling and Movienet reconstruction could enable the integration of 4D MRI into the Elekta MR-Linac clinical workflow for adaptive radiotherapy.



THE 11TH ANNUAL SYMPOSIUM ON MAGNETIC RESONANCE IN RADIATION THERAPY

Proffered 4: Quantitative MRI Part 1

A multi-centre investigation of longitudinal changes in the apparent diffusion coefficient during short-course radiotherapy for patients with rectal cancer

Anne L. H. Bisgaard¹, Chavelli M. Kensen², Marielle E. P. Philippens³, Martijn P. W. Intven³, G. J. Meijer³, Corrie A. M. Marijnen², Uulke A. van der Heide², Erik van der Bijl⁴, Pètra Braam⁴, Petra J. van Houdt², Faisal Mahmood^{1,5}

¹Laboratory of Radiation Physics, Odense University Hospital, Odense, Denmark. ²Department of Radiation Oncology, The Netherlands Cancer Institute, Amsterdam, Netherlands. ³Department of Radiotherapy, University Medical Hospital Utrecht, Utrecht, Netherlands. ⁴Department of Radiation Oncology, Radboud University Medical Center, Nijmegen, Netherlands. ⁵Department of Clinical Research, University of Southern Denmark, Odense, Denmark

Abstract

Purpose

The apparent diffusion coefficient (ADC) derived from diffusion-weighted MRI (DWI) is a potential biomarker for predicting response to neoadjuvant radiotherapy in rectal cancer, enabling personalized treatment [1]. The introduction of the hybrid MRI linear accelerator (MRI-Linac) has made it feasible to acquire longitudinal DWI, and thus to obtain ADC measurements from each radiotherapy fraction. This study aims to determine whether longitudinal changes in the ADC can be detected during short-course radiotherapy in a multi-centre cohort of patients with rectal cancer treated on a 1.5T MRI-Linac.

Methods

This retrospective study included patients with rectal cancer across three centres who received radiotherapy on the MRI-Linac. All patients were enrolled in the ongoing MOMENTUM trial (clinicaltrials.gov, NCT04075305 [2]). In total, 200 patients were evaluated with respect to tumour characteristics and treatments. Patients with primary tumours who received short-course radiotherapy (5 fractions of 5Gy) with at least 2 fractions on the MRI-Linac, and no other treatment prior to this, were selected for further analysis (n=141).

GTVs were rigidly propagated from pre-treatment T2-weighted MRI to DWI for each treatment fraction. Within a 5 mm margin around the GTV, a region of interest (ROI) was defined on the high b-value DWI image using a threshold-based delineation tool [3]. ADC voxel-values were extracted within this ROI using b-values in the range [100, 800] s/mm². For each patient, median ADC values within the ROI were reported and the ADC time-trend across fractions was extracted using linear fitting. Acquisition-related ADC variation was addressed by grouping sequences according to scan parameters and applying median scaling of ADC histograms from all tumour voxel-values between the groups [4].

Results

Seven DWI sequences were identified across centres and grouped into 4 sequence groups (Figure 1). Important differences between the sequence groups were different echo times, repetition times and fat suppression techniques. Median ADC values were 1.13, 1.19, 1.07 and 1.16 mm²/s for sequence group 1, 2, 3 and 4, respectively. Relatively small scaling factors (range: 0.98-1.09) were needed to account for this variation. The median (range) ADC change during radiotherapy was 19.8% (-23.7%-102.7%) (Figure 2).

Conclusion

This multi-centre study examined ADC values derived from longitudinal DWI collected using a 1.5 T MRI-Linac. The ADC variation across DWI sequences was relatively small, demonstrating feasibility of multi-centre investigations of DWI acquired on the MRI-Linac. We observed ADC changes during treatment larger than repeatability coefficients of 10.0-17.9% reported in other studies on the 1.5T MRI-Linac [5], suggesting that longitudinal DWI can reflect radiotherapy-induced changes. These findings encourage future multi-centre studies linking ADC to clinical outcomes in rectal cancer.

References

1. Schurink NW et al. Br J Radiol. 2019;92(1096):20180655.
2. de Mol van Otterloo SR et al. Front Oncol. 2020;10.
3. Bisgaard ALH et al. Phys Imaging Radiat Oncol. 2022;21:146–52.
4. Fernandez Salamanca M et al. Front Oncol. 2024;14:1–7.
5. Fernando N et al. Phys Imaging Radiat Oncol. 2024;30:100570.

MR Multitasking-driven Abdominal Integrated Imaging (MT-AI²)

Junzhou Chen^{1,2}, Qingle Kong¹, Yang Chen¹, Diane Ling¹, Eric Chang¹, Anthony Christodoulou², Debiao Li³, Wensha Yang⁴, Zhaoyang Fan¹

¹University of Southern California, Los Angeles, USA. ²University of California, Los Angeles, Los Angeles, USA. ³Cedars-Sinai Medical Center, Los Angeles, USA. ⁴University of California, San Francisco, San Francisco, USA

Abstract

Purpose:

MR features superior soft tissue contrast through qualitative and quantitative images, providing versatile information on, anatomy, motion, and function. These capabilities are invaluable for abdominal applications such as radiation therapy planning (RTP), where complex anatomy and pathologies exist and are complicated by respiratory motion. To achieve these capabilities, however, abdominal MR protocols typically comprise a group of sequences often consisting of multiple breath holds. The resultant long protocol time and inter-scan inconsistency in spatial resolution, orientation, and respiratory motion compensation strategies may markedly compromise the efficiency and effectiveness of clinical workflows.

In an effort to address these challenges, we propose MR Multitasking-driven Abdominal Integrated Imaging (MT-AI²) as a framework to produce volumetric motion-resolved, multi-contrast qualitative images as well multi-parametric quantitative maps in single 9-minute scan. Such framework will not only benefit the workflow of RTP but can also be used for functional evaluation in the target organ and toxicity evaluation among organs at risk after receiving radiation therapy. This work adopts non-Cartesian (stack-of-stars) sampling for added motion-robustness. The authors have taken steps to greatly reduce reconstruction and map fitting time, enhancing its potential for practical clinical use with further refinement and validation.

Methods:

The MT-AI² sequence consisted of repetitive cycles of four-stage FLASH readouts intermittently modulated by inversion-recovery and T2 preparation pulses to generate both qualitative T1, T2, and proton density-weighted image and quantitative T1 and T2 map. A stack-of-stars k-space sampling trajectory was used for added motion robustness. An in-house developed liver dome tracking algorithm allows for bi-directional fine-grained (> 20 bins) motion binning in the presence of dynamic contrast evolution. Motion-resolved, multi-contrast images were first reconstructed using the MR Multitasking low-rank tensor reconstruction framework. Reconstruction was implemented using Toeplitz-based self-implemented GPU CUDA kernels in conjunction with cuFINUFFT. T1 and T2 maps were then generated via GPU-based inner product with Bloch-simulated signal dictionaries, similar to MR Fingerprinting.

Phantom experiments (ISMRM/NIST premiums system phantom), 7 healthy volunteer and 2 patient studies were performed at 3T to demonstrate the feasibility. MT-AI² images were acquired at transverse orientation with 1.6 x 1.6 x 4.0 mm³ resolution, 320 x 320 x 56 matrix size.

Results:

On human subjects, MT-AI² was able to produce motion-resolved, multi-contrast 3D images as well as multi-parametric quantitative maps for healthy volunteers and patients with excellent visual quality. On the phantom, a high correlation of T1 and T2 values can be observed between the reference method and the proposed MT-AI² protocol both visually and from correlation analysis.

Iterative reconstruction time was reduced from 20-30 hours using gpuNUFFT to 4 minutes following implementation of the self-implemented Toeplitz-based CUDA kernels. Combined fitting time for T1 and T2 was 4 seconds for the whole volume.

Conclusions:

MT-AI² efficiently provides multi-faceted information that may be highly useful for a range of abdominal applications such as functional-informed treatment planning and plan adaptation in abdominal RT. The drastic acceleration in reconstruction and maps fitting also make this framework ready for clinical workflows. Further technical refinement and performance validation are warranted and underway.

Evaluation of a Novel Quantitative Multiparametric MR Sequence for Radiation Therapy Treatment Response Assessment

Yuhao Yan^{1,2}, Adam Bayliss¹, Florian Wiesinger³, Jose de Arcos⁴, Adam Burr¹, Andrew Baschnagel¹, Brett Morris¹, Carri Glide-Hurst^{1,2}

¹Department of Human Oncology, University of Wisconsin-Madison, Madison, USA. ²Department of Medical Physics, University of Wisconsin-Madison, Madison, USA. ³GE HealthCare, Munich, Germany. ⁴GE HealthCare, Little Chalfont, United Kingdom

Abstract

Purpose: Multi-parametric MRI has shown great promise to rapidly derive multiple quantitative imaging biomarkers for treatment response assessment. A novel Deep Learning-enhanced Multi-PArametric MR sequence, DL-MUPA, was evaluated for treatment response assessment for two prospective clinical trials: brain metastases patients treated with stereotactic radiosurgery (SRS) and head-and-neck (HnN) cancer patients treated with conventional fractionation adaptive radiation therapy (ART).

Methods: DL-MUPA acquires 3D proton density (PD), T1 and T2 weighted images in a single 4-6-minute scan and derives quantitative T1 and T2 relaxation time maps using least-squares, orthogonal matching pursuit dictionary fitting relative to spoiled gradient-echo simulated signals. The segmented sequence starts with a steady-state PD image acquisition using low flip angle ($FA \sim 1^\circ$) Zero TE, followed by a transient-state T1 and T2 magnetization prepared segmented Zero TE acquisition ($FA = 3^\circ$). Images were reconstructed using a DL-based reconstruction pipeline to reduce noise, artifacts and improve sharpness. Phantom benchmarking was performed over 1 year in the NIST-ISMRM phantom. Longitudinal DL-MUPA data were acquired without contrast agent on a 1.5T MR-simulator. In brain, data were acquired pre-treatment (PreTx) and every ~3 months after SRS (PostTx). In HnN, DL-MUPA were acquired PreTx, 2-3 weeks after treatment start (MidTx) and 3 months after treatment end (PostTx). T1 and T2 histograms of gross tumor volumes (GTVs) and parotids (HnN) were evaluated for treatment response. Uninvolved normal tissue (normal appearing white matter in brain and spinal cord in HnN) were evaluated for within-subject repeatability. Delta analysis was performed calculating changes in mean T1 and T2 values.

Results: Phantom benchmarking revealed systematic bias but excellent repeatability (inter-session coefficient of variation <0.9% for T1, <6.6% for T2), suggesting reliability in longitudinal studies. Uninvolved normal tissue values were consistent across timepoints (absolute $\Delta T1_{mean} < 65\text{ms}/5\%$ and $\Delta T2_{mean} < 4\text{ms}/6\%$) demonstrating excellent within-subject repeatability. A resolved brain metastasis demonstrated considerable changes at 4-month PostTx ($\Delta T1_{mean}=155\text{ms}/14\%$ and $\Delta T2_{mean}=12\text{ms}/19\%$) while 2 of 3 necrotic brain metastases demonstrated significant enhancement ($\Delta T1_{mean}>214\text{ms}/18\%$ and $\Delta T2_{mean}>7\text{ms}/9\%$) between 3-month and 6-month PostTx scans. Notable changes were also observed for a resolved HnN tumor at PostTx ($\Delta T1_{mean}=-340\text{ms}/-26\%$ and $\Delta T2_{mean}=-11\text{ms}/-18\%$). Another HnN patient with the left parotid close to the GTV exhibited longitudinal enhancement on T1 maps at MidTx ($\Delta T1_{mean}=52\text{ms}/6\%$) and PostTx ($\Delta T1_{mean}=93\text{ms}/10\%$) which coincided with a patient's reported outcome of persistent severe dry mouth. In comparison, the right parotid remained stable ($\Delta T1_{mean}=-19\text{ms}/-2\%$ at MidTx and $-43\text{ms}/-5\%$ at PostTx), suggesting potential of implementing DL-MUPA for identifying endpoints for functional organ at risk sparing in HnN ART.

Conclusions: Preliminary results suggest promise of applying DL-MUPA in treatment response assessment for tumor and functional organs. With confirmation in a larger cohort and corresponding outcome information, future applications of T1 and T2 via DL-MUPA can be established to assess brain metastases treatment response and identify actionable endpoints for HnN functional treatment adaptation.

Longitudinal ADC changes in the prostate and dominant lesion during hypo-fractionated SBRT on a 1.5 T MR linac: correlation with PSA response.

Sarah Morris¹, Christoph Maier², Alex Dresner³, David Barbee¹, Hesheng Wang¹, Ting Chen¹, Riccardo Lattanzi², Tobias Block², David Byun¹, Michael Zelefsky¹

¹NYU Langone Health, New York, USA. ²NYU Grossman School of Medicine, New York, USA. ³Philips Healthcare MR Oncology, New York, USA

Abstract

Purpose

To explore changes in apparent diffusion coefficient (ADC) across the whole prostate and dominant intra-prostatic lesion (DIL) during and after hypo-fractionated SBRT and assess how these changes correlate with reductions in prostate specific antigen (PSA) over 6 months post-treatment.

Methods

Fifteen patients underwent MR simulation followed by manual contouring by the physician of the whole prostate clinical target volume (CTV), and DIL (if present) in MIM. They received 5-fraction SBRT (40 Gy) on a 1.5 T MR linac with daily imaging and adaptation (Philips Marlin 1.5 T). Only patients not receiving hormonal therapy were included. PSA levels were measured at 3 and 6 months, and follow-up MRI was obtained at 6 months (Philips Ingenia 1.5 T).

MRI:

- **T2-weighted:** scan length = 4 min 11 sec, TFE, TR/TE=5566/120ms, resolution=0.9x0.99x3mm, SENSE factor 2.5 (AP).
- **Diffusion-weighted:** scan length = 2 min 28 sec, SE EPI, TR/TE=4108/83.4ms, b=0, 200,100, resolution=2.86x2.98x4mm, SENSE factor 2.5 (AP), using gradient overplus to maximize gradient strength.

Contours were converted to nifti format using pydicom. Image processing was performed using mrtrix.¹ DWI maps were resliced to the matrix of the T2w image. DWI data was denoised using a random matrix theory method² and fit with a mono-exponential (Equation 1). The mean ADC was calculated for prostate CTV and DIL.

$$S=S_0e^{-b \text{ ADC}} \quad \text{Equation 1}$$

Results

ADC values and longitudinal dynamics: Average ADC during treatment was $1.39 \pm 0.25 \times 10^{-3}$ mm²/s in the prostate and $1.34 \pm 0.19 \times 10^{-3}$ mm²/s in the DIL, comparable to previously reported values.³ On average ADC increased 3% in the prostate and 12% in the DIL during treatment and a further 9% in the prostate (range 2-25%) and 8% in the DIL (range -6-25%) at 6 months.

Correlation with PSA decrease: There was a strong significant correlation between ADC increase in the DIL during treatment and PSA reduction from 3 to 6 months ($R^2=0.9$, $p=0.01$). This correlation was not seen in ADC change in the DIL at 6 months. These results suggest ADC decrease in the DIL during treatment reflects treatment response, while post-treatment ADC changes may be driven by other microstructural processes which do not correlate with PSA decrease. No significant correlation with PSA was seen in the whole prostate.

Conclusions

ADC increased during and up to six months post-SBRT delivered on a 1.5T MR-linac. ADC increase in the DIL during treatment was strongly correlated with PSA reduction, indicating that longitudinal measurements of ADC in the DIL during hypo-fractionated SBRT could serve as a prognostic biomarker for treatment efficacy.

References

1. Tournier, J.-D. et al. MRtrix3: A fast, flexible and open software framework for medical image processing and visualisation. *NeuroImage*, 2019, 202, 116137
2. Veraart, J.; Fieremans, E. & Novikov, D.S. Diffusion MRI noise mapping using random matrix theory. *Magnetic Resonance in Medicine* (2016) 76(5), 1582-1593
3. Zakian, K. et al. Changes in Multimodality MRI Characteristics Following SBRT in Prostate Cancer. *Int. Journal of Radiation Oncology, Biology, Physics* (2017) 99, E745–E746

Multi-Center Diffusion-Weighted MRI Validation for 0.35T MR-Linac

Siamak Nejad-Davarani¹, Natalia Lutsik¹, Kathryn Mittauer², Nema Bassiri-Gharb², Joseph Weygand³, Tess Armstrong⁴, Shyam Pokharel⁵, Suresh Rana⁵, Hui Wang⁶, Alonso Gutierrez², Michael Kasper⁵, Eric Mellon¹

¹University of Miami Miller School of Medicine, Miami, USA. ²Miami Cancer Institute, Miami, USA.

³Dartmouth College, Lebanon, USA. ⁴Moffitt Cancer Center, Tampa, USA. ⁵Lynn Cancer Institute, Boca Raton, USA. ⁶AstraZeneca, Gaithersburg, USA

Abstract

Purpose

Radiation treatments on the MR-linac (MRL) enable acquisition of daily anatomic and physiologic images to assist with adaptation of treatment plans. The apparent diffusion coefficient (ADC) derived from diffusion weighted images (DWI) is a quantitative imaging biomarker that correlates with tumor cellularity and response to treatment. Repeatability and reproducibility testing of ADC values across centers is necessary as a prelude for multi-center diffusion studies and clinical trials of physiologic adaptive radiotherapy on low-field MRLs.

Methods

Echo-planar Imaging (EPI) based DWI was acquired using a commercial diffusion phantom composed of vials with six concentrations of polyvinylpyrrolidone (PVP) ranging from 0% to 50%. Images were acquired along the three orthogonal directions with two sets of b-values: [0,30,60,90,120,150,180,200,500,1000] s/mm² and [0,500,1000] s/mm². For the reproducibility assessment, measurements of the same phantom were performed on four MRLs at different institutions with both head and torso MRI coils. To explore the influence of gantry angle position, measurements were also repeated with the gantry set to the gantry angle with the highest distortion. For the repeatability assessment, four measurements were acquired at a single institution. The ADC values for each measurement were corrected to account for temperature difference from 22°C and were reported as the value at this temperature. Coefficient of variation (COV) and normalized deviation from the reference ADC values for each vial were calculated.

Results

The COV of ADC values measured on a single MRL when DWI images with three b-values were used ranged from 0.28% to 1.44% and from 0.39% to 2.52% across all vials when head coil and torso coils were used, respectively. When ten b-values were used, the COV ranged from 0.20% to 2.39% and from 0.70% to 4.45% for these coils. For measurements acquired amongst MRLs, the COV of ADC values estimated with three b-values ranged from 0.29% to 1.76%, and 0.87% to 2.63% for both coil sets. When ADC values were estimated with DWI sets of ten b-values across different MRLs, the COV ranged from 0.37% to 1.52% with the head coil and from 0.64% to 3.68% with the torso coil. To estimate

the deviation of measured ADC values from reference values, the normalized root mean squared error (nRMSE) was calculated across all vials and ranged from 2.42% to 3.17% across the measurements acquired on a single MRL and 3.37% to 3.72% across ADC values measured amongst MRLs. The results above were obtained with the gantry angle set to zero. When DWI images were acquired with the gantry angle at maximum image distortion, all metrics above worsened, with the nRMSE increasing by 7.55% and 2.52% for the three and ten b-value measurements, respectively.

Conclusions

Our study showed excellent repeatability and reproducibility of ADC values measured on a phantom using an EPI based DWI sequence on the low-field MRL. These results were consistent when using different combinations of b-values and when acquired with either the head or torso coils. These results suggest high likelihood of reliability of ADC measurements on patients across treatment courses and at different centers.

Quantitative modelling of oxygen delivery in patients with head and neck cancer using oxygen-enhanced MRI

Michael J Dubec^{1,2}, James Price¹, Damien J McHugh^{1,2}, James P B O'Connor^{1,2,3}, David L Buckley^{1,4}

¹The Christie NHS Foundation Trust, Manchester, United Kingdom. ²The University of Manchester, Manchester, United Kingdom. ³Institute of Cancer Research, London, United Kingdom. ⁴University of Leeds, Leeds, United Kingdom

Abstract

Purpose

Hypoxia mediates treatment resistance in tumours. Oxygen-enhanced (OE)-MRI is a non-invasive method for quantifying tumour oxygenation (1). OE-MRI analysis in tumours typically measures hyperoxia-induced changes in longitudinal relaxation rate change (ΔR_1). However, with dynamic OE-MRI, there is the possibility to assess the delivery of oxygen to tumours using quantitative modelling similar to that used in lung parenchyma studies (2). Here we aimed to obtain information on oxygen delivery in tissues of patients with head and neck cancer using dynamic OE-MRI.

Methods

Patients who had a primary tumour (PT), a local metastatic lymph node (LN) and the nasal concha (NC) within the imaging field of view were selected from a previous study (3). The OE-MRI protocol, acquired at 1.5 T, consisted of a T_1 measurement sequence (inversion-recovery turbo field echo (IRTFE)), and a dynamic OE-MRI sequence (IRTFE, temporal resolution = 12 seconds (sequence parameters available in (3))). During the OE-MRI sequence, air (21% O_2) was breathed for 4 minutes, followed by 100% oxygen (9 minutes), followed by air breathing (4 minutes). T_1 measurement permitted conversion of OE-MRI signal intensity $S(t)$ to $\Delta R_1(t)$. A piecewise model (equation 1) of oxygen-delivery was fitted to the $\Delta R_1(t)$ data by non-linear least squares fitting. The wash-in (τ_{in}) and wash-out (τ_{out}) time constants and the ΔR_1 plateau were fitted as free parameters and extracted for the primary tumour, lymph node and nasal concha for each patient. Median ΔR_1 was measured from the final 10 measurements on oxygen breathing for comparison. Parameter differences per tissue region were identified using a paired t-test. Parameter differences between tissues was assessed using repeated measures ANOVA with pairwise comparisons.

Results

Eight patients were included. Figure 1 A-C shows representative model fits to $\Delta R_1(t)$ for the primary tumour, lymph node and nasal concha. Table 1 shows results of ΔR_1 , τ_{in} and τ_{out} for each tissue region. τ_{out} was significantly shorter than τ_{in} for lymph node ($p=0.003$) and nasal concha ($p=0.036$) but not for primary tumour ($p=0.070$). τ_{in} and τ_{out} in the primary tumour were similar to τ_{in} and τ_{out} in the lymph node, but they were longer in the nasal concha (Table 1). ΔR_1 plateau and median

estimates were similar for the primary tumour and lymph node, but ΔR_1 plateau was significantly larger than the ΔR_1 median for the nasal concha ($p=0.010$).

Conclusions

Dynamic OE-MRI can measure oxygen delivery to tumours. Differences in τ_{in} between tissues may relate to blood flow differences, with shorter τ_{in} being associated with increased blood flow. Differences between τ_{in} and τ_{out} in tissues may relate to differences in haemoglobin oxygen saturation levels prior to hyperoxia. Analysis of oxygen delivery provides information on underlying processes relating to tissue oxygen transport, which could be important in understanding mechanisms of tumour hypoxia, and its modification. Further work will explore the OE-MRI modelling in a larger patient cohort, as well as assess radiotherapy-induced changes in oxygen delivery.

References

1. Cancer Res. 2016;76(4):787-95.
2. Eur J Radiol. 2015;84(2):318-26.
3. Radiother Oncol. 2023;183:109592



THE 11TH ANNUAL SYMPOSIUM ON MAGNETIC RESONANCE IN RADIATION THERAPY

Proffered 5: Advanced and Specific Topics Part 1

C-SegDeform: a novel alternative to image registration in MR-guided adaptive radiotherapy of pancreatic cancer

Mehdi Shojaei¹, Björn Eiben¹, Jamie McClelland², Simeon Nill¹, Alex Dunlop¹, Arabella Hunt³, Brian Ng-Cheng-Hin³, Uwe Oelfke¹

¹Joint Department of Physics, The Institute of Cancer Research and The Royal Marsden NHS Foundation Trust, London, UK, London, United Kingdom. ²UCL Hawkes Institute and Department of Medical Physics and Biomedical Engineering, University College London, UK, London, United Kingdom. ³The Royal Marsden NHS Foundation Trust, London, UK, London, United Kingdom

Abstract

Purpose-Pancreatic cancer is challenging to treat with radiotherapy due to anatomical changes between fractions and its proximity to critical organs-at-risk (OARs). Adaptive treatments on MR-Linacs address these changes by acquiring daily images[1] and employing image registration to propagate reference contours (Prop-ROIs), with subsequent manual modifications confined to a two-centimeter margin around the planning target volume (PTV+2cm). However, image registration introduces significant errors, and severe anatomical changes can cause the adaptation process to exceed the timeframe of 20min, underscoring the need for more accurate and time-saving solutions. Conventional deep-learning models could streamline this process but require large, high-quality datasets, which are scarce for MR-Linac pancreatic cancer cases[2]. To address these challenges, we propose C-SegDeform, a conditional segmentation approach combined with a novel structure-guided deformation-based augmentation (sgDefAug) pipeline to simulate potential daily anatomical variations. This approach is an alternative to registration-based contour propagation to improve accuracy and streamline treatment adaptation even when using small datasets.

Methods-Five patients were acquired, each with 5 session b3DVane images. OARs including small bowel, duodenum, kidneys, large bowel, liver, spinal canal, spleen, and stomach, were manually contoured and verified by two experienced clinical oncology consultants. After preprocessing, the sgDefAug approach was employed for data augmentation by applying anatomically plausible deformations through OAR scaling and displacement, generating 2 variants per image. Then, nnU-Net was trained on three patients with a conditional approach[3]. Each input-output comprised $(I_n, L_n, I_m) \rightarrow L_m$ where I_n and L_n are the image and label for session n , and I_m is the image for session m . The model's output L_m , is the predicted label for session m . The evaluation was conducted on two patients (each with 4 session images) comparing C-SegDeform with Prop-ROIs and included geometric accuracy (Dice score, average surface distance (ASD)) and dosimetric analysis using a clinically-delivered plan's dose

distribution, measuring $D_{2\%}$ difference to identify potential hotspots. Likert scaling was conducted to rank the usability of auto-contours[4].

Results-Training required 3 days, with results generated in approximately 30s. C-SegDeform improved Dice score from 0.74 ± 0.05 to 0.93 ± 0.01 and ASD from 7.93 ± 2.99 mm to 1.42 ± 0.47 mm compared to Prop-ROIs. Dosimetric analysis of $D_{2\%}$ revealed that C-SegDeform contours deviated by $0.40 \pm 0.42\%$ from the ground-truth, while Prop-ROIs showed a larger deviation of $4.32 \pm 2.27\%$, when normalized to prescribed dose (40Gy). These indicate that C-SegDeform requires fewer modifications, providing clinicians with more time to focus on accurately reviewing OARs within the PTV+2cm margin. To assess editing effort for pancreatic cancer stereotactic ablative body radiotherapy OAR contouring, Likert scale was used (R1:*No changes*-R5:*Unusable*). C-SegDeform contours required *no or minor edits* in 97.2% of cases (R1,R2) compared to 68% for Prop-ROIs. Only 2.8% needed *minor edits better than starting from scratch* (R3), with none requiring *major edits* or being *unusable* (R4,R5), unlike 20% for Prop-ROIs.

Conclusions-The proposed C-SegDeform is simple, computationally efficient, clinically practical, and fast enough for integration into an MR-Linac online adaptive workflow. By replacing registration-based contour propagation, it reduces contour modifications and clinician workload, provides reliable results, ultimately improving patient outcomes.

Need for Speed: Timegain of AI-based delineations for MR-guided online adaptive radiotherapy of prostate cancer

Maximilian Konrad^{1,2}, Carsten Brink^{1,2}, Anders Bertelsen¹, Ebbe Lorenzen^{1,2}, Christina Nyborg³, Lars Dysager³, Tine Schytte^{3,2}, Uffe Bernchou^{1,2}

¹Laboratory of Radiation Physics, Odense University Hospital, Odense, Denmark. ²Department of Clinical Research, University of Southern Denmark, Odense, Denmark. ³Department of Oncology, Odense University Hospital, Odense, Denmark

Abstract

Purpose

Daily magnetic resonance imaging (MRI)-guided radiotherapy plan adaptation relies on time-intensive manual delineation adjustments for targets and organs at risk (OAR) prior to every delivered treatment fraction, posing a significant challenge to workflow efficiency. Advances in auto-segmentation have demonstrated the capability to generate accurate delineations rapidly but the in-clinic time benefit remains unexplored. This study aims to assess the feasibility and potential time benefit of integrating online artificial intelligence (AI)-based delineations for prostate cancer treatment on a 1.5T MRI-Linac.

Methods

This prospective study included 15 consecutive prostate cancer patients treated with 60 Gy in 20 fractions on a 1.5T MRI-Linac. The first five patients (Group 1) underwent treatment using the standard workflow for all fractions. The remaining ten patients (Group 2) followed the standard workflow for 1 up to 3 fractions (Group 2 – Standard) and an AI-based workflow for the subsequent fractions (Group 2 – AI). AI-generated delineations were provided through an in-house AI inference service, which received delineations from an in-house developed nnU-Net model. Figure 1 illustrates the standard and AI-based workflow per delivered fraction. In the standard workflow, target and OAR delineations were propagated from reference scans to the daily scan using deformable image registration and then manually corrected if clinically relevant. In contrast, the AI-based workflow involved importing AI-generated delineations, merging them with bone, external and couch structures from the reference scans and correcting the delineations where needed. Differences in delineation time and total treatment time per fraction were analyzed for statistical significance using linear mixed models.

Results

The AI-based workflow significantly reduced the median delineation time by 46 % (see Figure 2a) from 9.8 minutes to 5.3 minutes (p -value < 0.001). Similarly, the overall treatment time was reduced by 8 % from 27.3 minutes to 25.0 minutes (p -value < 0.02). Delineation time variability increased throughout the treatment course for patients in Group 1 but remained stable in Group 2, highlighting the consistency of the AI-based delineation workflows over the entire treatment (see Figure 2b). For one patient, the nnU-Net model delivered suboptimal results and led to increased delineation time. Due to

the modular implementation of the AI inference service, a patient-specific model could be trained and deployed for this patient for the remaining fractions, reducing the delineation time also for this patient.

Conclusion

Integrating AI-based delineation at the MRI-Linac is feasible and effectively reduces delineation time. The reduced variability in delineation duration enhances the predictability of daily treatment scheduling. Additionally, in-house developed AI algorithms enable training patient-specific models and deploying them quickly, ensuring more accurate and consistent delineation within the online workflow for non-standard anatomies. The AI workflow is now part of our clinical standard treatment for all patients with pelvic cancer.

Accelerate Diffusion-Weighted MRI with Extended b-values via Implicit Neural Representation Learning

Yurok Song¹, Adam Johansson², Lianli Liu³

¹Emory University, Atlanta, USA. ²Uppsala University, Uppsala, Sweden. ³Stanford University, Palo Alto, USA

Abstract

INTRODUCTION: Diffusion-weighted MRI (DWI) is conventionally acquired with 2-3 b-values. Acquiring DWI with extended b-values (more than 3 b-values with the highest b-value greater than 1000 s/mm²) has the potential of supporting higher-order diffusion analysis for more accurate characterization of tissue environment. The dense sampling of b-values, however, prolongs the image acquisition time and limits the clinical utility. Aimed at accelerating DWI acquisition with extended b-values, this study investigates integrating self-supervised implicit neural representation learning with an explicitly defined low-rank model to reconstruct high quality DWI images from 10-fold under-sampled k-space data.

METHOD: For a DWI dataset acquired with B different b-values at N different spatial locations I , we first decompose the dataset into a spatial subspace \mathbf{U} and a signal attenuation subspace \mathbf{V} such that $\mathbf{I} = \mathbf{UV}$. As signal attenuations with increasing b-values are correlated across different spatial locations, the DWI dataset is low-rank. Given the limited number of tissue types presented in the DWI dataset, the signal attenuation subspace \mathbf{V} can be further estimated from low-resolution DWI images reconstructed using the center of the k-space only. To recover high-resolution spatial subspace \mathbf{U} from sparse k-space samples, a multi-layer perceptron network was optimized to learn the implicit neural representation of \mathbf{U} . Specifically, a continuous mapping function from matrix indices of \mathbf{U} to values of \mathbf{U} was defined. The network takes function coordinates as inputs and outputting the corresponding function values to estimate \mathbf{U}' . The network was optimized by minimizing the L2 loss between the reconstructed image $\mathbf{U}'\mathbf{V}$ and k-space samples at sparsely acquired positions.

RESULTS: The proposed method was evaluated using a DWI brain dataset that consists of DWI images acquired from 10 subjects with 9 b-values ranging between 0 s/mm² to 2400 s/mm². We retrospectively subsampled the 8-coil k-space data, by fully sampling the central 16 phase encoding lines and sparsely sampling the periphery phase encoding lines with an acceleration

factor (AF) of 10. Compared to a parallel imaging-based method (GRAPPA) with an acceleration factor of 4 and 16 calibration lines, the proposed method achieves higher peak signal-to-noise ratio (44.48 ± 2.88 dB versus 43.29 ± 1.47 dB) between sparse reconstruction and fully sampled ground truth. Fitting a mono-exponential model and a higher-order diffusion kurtosis model to sparsely reconstructed and ground truth DWI dataset demonstrates good consistency in apparent diffusion coefficient (ADC) and diffusion kurtosis quantification. The mean absolute error across the 10 subjects was $(5.08 \pm 1.88) \times 10^{-5}$ mm²/s, $(1.05 \pm 0.46) \times 10^{-4}$ mm²/s and 0.16 ± 0.04 for ADC, kurtosis-corrected diffusion coefficient and diffusion kurtosis calculation. Paired t-test suggests no significant difference ($p > 0.01$) between diffusion quantification results when using sparsely reconstructed versus ground truth DWI dataset.

CONCLUSION: Integrating implicit neural representation learning with an explicitly defined low-rank model provides effective regularization for the ill-posed problem of DWI reconstruction from sparsely sampled k-space. The proposed method achieves higher acceleration factor and improved image reconstruction quality, as compared to clinically used parallel imaging-based methods. Quantitative diffusion parameter mapping suggested the reconstructed images may be used to support higher-order diffusion analysis for more accurate characterization of diffusion properties.

A software framework for automated commissioning of AI Segmentation models for radiation therapy workflows

Nicolas Côté^{1,2}, Jue Jiang¹, Ifeanyirochukwu Onochie¹, Harini Veeraraghavan¹, Neelam Tyagi¹, Arthur Lalonde², Sharif Elguindi¹

¹Memorial Sloan Kettering Cancer Center, New York, USA. ²Université de Montréal, Montréal, Canada

Abstract

Introduction

The integration of artificial intelligence (AI) segmentation models into radiation therapy clinical practice necessitates an efficient and streamlined processes. We introduce “Validator,” a generalized software application designed to automate the labor-intensive commissioning of AI models for clinical use. The platform features a web-based graphical user interface (GUI) that enables users to collect and tag benchmark DICOM data, execute unapproved AI models, and generate standardized commissioning reports for review with just a few clicks. The report includes quantitative metrics such as the 95th percentile Hausdorff Distance (HD95), as well as 3D and surface Dice similarity coefficients (DSC, SDSC). Visual previews of the best and worst performing anatomical regions on the test set are provided, alongside blended 3D meshes of AI-generated structures with ground truth segmentations to facilitate rapid qualitative evaluation. The system also supports benchmarking initial test set performance against future model iterations.

Methods

To evaluate the software’s capabilities, we trained a previously published transformer architecture to segment upper gastrointestinal (GI) organs from MRI scans. A training dataset comprising 30 patients with locally advanced pancreatic cancer, treated with hypofractionation using the MR-Linac Unity system and contoured over five fractions, was established. An independent test set of 10 patients, fully contoured by a trained anatomist, was specified in an Excel table, and submitted to Validator via file upload. Metrics computed included surface Dice similarity coefficients at 1 mm, 2 mm, and 3 mm thresholds, 3D DSC, and HD95. These metrics were compiled into a general summary table and detailed per individual case within the report. Additionally, 2D slice previews and 3D mesh visualizations were generated to compare AI model contours with ground truth segmentations.

Results

The average metrics for HD95, volumetric Dice similarity coefficient (VDSC), and surface Dice similarity coefficient (SDSC) across all 10 test cases are summarized in Table 1. Within the current framework, the total time to generate the report is approximately 25 minutes, encompassing data retrieval from the clinical PACS and model inference execution. The report is accessible via an internal webpage and can be

readily downloaded for local analysis. Figure 1 shows a sample of the file upload and data processing as well as the generated report.

Conclusion

The Validator framework effectively generates comprehensive reports for newly trained or retrained AI models, providing detailed, objective evaluations of performance relative to previous iterations, supplemented by visual assessments of key areas. Initial testing indicates that segmentation of the small bowel underperforms compared to other structures, highlighting the need for additional curated data to improve model accuracy. This evaluative process assists users in identifying areas for improvement, potential issues, and critically, determining the model's readiness for rapid integration into clinical practice.

The impact of deep learning organ delineation uncertainty for prostate cancer radiotherapy

Viktor Rogowski^{1,2}, Angelica Svalkvist^{3,4}, Matteo Maspero^{5,6}, Tomas Janssen⁷, Federica Carmen Maruccio⁷, Jenny Gorgisyan^{8,9}, Jonas Scherman⁸, Ida Häggström^{10,11}, Victor Wåhlstrand Skärström¹⁰, Adalsteinn Gunnlaugsson¹², Martin Nilsson¹², Mathieu Moreau¹², Nándor Vass¹², Niclas Pettersson^{3,4}, Christian Jamtheim Gustafsson^{8,13}

¹Radiation Physics, Department of Hematology, Oncology and Radiation Physics, Skåne University Hospital, Lund, Sweden. ²Department of Medical Radiation Physics, Clinical Sciences, Lund University, Lund, Sweden. ³Department of Medical Radiation Sciences, Institute of Clinical Sciences, Sahlgrenska Academy, University of Gothenburg, Gothenburg, Sweden. ⁴Region Västra Götaland, Sahlgrenska University Hospital, Department of Medical Physics and Biomedical Engineering, Gothenburg, Sweden. ⁵Department of Radiation Oncology, Imaging and Cancer Division, University Medical Center Utrecht, Utrecht, Netherlands. ⁶Computational Imaging Group for MR Diagnostics & Therapy, Center for Image Sciences, University Medical Center Utrecht, Utrecht, Netherlands. ⁷Department of Radiation Oncology, The Netherlands Cancer Institute, Amsterdam, Netherlands. ⁸Radiation Physics, Department of Hematology, Oncology, and Radiation Physics, Skåne University Hospital, Lund, Sweden. ⁹Medical Radiation Physics, Department of Clinical Sciences Lund, Lund University, Lund, Sweden. ¹⁰Department of Electrical Engineering, Chalmers University of Technology, Gothenburg, Sweden. ¹¹Department of Medical Radiation Sciences, Gothenburg University, Gothenburg, Sweden. ¹²Department of Hematology, Oncology, and Radiation Physics, Skåne University Hospital, Lund, Sweden. ¹³Department of Translational Medicine, Medical Radiation Physics, Lund University, Malmö, Sweden

Abstract

Purpose

Deep learning (DL)-based delineation of organs-at-risk for radiotherapy is becoming increasingly common. While DL models can calculate voxel-wise uncertainty maps of their segmentations, this map is rarely presented to clinicians. Our aim was to assess the impact and value of DL-generated uncertainty maps presented to radiation oncologists during the delineation of pelvis structures for prostate radiotherapy.

Methods

Two nnUNet DL models were trained with 10-fold cross-validation on a dataset of 434 patients undergoing ultra-hypofractionated MRI-only radiotherapy for prostate cancer. The models performed clinical target volume (CTV) and rectum segmentation. Each cross-validation model was evaluated on an

independent test set of 35 patients. Segmentation uncertainty was calculated voxel-wise as the SoftMax standard deviation (0-0.5, n=10) and visualized as a fixed scale color-coded map.

Four oncologists were asked to:

1. Step1: Rate the quality and confidence of the DL segmentations using a four and five point Likert scale respectively and correct the delineations without access to any uncertainty map.
2. Step2: Repeat step1 after at least four weeks with the color-coded uncertainty map available. Oncologists were asked to blend the uncertainty map with the DL segmentation and MRI volume (Figure 1).

Delineation time was recorded for both steps. In *step2*, oncologists also provided free-text feedback on the benefits and drawbacks of using the uncertainty map during delineation. A histogram analysis was performed to compare the number of voxels changes between *step1* and *step2* for different uncertainty levels (bins with 0.1 interval).

Results

The DL models achieved high-quality segmentations with a mean Dice coefficient per oncologist of 0.97-0.99, calculated between edited and unedited structures in *step1* for the prostate and rectum.

While the overall quality rating decreased slightly for rectum segmentations on a group level in *step2* (statistically significant), individual responses varied. Some oncologists rated the quality higher for prostate with the uncertainty map, while others rated it lower. Similarly, confidence ratings varied across oncologists and organs (Table 1).

Decreased delineation time was recorded for three oncologists using uncertainty maps, saving 1-2 minutes per patient. The majority of oncologists found the uncertainty maps helpful, and one reported benefit was the ability to quickly see where to focus more thoroughly.

The histogram analysis indicated fewer voxel edits in regions of low uncertainty in *step2* compared to *step1*. Specifically, 50% less voxel edits were recorded for the uncertainty region 0.0-0.1, suggesting increased trust in the DL model's prediction in these areas (Figure 2).

Conclusions

Presenting DL uncertainty information to radiation oncologists can influence their decision-making, perception, and trust in the DL segmentations. Regions with low uncertainty were less likely to be edited, indicating increased reliance on the model's predictions. Additionally, uncertainty maps can improve efficiency by reducing delineation time. Our study suggests that DL-based segmentation uncertainty can be a valuable tool in clinical practice, enhancing the accuracy and efficiency of radiation therapy planning.

Radiomics Approaches for Survival Prediction and Risk Stratification in Glioma Using MRI

Walid Dandachly¹, Benjamin Leporq¹, Frank Pilleul^{1,2}, Vincent Grégoire³, Olivier Beuf¹

¹INSA-Lyon, Université Claude Bernard Lyon 1, UJM-Saint Etienne, CNRS, Inserm, CREATIS UMR 5220, U1294, F-69621, LYON, France, Lyon, France. ²CRLCC Léon Bérard – Département de Radiologie, Lyon, France. ³CRLCC Léon Bérard – Département de Radiothérapie, Lyon, France

Abstract

Purpose

Radiomics has gained notable momentum in the field of oncology over the past decade, emerging as a significant area of research in cancer studies. Our aim is to exploit radiomics for survival prediction and risk stratification in glioma, employing classical and novel approaches.

Methods

The UPENN-GBM cohort from TCIA (The Cancer Imaging Archive) was utilized in this study [1]. This dataset includes magnetic resonance imaging (MRI) scans, including T1, T1-Gd, T2, T2-FLAIR, DSC, and DTI, from 611 de novo glioblastoma patients. The automatic and manually corrected segmentation of distinct tumor sub-regions including: Tumor core, Enhancing tumor and Invasion was available for all patients.

Conventional and voxel-wise radiomics were extracted from each tumor sub-region and the entire tumor volume using PyRadiomics v3.1.0 [2], with the default extraction parameters (binWidth: 25; resampledPixelSpacing: disabled; weightingNorm: none). For voxel-wise radiomics, two distinct approaches were utilized. In the first approach, the average voxel value was calculated for each feature. In the second approach, K-means clustering (K=3) was applied to features extracted from the entire tumor volume to generate distinct tumor habitats (figure 1), and the volume of each habitat was calculated. Pearson correlation analysis (correlation coefficient > 0.9) was applied to identify and eliminate highly correlated features. The remaining features, along with patient age, were then used as predictors in a Cox regression model.

To build the models, every possible combination of two and three predictors was evaluated. Four-fold cross-validation was employed to enhance the reliability of the results. Patients were divided into low- and high-risk groups based on risk scores predicted by the Cox proportional hazards model.

Results

Radiomics features were extracted using two different MRI acquisitions (gadolinium-enhanced T1- and T2-weighted images).

The C-index for the best models ranged from 0.647 to 0.654 (95% CI: 0.534–0.751; $P < .0001$) in conventional radiomics and from 0.643 to 0.655 (95% CI: 0.530–0.753; $P < .0001$) in spatial radiomics. While for the habitats-based approach the C-index for the best models ranged from 0.635 to 0.639 (95% CI: 0.526–0.738; $P < .0001$) (figure 2).

Conclusion

All radiomics approach offered comparable results, with the classical method having a slight edge on both spatial radiomics approach, and the same can be said for the two weighting mechanisms. However, there were differences in model's performance when features are extracted from the different tumor sub-regions, which is mainly due to tumor heterogeneity. This observation highlights the potential for exploiting radiomics in dose painting. Although these results can be further improved by including more predictors in the model, our goal was to keep the model as simple as possible which will facilitate the reproducibility of generalization of the results.

Acknowledgements

LabEx PRIMES (ANR-11-LABX-0063), HERESP ANR (ANR-22-CE19-0027-01) and LyRICan (INCa-DGOS-INSERM-ITMO cancer 1803)

References

1. Bleeker, Fonnet E., Remco J. Molenaar, and Sieger Leenstra. "Recent advances in the molecular understanding of glioblastoma." *Journal of neuro-oncology* 108 (2012): 11-27.
2. Van Griethuysen, Joost JM, et al. "Computational radiomics system to decode the radiographic phenotype." *Cancer research* 77.21 (2017): e104-e107.



THE 11TH ANNUAL SYMPOSIUM ON MAGNETIC RESONANCE IN RADIATION THERAPY

Proffered 6: Clinical Studies and Applications in MRgRT Part 2

Low-field (0.55T) respiratory-resolved and pulmonary functional MRI for lung radiotherapy

Jessica Scholey¹, Xin Miao², Dominique Baria³, Prachi Deo³, Yoo Jin Lee³, Pan Su⁴, Jonathan Liu³, Brendan Huang⁵, Lisa Singer¹, Yang Yang³, Peder Larson³, Jae Ho Sohn³, Dante Capaldi¹

¹Department of Radiation Oncology, University of California San Francisco, San Francisco, USA.

²Department of Radiology, Children's Hospital Los Angeles, Los Angeles, USA. ³Department of Radiology and Biomedical Imaging, University of California, San Francisco, San Francisco, USA.

⁴Siemens Medical Solutions, Malvern, USA. ⁵Department of Pulmonology, University of California San Francisco, San Francisco, USA

Abstract

Purpose: Low-field (0.55T) magnetic resonance imaging (MRI) has shown significant potential for lung imaging due to reduced susceptibility artifacts relative to MRI at higher field strengths. For radiotherapy applications, respiratory-resolved (4D-MRI) may provide adequate contrast and geometric fidelity for accurate internal-target-volume (ITV) generation while Fourier-decomposition (FD) MRI may provide ventilation and perfusion information for pulmonary functional avoidance. The purpose of this study was to report on a free-breathing, non-contrast, radiotherapy-specific lung MRI protocol including 4D-MRI and FDMRI for ventilation and perfusion mapping.

Methods/Materials: All scans were performed on a 0.55T MRI scanner (MAGNATOM Free.Max, Siemens Healthcare, Erlangen, Germany). **4D-MRI:** Continuous free-breathing acquisition was achieved using a T1-weighted 3D fast gradient-echo sequence with golden-angle stack-of-stars sampling (TE/TR/flip angle=2.5ms/4.9ms/30°; FOV=380mm², matrix=256x256, slice thickness=3mm, slices=68, 2000 radial views; ~10min). A k-space self-gating signal was used as a respiratory motion surrogate. A prototype amplitude-binning algorithm accounting for hysteresis was applied. **FDMRI:** Multi-slice coronal MRIs were acquired under free-breathing using an optimized commercially available balanced-steady-state free-precession (bSSFP) sequence (TE/TR/flip-angle=1.33ms/231.3ms/30°; FOV=500mm²; matrix=128x128, BW=1395Hz/pixel; slice thickness=15mm; 90s). FDMRI analysis was performed using an inhouse software and the ventilation- (VDP) and perfusion-defect-percent (QDP) were generated using a hierarchical k-means clustering approach to extract ventilation and perfusion defect volumes and seeded region-growing to segment thoracic cavity volumes. Quantitative comparisons between volunteers and lung cancer patients were performed using unpaired t-tests. **Subjects:** A respiratory motion phantom (QUASAR, Modus QA, London, ON, Canada) was used as geometric ground truth for 4D-MRI assessment using sinusoidal waveforms with a peak-to-trough amplitude of 20mm. Twenty patients with lung disease were prospectively recruited for 4D-MRI. Twelve patients with lung-cancer and 14 volunteers were prospectively recruited for ventilation perfusion mapping. **Statistical Analysis:** Quantitative comparisons of VDP and QDP between volunteers and patients with lung disease were performed using Mann-Whitney U-tests (significance p<0.05).

Results: **4D-MRI:** All datasets were reconstructed successfully into 4D images that showed no obvious artifact, suggesting the reliability of k-space SGS extraction. The phantom ground truth and 4D-MRI-derived ITVs measured 31.4cc versus 31.3cc, respectively. Example axial, sagittal, and coronal 4D-MRIs at peak-exhale and peak-inhale are shown in Figure 1, demonstrating qualitative visibility of pulmonary lesions and ability to capture respiratory-induced motion. **FDMRI:** Low-field FDMRI ventilation and perfusion maps showed visible ventilation heterogeneity (i.e., V/Q mismatch) in lung-cancer patients as compared to volunteers. Ventilation and perfusion pulmonary defects can be observed in regions exposed to high doses of radiation, as shown in Figure 2. Quantitatively, as compared to volunteers, both VDP (healthy=2.0±0.9%, lung-cancer=6.8±3.9%; p<0.0001) and QDP (healthy=3.2±1.0%, lung-cancer=9.1±5.0%; p=0.0002) were significantly elevated in lung-cancer patients.

Conclusion: Low-field 4D-MRI can provide high-quality respiratory-resolved imaging and ITV estimations, while FDMRI-derived ventilation and perfusion defects were qualitatively visible and quantitatively elevated in lung-cancer as compared to volunteers. These advancements underscore low-field MRI's unique potential for accessible, high-quality, non-contrast, free-breathing techniques for radiotherapy treatment planning of lung cancer.

Deliverability of biologically guided RT plans driven by quantitative MR imaging

Yutong Zhao¹, Annette Haworth^{2,3}, Pejman Rowshanfarzad^{1,4}, Hayley M. Reynolds⁵, Yu Sun², Scott Williams^{6,7}, Martin A. Ebert^{1,4,8}

¹The University of Western Australia, Crawley, Australia. ²The University of Sydney, Sydney, Australia. ³Sydney West Radiation Oncology Network, Westmead, Australia. ⁴Centre for Advanced Technologies in Cancer Research (CATCR), Perth, Australia. ⁵The University of Auckland, Auckland, New Zealand. ⁶University of Melbourne, Melbourne, Australia. ⁷Peter MacCallum Cancer Centre, Melbourne, Australia. ⁸Sir Charles Gairdner Hospital, Nedlands, Australia

Abstract

Purpose: The concept of defining treatment prescriptions based on biological target volumes dates back more than 20 years¹. Clinical translation of this concept was hampered by lack of high-quality imaging that had poor resolution and had limited accessibility. Validation of the approach was also a prohibiting factor. Advances in MR imaging, and in particular, the rise of quantitative imaging, has provided a quantum leap towards realising biologically guided radiation therapy (BgRT) into mainstream RT. With access to AI models capable of transforming multiparametric MRI into 3D maps of biological characteristics, we investigated the potential of five different, commonly used treatment modalities to deliver BgRT treatment plans

Methods: Within this in silico study, MR data from three high risk prostate cancer patients were used to produce 3D tumour cell density maps. These patients were selected from a cohort of 63 patients scheduled for prostatectomy and represented tumour volumes of 3.2 cc, 4.6 cc and 10.4 cc. The tumour cell density maps were generated from an AI model created using the 63-patient cohort through correlation of imaging features from the *in vivo* MR data (including T2w, DWI and DCE) and histology data. The tumour density maps were scaled based on the patient-specific disease risk factor. A tumour control probability (TCP) model and biological optimisation was used to generate a non-uniform dose distribution through the tumour volume accounting for tumour heterogeneity. To assess the deliverability of the highly modulated dose distributions, three substructures were created based on discrete dose thresholds generated from 15 dose levels evenly spaced between 35 Gy and 50 Gy, to be delivered in five fractions. Dose constraints for organs at risk were consistent with those used in the hypo-FLAME study². An assumption was made that treatments would be delivered with fiducial marker tracking technology. Treatment plans were created to be delivered using Elekta Versa, CyberKnife, Helical Tomotherapy (TOMO), intensity modulated proton therapy (IMPT), and Varian TrueBeam (encompassing two separate centres). The plans, generated with a heterogeneous tumour dose distribution, were compared with a standard homogeneous intra-prostatic lesion (IPL) boost dose prescription².

Results: The TCP for all homogeneous plans was > 90% and consistent with the reported 5-year biochemical control rates of the hypo-FLAME study² (93%). Compared with the homogeneous dose

plans, 67% of heterogeneous dose plans achieved higher TCPs. Patients with larger tumour volumes gained the greatest advantage from the heterogeneous approach suggesting this method has the potential to decrease toxicity whilst maintaining high rates of tumour control.

Conclusions: Multiparametric MRI shows promise in advancing BgRT into clinical practice. This study demonstrates a planning pipeline is feasible with robust treatment plans deliverable using standard treatment modalities and tumour tracking technology.

1. Ling, C.C., et al., *Towards multidimensional radiotherapy (MD-CRT): IJROBP* 2000.
2. Draulans, C., et al. Stereotactic body radiotherapy with a focal boost to the intraprostatic tumor for intermediate and high risk prostate cancer: *Radiother Oncol* 2024.

Evaluating T1 and T2-weighted MR images for improved liver GTV delineation and subsequent ITV generation using a novel 4D multitasking MR sequence

Theodore Geoghegan¹, Wensha Yang¹, William Chen¹, Jessica Scholey¹, Mary Feng¹, Zhaoyang Fan², Junzhou Chen²

¹University of California, San Francisco, San Francisco, USA. ²University of Southern California, Los Angeles, USA

Abstract

Purpose: Delineating gross tumor volumes (GTVs) on computed tomography (CT) images for free-breathing liver stereotactic body radiation therapy (SBRT) is suboptimal due to the poor contrast between healthy and cancerous liver tissues. Likewise, generating 4DCT-based internal target volumes (ITVs) is also suboptimal. Therefore, breath-hold (BH) T1-weighted (T1w) MR images are often required to assist GTV delineation. However, liver tumors of different diagnoses demonstrate varying degrees of hyper- and hypo-intensities in T1w and T2w images, implying uncertainty in tumor delineation if only one sequence is utilized. A novel multi-tasking (MT)MR imaging technique was implemented on a 3-Tesla MR simulator, providing T1, T2, and proton density-weighted (PDw) 4DMR images in a single 8-minute free-breathing scan. We have previously shown that MTMR can provide more accurate tumor delineation and motion evaluation than 4DCT. This study further assesses the value of the T2w images for ITV generation and their potential impact on liver SBRT planning.

Methods: Clinical MR protocol included BH pre- and post-contrast T1w MR and a research pre-contrast free breathing MTMR. The MTMR sequence implemented in this investigation utilizes a multi-tasking low-rank tensor framework, allowing inherently registered and respirations-correlated T1w, T2w, and PDw 4DMR sequences in one scan. Tumor contrast-to-noise ratio (CNR) was quantified using , where and are average image intensities of three random points within the tumor and healthy liver, respectively, and is the standard deviation of the background noise measured outside the body. GTVs were contoured and analyzed in MIM™ (MIM Software Inc., Cleveland, Ohio). The BHT1w BHT2w images were then registered to the exhale bins of the MTMR-T1w and MTMR-T2w, respectively. A deformable propagation was then applied to map GTV to other respiratory bins, and ITV was created by the union of all GTVs.

Materials: A single radiation oncologist delineated GTVs on the post-contrast, BH-T1w, and BH-T2w scans for 17 patients, demographics shown in Tab. 1. The image resolution for the BHT1w and BHT2w images were 1.25x1.25x3 mm³ and 1.56x1.56x6 mm³, respectively. The MTMR had an image resolution of 1.6x1.6x3.2 mm³.

Results: As shown in Fig. 1a, GTVs drawn on T1w or T2w resulted in similar average volumes across the patient sample, 119.31 cc and 118.76 cc, respectively. Although the volumes are similar, differences exist, and there is no consistent trend in one direction or another, even when grouped by diagnosis. This

suggests there is no single sequence that entirely encapsulates the physiology of the tumor, and the MTMR sequence can offer complementary tumor visualization across diagnoses. As shown in Fig. 1b, BH-T1w and BH-T2w GTVs both displayed similar CNR magnitudes, -73.45 and 74.88, respectively, both of which are much higher than CT at -1.29. Figure 2 illustrates the variability in GTV delineation between T1w and T2w images for patients with metastases (2a) and ICC (2b)

Conclusion: The MTMR sequence was successfully implemented on our MR simulator. For patients who struggle with BH treatments, MTMR may translate into improved tumor and motion definition and more accurate PTV coverage in free-breathing liver SBRT, compared to 4DCT.



THE 11TH ANNUAL SYMPOSIUM ON MAGNETIC RESONANCE IN RADIATION THERAPY

Proffered 7: Quantitative MRI Part 2

Repeatability of longitudinal apparent diffusion coefficient measurements in esophageal tumors on a 1.5 T MR-linac

Koen Kuijter, Astrid van Lier, Lieke Meijers, Stella Mook, Gert Meijer

University Medical Centre Utrecht, Utrecht, Netherlands

Abstract

Purpose

Changes in apparent diffusion coefficient (ADC) values show promise as a biomarker for assessing response after neoadjuvant treatment in esophageal cancer but currently lack the accuracy needed for clinical decisions, such as omitting esophagectomy in cases of pathological complete response. Most studies evaluating ADC changes rely on only two measurements. The advent of MR-linac systems enables ADC measurements at each treatment fraction, offering the potential for more robust response assessments. This study evaluated the repeatability of ADC measurements in esophageal tumors using a 1.5T MR-linac and examined the impact of longitudinal ADC measurements on ADC change assessments.

Materials and Methods

Six esophageal cancer patients (three receiving 23 fractions and three receiving 28 fractions) underwent treatment on a 1.5 T MR-linac (Unity, Elekta AB, Sweden). Two consecutive diffusion-weighted scans (b -values: 0, 150 and 500 s/mm^2 , voxel size: $2.0 \times 2.0 \times 5.0 mm^3$, and no respiratory triggering) were acquired daily, except once a week, resulting in 17 or 22 scan days per patient. ADC-maps were calculated using a mono-exponential fit of the b -values 150 and 500 s/mm^2 , excluding ADC values below 0 s/mm^2 . For each session, a volume-of-interest encompassing the primary tumor was manually delineated on the b500 scan.

The absolute and relative repeatability coefficient (RC, relRC) for median ADC values within the volumes-of-interest were calculated. Changes in median ADC relative to fraction one were calculated, with the repeatability assessed using Bland-Altman analysis and the RC. Additionally, linear regression lines were fitted through all median ADC values of both sessions to calculate regression-based ADC changes, with differences between sessions analyzed using Bland-Altman analysis.

Results

Of the 120 scan days, both sessions were successfully acquired in 106 fractions. Missing scans were due to insufficient time in the workflow to complete the second session (8), selection of the incorrect examcard (5), or technical failure (1).

The RC for median ADC values was 0.38×10^{-3} mm²/s, and the relRC was 23.5%. Figure 1 depicts changes in median ADC values throughout treatment for the first three patients. For relative ADC changes based on two measurements, the RC was 27.4 percentage points (%pt), with a session-to-session bias of -5.0 %pt and 95% limits of agreement ranging from -32 to 22 %pt (Figure 2). In contrast, the maximum difference between sessions was 11.5 %pt when based on regression assessments. Although the available data are insufficient to determine the RC for regression-based assessments, this approach yielded more consistent estimates of ADC changes for all patients.

Conclusions

The relRC of median ADC values in esophageal tumors measured on a 1.5T MR-linac was 23.5%. Relative ADC changes based on two measurements demonstrated substantial variability with a RC of 27.4 %pt, limiting their reliability for accurate response assessment. However, using regression-based approaches to analyze longitudinal ADC measurements greatly improved the consistency of ADC change assessments. Daily ADC measurements facilitated by MR-linac systems provide a more stable and accurate method for evaluating treatment response in esophageal cancer, underscoring the potential of these systems to enhance clinical decision-making.

Preliminary Results from Consensus Measurement Methods for Longitudinal relaxometry on the 1.5T Unity MR-linac: a multi-institution comparison

M.J. van Rijssel¹, T.C. Salzillo², W. Foltz³, E.D. Subashi², E. van der Bijl⁴, M. Kruiskamp⁵, A.L.H.M.W. van Lier¹, E. Paulson⁶, B. Stemkens⁷, M.E.P. Philippens¹

¹UMC Utrecht, Utrecht, Netherlands. ²UT MD Anderson Cancer Center, Houston, USA. ³UHN, Toronto, Canada. ⁴RadboudUMC, Nijmegen, Netherlands. ⁵Philips, Best, Netherlands. ⁶MCW, Milwaukee, USA. ⁷Elekta, Best, Netherlands

Abstract

Purpose

The Elekta Unity MR-Linac combines a 1.5T MRI with a linear accelerator for simultaneous MR-imaging and external beam radiotherapy [1]. It provides the potential for online adaptive radiotherapy planning and delivery based on quantitative imaging biomarkers (QIBs) [2]. A multi-institutional task group now pursues a consensus protocol for T1 and T2 quantification in a fast but reliable manner, enabling relaxation based QIBs. This work summarizes progress towards a T1 consensus protocol, including identification of candidate techniques and their evaluations using the ISMRM-NIST phantom [3].

Methods

The task group developed a protocol for T1 mapping after several consensus meetings and is evaluating inter- and intra institutional reproducibility and accuracy of 4 methods (Table 1). The phantoms were imaged thrice in institute A on two MR-Linacs and twice in institute B. Gold-standard methods, IR and MIX, were performed in institute A only.

Flip angles for DESPOT1 were corrected using the AFI method [4], and via compensation for incomplete RF spoiling (RFS) at short TR [5]. Analysis was limited to the central slice, consisting of a one-pixel erosion from manually segmented ROIs drawn on each individual sample. Per sample T1 bias was calculated as the difference between mean T1 and the vendor-supplied reference. Repeatability (within-subject deviation) and reproducibility (within-subject coefficient of variation) were calculated according to QIBA recommendations [6] for multi-institutional data (only for DESPOT1 and MIRACLE).

Results

For vial T1-5 (T2=446 ms), T1 bias was 42, -57, -6, and 2 ms for MIRACLE, DESPOT1, MIX and IR respectively. Due to fundamental AFI and RFS model limitations ($TR_1 < TR_2 = 150 \text{ ms} < T_1$ for AFI; RFS compensation derived with $T_2 = 85 \text{ ms}$), DESPOT1 showed relatively large bias and precision for spheres outside the range of $70 < T_2 < 500 \text{ ms}$ and $T_1 > 150 \text{ ms}$. Outside of these ranges, DESPOT1 biases breached $31\% \pm 45\%$. MIRACLE has low performance at long T2s due to aliasing across the phase cycles, an increased TR would lead to a higher accuracy for long T2s at the expense of longer scantimes. Further analysis was therefore constrained to nine spheres with $70 < T_2 < 500 \text{ ms}$ and $T_1 > 150 \text{ ms}$ (Figure 1).

Within the constrained sphere set, MIRACLE T1 and DESPOT1 biases were similar (11+-100 ms vs -24+/-146 ms; -2+-12% vs 0+-13%). For DESPOT1, T1 bias compensation was nominal from AFI, but considerable from RFS (-208+/-225ms, no compensation; -242+/-245 ms, AFI-only; 22+/-156 ms, RFS-only; -24+-146 ms, AFI+RFS). Even with these corrections, each of the DESPOT1 T1 maps presented a similar scaling of percentage bias with reference T2 at both sites (Figure 2).

DESPOT1 presented with better reproducibility and repeatability (153+/-245 ms and 10+-10% for MIRACLE; 32+-26 ms and 3+-2% for DESPOT1). Tighter physiologic constraints to reference T2 improved MIRACLE repeatability and reproducibility (27+-34 ms and 7+-4% for spheres with 8<T2<230 ms; T1<1200 ms). Results compare favorably to QIBs in literature: reproducibility is 17% for ADC, 20% for k-trans in prostate [6].

Conclusion

Consensus protocols have been developed for T1 relaxometry on the Unity MR-Linac. Both DESPOT1 and MIRACLE show promise for T1 mapping, but methodologic limitations must be accounted for.

Longitudinal Assessment of Diffusion-MRI Hypoxia Score in Patients with Prostate Cancer Receiving Definitive Radiotherapy

Ivan A Rashid¹, Sacha af Wetterstedt^{1,2}, Erik Thimansson³, Camilla Thellenberg Karlsson⁴, Karin Söderkvist⁴, Tufve Nyholm⁴, Patrik Brynolfsson^{1,2}, Adalsteinn Gunnlaugsson^{5,6}, Lars E Olsson^{1,2}

¹Department of Translational Medicine, Medical Radiation Physics, Lund University, Malmö, Sweden. ²Radiation Physics, Department of Hematology, Oncology and Radiation Physics, Skåne University Hospital, Lund, Sweden. ³Department of Translational Medicine, Diagnostic Radiology, Lund University, Malmö, Sweden. ⁴Department of Diagnostics and Intervention, Oncology, Umeå University, Umeå, Sweden. ⁵Department of Clinical Sciences, Radiation Therapy, Lund University, Lund, Sweden. ⁶Oncology, Department of Hematology, Oncology and Radiation Physics, Skåne University Hospital, Lund, Sweden

Abstract

Purpose

In an ongoing prospective clinical trial, very high-risk prostate cancer patients receive a GnRH-antagonist for androgen deprivation therapy (ADT) along with radiotherapy to the prostate, including a focal boost to the intraprostatic lesion. The purpose of this study was to present longitudinal hypoxia-MRI assessments of the intraprostatic lesion at three time points during the treatment for the first five patients.

Methods

Five patients with PI-RADS 4-5 lesions underwent three MRI examinations on a 3T Signa Architect (GE Healthcare, Milwaukee, WI, USA) with the 30 channel AIR anterior array coil in combination with the denoising reconstruction AIR Recon DL.

The MRI examinations were scheduled as follows. MRI-1 for treatment planning followed by the start of ADT. MRI-2 two weeks after start of ADT, in conjunction with start of radiotherapy. MRI-3 within 48 hours after 4 of the 7 fractions of ultra-hypofractionated radiotherapy (prostate 42.7 Gy, intraprostatic lesion 49.0 Gy, pelvic lymph nodes 29.4 Gy and seminal vesicles 31.2 Gy).

An empirical consumption and supply-based hypoxia model using the intravoxel incoherent motion (IVIM) diffusion model was previously developed and validated¹. The perfusion fraction f , describes the voxel fraction occupied by capillaries, and the diffusivity D correlates inversely with cell density. Low f and D indicate poor oxygen supply and high cell density, hence a high probability of tissue hypoxia.

DWI for IVIM analysis was acquired with b-values 0, 50, 200, 800 s/mm², 3 directions, 5 repetitions. A segmented bi-exponential fitting approach was used for parameter estimation.

A Euclidean approach was used to calculate voxel-wise hypoxia scores ($HS_{\text{Euclidean}}$) according to Mo et al.², through histogram analysis of f and D in whole-prostate ROIs. The lower and upper thresholds of f and D for $HS_{\text{Euclidean}}$ determined by the 1st and 99th percentiles of the pooled parameter distributions of all five patients. D_{low} , D_{high} were 0.6 and 2.0 1e-3mm²/s, respectively, and $f_{\text{low}}, f_{\text{high}}$ was 0 and 37%, respectively.

ROIs representing the intraprostatic lesion were contoured by an experienced oncologist and radiologist for each patient on the first MRI examination. The ROIs were propagated to the later examinations by affine registration to the unweighted DWI of the subsequent examinations.

Results

Longitudinal changes in the IVIM parameters f and D , and the hypoxia scores were both visually depicted and quantifiable in the tumor ROI. Three of five patients had a median f decrease (3 – 6%). For one patient the median f increased by 5%. All patients had a median D increase (0.1 – 0.4 1e-3mm²/s). Between MRI-1 and MRI-3 the median $HS_{\text{Euclidean}}$ decreased in four patients by 0.10, with the largest decrease between MRI-2 and MRI-3. One patient had a median $HS_{\text{Euclidean}}$ increase by 0.04.

Conclusions

These are the preliminary results of the first five patients. Diffusion-MRI-based hypoxia mapping revealed longitudinal changes in tumor hypoxia. This is to the best of our knowledge the first time longitudinal changes in diffusion-MRI hypoxia score have been measured in prostate cancer during ADT and radiotherapy.

¹Hompland et al. *Cancer Res.* 2018;78(16).

²Mo et al. *Cancers (Basel)*. 2022;14(5).

Early radiation induced changes to the microenvironment in cervical cancer patients

Tiril Hillestad¹, Kjersti Lund², Heidi Lyng¹, Tord Hompland¹

¹Institute for Cancer Research, Oslo University Hospital, Oslo, Norway. ²Department of Radiology and Nuclear Medicine, Oslo University Hospital, Oslo, Norway

Abstract

Purpose/Objective

Radiotherapy (RT) is a successful treatment of cervical cancer (CC), but due to tumor radiation resistance about 1 in 3 patients are not cured. Today all CC patients receive the same treatment regimen, fractionated external RT (2 Gy x 25), followed by brachy therapy.

To improve cure rates and achieve a more personalised treatment approach there is need for a biomarker to select the patients that are not cured by standard treatment. Tumour hypoxia from MR images obtained prior to treatment provides strong prognostic information and is precise in selecting patients with a good prognosis [1]. The more hypoxic patients have a poor prognosis, however, more than 50 % of these patients are cured. A more precise biomarker within hypoxic patients could provide even better candidates for treatment intensification studies. Here we investigate if an early treatment response by MR imaging and cell density from biopsy (1 week into treatment) can provide prognostic information that are not available at baseline.

Material/Methods

MR imaging, including anatomical T2 weighted (T2w) imaging and dynamic contrast enhanced (DCE) MR was performed in 25 CC patients before RT and again after receiving a total dose of 10 Gy. From DCE MR data the Tofts parameters K^{trans} , reflecting perfusion, and V_e , reflecting the extracellular volume fraction, were derived. Tumour volume was obtained from T2w images. Furthermore, a biopsy was obtained at the same time points, and cell density (CD) was estimated from immunohistochemistry slides.

Results

After 10 Gy all patients had a decrease in CD ($p<0.001$), however this was not reflected in tumor volume as no significant reduction was found ($p=0.95$). V_e , which has been shown to negatively correlate with CD, increased by 19% but this was not statistically significant ($p=0.067$). Reperfusion is thought to be an important factor of fractionated RT and median K^{trans} increased by 28% ($p=0.011$). 4 patients experienced tumor recurrence and was classified as non-responders. Responders had a significantly higher increase in K^{trans} than non-responders ($p=0.008$). There was no difference in CD, V_e or tumor volume between responders and non-responders.

Conclusion

After 10 Gy significant changes were observed in parameters reflecting the tumor microenvironment

that were independent of tumor volume changes. An increase in tumor perfusion, K^{trans} , was higher in responders than non-responders and may be a promising biomarker for tumor response to RT. These results may provide a rationale for repeated MR imaging of hypoxic high-risk patients after 1 week of RT to evaluate the need for intensified treatment.

References

- [1] Skipar K. et al. Risk of recurrence after chemoradiotherapy identified by multimodal MRI and 18F-FDG-PET/CT in locally advanced cervical cancer. Radiother Oncol;2022;176:17-24

Longitudinal Diffusion-Weighted MRI for Treatment Response Assessment in Locally Advanced Rectal Cancer Patients Undergoing Short-Course Radiotherapy

Jonathan Pham, Huiming Dong, Ann Raldow, Sharon Qi

UCLA, Los Angeles, USA

Abstract

Purpose: To investigate the longitudinal changes in apparent diffusion coefficient (ADC) as an early predictor of treatment response in patients with locally advanced rectal cancer (LARC) undergoing short-course radiotherapy (SCRT) followed by total neoadjuvant therapy (TNT).

Methods: A pilot cohort of ten LARC patients enrolled in a prospective clinical trial (NCT04703101) were included in the study. All patients were planned and treated on a low-field 0.35T ViewRay MR-guided LINAC, with a prescription of 25 Gy in 5 fractions followed by 16 weeks of mFOLFOX. Diffusion-weighted MRIs (DWI) were acquired using a fine-tuned diffusion-weighted single-shot echo-planar-imaging (DW-ssEPI) sequence with b-values of 0, 300, 500 s/mm² at 3 time points: 1) simulation (baseline), 2) 3rd fraction, and 3) 5th fraction of radiotherapy treatment. Rectal gross tumor volumes were contoured on the planning and fractional MRI at each timepoint, with mean ADC measured on registered ADC map. Patients were categorized as either clinical complete response (cCR) or incomplete response based on their actual treatment outcomes, which were assessed 8-12 weeks after the completion of neoadjuvant therapy using digital rectal examination endoscopy and MRI. Longitudinal ADC and ADC change were analyzed for correlation with post-treatment response. The mean ADC treatment response prediction threshold was determined at the optimal operating point of the ROC curve. Additionally, ADC quantification was validated using a Diffusion Phantom (CaliberMRI Inc.), comprising of vials of 0-50% polyvinylpyrrolidone (PVP) concentration and MR-readable liquid crystal thermometer.

Results: In the pilot SCRT cohort, four out of ten (40%) LARC patients achieved a cCR. An increase in ADC was associated with cCR. The mean ADC at the 5th fraction was observed to be the most predictive of treatment response, with an area under the curve (AUC) of 0.83, where the final ADC threshold of 1.32×10^{-3} mm²/s demonstrated an accuracy, sensitivity, and specificity of 0.80, 0.75, and 0.83 respectively. Additionally, DW-ssEPI mean ADC bias (error) and within-subject Coefficient of Variation (wCV) were measured using the Diffusion Phantom, yielding values of $1.47 \pm 3.59\%$ and $1.35 \pm 0.89\%$, respectively.

Conclusion: Longitudinal ADC may be used as a non-invasive predictor for early treatment response inpatients undergoing SCRT. Monitoring ADC trend may allow for tailored treatment such as non-operative management (NOM) in LARC patients who achieved a complete response, reducing the need for radical surgery and its associated morbidities.

Monitoring Concurrent Chemoradiation Treatment Response in Cervical Cancer Using Quantitative 3D T1p Mapping

Sandeep Panwar Jogi¹, Vonetta Williams², Qi Peng³, Ricardo Otazo^{1,4}, Marisa Kollmeier², Victoria Yu¹, Can Wu¹

¹Department of Medical Physics, Memorial Sloan Kettering Cancer Center, New York, USA.

²Department of Radiation Oncology, Memorial Sloan Kettering Cancer Center, New York, USA.

³Department of Radiology, Albert Einstein College of Medicine and Montefiore Medical Center, Bronx, New York, USA. ⁴Department of Radiology, Memorial Sloan Kettering Cancer Center, New York, USA

Abstract

PURPOSE

Cervical cancer, primarily caused by oncogenic human papillomavirus (HPV), remains a leading cause of mortality among women. About 60% of patients with advanced tumors (>4 cm) achieved a 5-year disease-free survival rate despite receiving standard care, which includes concurrent chemoradiation therapy (CCRT) followed by brachytherapy. T2-weighted and diffusion-weighted MRI can be useful for monitoring treatment response in cervical cancer. However, inflammation caused by treatment often leads to misleading changes in T2-weighted imaging, and diffusion-weighted imaging is sensitive to susceptibility-related distortions. Thus, exploring other MR tissue parameters is necessary. T1 relaxation is sensitive to macromolecule-water interactions and has demonstrated promise in detecting early treatment responses in rectal and head-neck cancers. However, its potential for evaluating cervical cancer treatment remains unexplored. The aim of this study is to investigate 3D T1p mapping within a clinically feasible scan time and to monitor the response to CCRT in cervical cancer patients.

METHODS

Seven HPV+ cervical squamous cell carcinoma patients (52.7 ± 14.7 years) consented to an IRB-approved study. Each patient received concurrent chemoradiotherapy (45 Gy to the pelvis, 56.25 Gy nodal boost if needed) and weekly cisplatin (40 mg/m^2).

Image Acquisition: MRI scans were performed pre-treatment and weekly during the five-week CCRT using a 3T MRI scanner equipped with anterior and in-table posterior torso coils (Philips Healthcare). The protocols included T2-weighted imaging for treatment planning and fat-suppressed 3D T1p imaging for treatment response. T1p imaging was based on a MAPSS (magnetization-prepared angle-modulated partitioned k-space spoiled gradient-echo snapshots) sequence, with four pairs of spin-lock times (± 0 , ± 30 , ± 60 , ± 80 ms) and a spin-lock frequency of 300 Hz, completed in approximately 5 minutes.

Data Processing: In-house software was used to calculate T1p maps using a mono-exponential fitting to T1p-weighted complex-valued data. An expert radiation oncologist (VW) delineated the tumor volumes on T2-weighted images at each imaging time point using MIM Maestro software (MIM Software Inc.,

Cleveland, USA). The T1 ρ maps were then imported into the MIM software and rigidly registered to the T2-weighted scans, enabling the transfer of the delineated tumor contours onto the T1 ρ maps.

Data Analysis: The mean and standard deviation of the T1 ρ values (ms) and tumor volumes (mL) were measured for each scan. Tumor T1 ρ values were normalized to posterior muscle values to account for residual field inhomogeneity.

RESULTS

The average T1 ρ value across the seven patients decreased each week during treatment. The mean pre-treatment T1 ρ value was 82.54 ± 9.78 ms, which decreased by 5.72% (week 1), 6.81% (week 2), 11.32% (week 3), 20.75% (week 4), and 24.59% (week 5). Tumor volume exhibited a similar trend, with a pre-treatment mean of 77.29 ± 51.98 mL, reduced by 5.54% (week 1), 36.54% (week 2), 60.90% (week 3), 72.13% (week 4), and 86.88% (week 5).

CONCLUSION

This work demonstrates that quantitative T1 ρ imaging has the potential to effectively detect changes induced by CCRT and to monitor treatment response in cervical cancer patients within a clinically feasible scan time.

Assessment of treatment response after prostate Stereotactic Body Radiation Therapy using quantitative MRI and radiomics: the SBRT SI-BiRT trial

Arpita Dutta¹, Giuseppe Sasso^{2,3}, Annette Haworth⁴, David Dubowitz⁵, Jerusha Padayachee², Vikash Patel², Catherine Morgan⁵, Satya Amirapu⁶, Hayley Reynolds¹

¹Auckland Bioengineering Institute, The University of Auckland, Auckland, New Zealand. ²Health New Zealand, Auckland City Hospital, Auckland, New Zealand. ³Faculty of Medical and Health Sciences, The University of Auckland, Auckland, New Zealand. ⁴University of Sydney, Sydney, Australia. ⁵Centre for Advanced MRI, The University of Auckland, Auckland, New Zealand.

⁶Department of Pathology, The University of Otago, Dunedin, New Zealand

Abstract

Purpose: Prostate cancer is the second most common cancer worldwide and was the fifth leading cause of cancer death in men in 2022. Stereotactic Body Radiation Therapy (SBRT) is a high-precision form of radiation therapy (RT) that enables the safe delivery of very high doses of radiotherapy in fewer sessions than conventional RT. While prostate RT has high five-year tumor control rates, the risk of local recurrence increases after five years, and standard prostate-specific antigen (PSA) blood testing may delay detection. Additionally, PSA testing is prone to high false-positive rates and lacks spatial information. We hypothesize that quantitative MRI and MRI-derived radiomic features could more accurately identify early response to prostate SBRT than PSA testing.

Methods: The SBRT Sequential-Imaging Biologically Targeted Radiation Therapy (SI-BiRT) clinical trial (ACTRN12621001118897) is an exploratory study designed to identify potential imaging biomarkers for early treatment response to prostate SBRT. Patients with localized prostate cancer, planned for prostate SBRT (36.25 Gray in 5 fractions) without the use of androgen deprivation therapy, were enrolled into the trial. MRI was acquired pre-treatment and at 6-months and 12-months post-SBRT, including T2-weighted, diffusion-weighted imaging (DWI), dynamic contrast-enhanced (DCE)-MRI, and R2* mapping. Quantitative MRI parameters and MRI radiomic features were extracted to quantify longitudinal changes in follow-up imaging relative to pre-treatment. DWI-derived parameters included the apparent diffusion coefficient (ADC), and parameters from a simplified Intravoxel Incoherent Motion (IVIM) model including diffusion coefficient (D), perfusion fraction (f) and hypoxia score (HS). DCE-MRI parameters included the semi-quantitative parameter time-to-peak (TTP), and pharmacokinetic parameters forward transfer rate constant (Ktrans), reverse transfer rate constant (Kep) and the extracellular extravascular space volume fraction (Ve). An in-vivo test-retest dataset was used to compute repeatability coefficients to determine thresholds for detecting treatment-related changes after prostate SBRT. Blood samples were collected at each imaging timepoint for PSA monitoring and to assess hypoxia, along with biopsy tissue for analysis using immunohistochemistry.

Results: Ten patients with low to intermediate-risk prostate cancer have been recruited to the SBRT SI-BiRT trial and have completed baseline and 6-month follow-up assessments. Analysis of the tumor

region-of-interest shows that six months post-SBRT, there were significant treatment-related changes shown on MRI. In all patients, the DWI-derived parameters ADC and D increased, suggesting lower tumor cellularity, while HS decreased, indicating improved tumor oxygenation. Meanwhile, the DCE-MRI parameter K_{ep} decreased and V_e increased in the tumor for all patients, reflecting reduced perfusion and higher permeability. Treatment-related changes at a voxel-wise level were detected the most frequently in DCE-MRI parameters and R2* maps. Thirty-two radiomic features demonstrated significant changes six months post-treatment, with most of these features being derived from DWI parameters.

Conclusions: Preliminary results from the SBRT SI-BiRT trial support the use of quantitative MRI and MRI-derived radiomic features for accurate and personalized evaluation of response after prostate SBRT. Robust imaging biomarkers would enable early interventions that target radio-resistant disease to reduce the risk of disease progression. Analysis of the 12-month follow-up data along with blood and tissue samples for hypoxia assessment will be completed in 2025.



THE 11TH ANNUAL SYMPOSIUM ON MAGNETIC RESONANCE IN RADIATION THERAPY

Proffered 8: Advanced and Specific Topics Part 2

Implementation of Quantitative MRI-Guided Adaptive Radiotherapy on MR-LINAC

Jie Deng, Yan Dai, Yen-Peng Liao, Junjie Wu, Chris Kabat, Jill De Vis, Fan-Chi Su, Mu-Han Lin, Andrew Godley

UT Southwestern Medical Center, Dallas, USA

Abstract

INTRODUCTION:

MRI is increasingly used to enhance image-guided radiation therapy, from initial dosimetry treatment planning through MR simulation to offline replanning. Integrating MRI with linear accelerator (MR-LINAC) systems enable in-treatment MRI, allowing for adaptation of daily dosimetry plans to accommodate anatomical and disease state changes, advancing MRI-guided radiation therapy (MRgRT)¹. However, anatomy-based adaptive radiotherapy (ART) has limitations, including underestimating tumor extent, unable to identify tumor subregions with varied biological resistance, thus delaying optimal plan adaptation. Functional adaptation has emerged to integrate biological insights into the ART process². In this study, we present clinical implementation of integrating diffusion-weighted imaging (DWI) and dynamic enhanced MRI (DCE) into the MRgRT workflow.

METHODS:

Quantitative MRI (qMRI) protocol optimization and rigorous quality assurance were developed using diffusion phantom and T1/T2 phantoms (CaliberMRI) for both 1.5T MR simulator and the MR-LINAC systems. Imaging protocol parameters are provided in **Table 1**. For DWI, the apparent diffusion coefficient (ADC) was calculated using linear fitting, while true diffusion coefficient (D_t) and fractional perfusion (f_p) were derived via non-linear bi-exponential fitting based on the intra-voxel incoherent motion (IVIM) model. An R-index³⁻⁵, calculated as $f_p * 0.69 + D_t / 3.0 * 10^{-3}$, which proved to reflect hypoxia levels in prostate cancer, with threshold values set at $f_p = 0.43$ and $D_t = 0.79 * 10^{-3}$. A cellularity map was created from D_t , as $(3.0 * 10^{-3} - D_t) / 3.0 * 10^{-3}$. For DCE, the IAUC, K_{trans} , and V_p maps were produced based on the Tofts model. Post-processing was performed using in-house software, incorporating patient-specific quality control. DWI and DCE are used during initial treatment planning for target contouring. DWI is integrated into the online adaptation workflow, allowing physicians to refine target contours in real-time.

RESULTS:

Fig. 1 shows a case of initial treatment planning for a glioblastoma multiforme (GBM) patient based on MRI simulation images. The gross target volume (GTV) includes areas within the enhancing rim on post-contrast T1-weighted images, while clinical target volume (CTV) extends to hyperintense regions on T2-weighted FLAIR images.

qMRI maps generated via a script in the treatment planning system (TPS) provides tissue property information such as cellularity and hypoxia levels from DWI and vascular properties from DCE. Adaptive planning for two GBM patients on MR-LINAC is shown in **Fig. 2**, where high dose target regions were defined based on the restricted diffusion areas rather than hyperintense FLAIR or enhancing post-T1 regions. Improved tumor-to-tissue contrast on high b-value images enhances the physician's confidence in refining the target during online adaptive planning.

DISCUSSION:

Dose painting can be used to achieve biological conformality by targeting intratumoral heterogeneity. Regions with high cellularity, high/low perfusion, and hypoxia, which may not be visible on standard post-T1 and FLAIR images, warrant attention and could potentially receive dose escalation. Additionally, online adaptation based on parametric changes in qMRI may guide biological adaptive planning, allowing for treatment adjustments based on responses to previous RT fractions.

CONCLUSION:

We implement qMRI into clinical workflows involving MRI simulation and MR-LINAC treatment, establishing a framework for MR-guided Biology ART in clinical settings to achieve personalized radiotherapy.

Online adaptive MR-Guided radiotherapy on a 1.5 T MR-Linac: clinical experience and evaluation of the first 1000 patients in a monocentric analysis

De-Colle Chiara, Michele Rigo, Andrea Gaetano Allegra, Luca Nicosia, Niccolò Giaj-Levra, Edoardo Pastorello, Francesco Ricchetti, Carolina Orsatti, Andrea Romei, Nicola Bianchi, Riccardo Filippo Borgese, Antonio De Simone, Davide Gurrera, Stefania Naccarato, Gianluisa Sicignano, Ruggero Ruggieri, Filippo Alongi

Advanced Radiation Oncology Department, Negrar di Valpolicella, Italy

Abstract

Purpose/Objective: The clinical implementation of MR-guided radiotherapy on MR-linacs (MRL) has rapidly increased in the recent years. The advantages represented by the MR-based daily online plan adaptation and real-time monitoring have been exploited for different tumour sites¹⁻³. Nevertheless, some concerns remain, mainly related to the longer treatment time and limited patient eligibility due to clinical or technical aspects, e.g. the smaller treatment field size⁴. We report here the experience of our center, where a 1.5T MRL was clinically implemented in 2019 and, since then, more than 1100 patients have been treated.

Material/Methods: The first 1000 patients treated at the MRL in our department were selected. Technical informations such as treatment time and adaptive technic have been prospectively recorded, while toxicity data were retrospectively collected. Median follow up was calculated from the start of radiotherapy (RT). Acute and late toxicity were defined using the cut off of 90 days.

Results: Between October 2019 and June 2024, 1000 patients for a total of 1061 treatment courses were included. Median follow up was 39 months (range, 0-60). Mean age was 69 years (range ,16-90). We irradiated the primary tumour or tumour bed in 72.6% of the cases, lymphnodal metastases in 16%, distant metastases in 7%, while 4.4% of the cases were retreatments. Prostate and prostate bed were irradiated in 67.3% and 10.2% of the cases, respectively, including pelvic lymphnodes in 4.7%. Other targets were tumors of the brain, pancreas, liver, adrenal gland, lung, bladder, kidney, anus/rectum, head and neck and gynecological cancers. The most frequent adopted doses were 36.25Gy (31%), 35Gy (28.3%) and 30Gy (9.4%) in 5 fractions. On a total of 9076 administered fractions, 80.8% were with adapt-to-shape and 19.2% with adapt-to-position method. The mean in-room time was 38 minutes (range, 18-103), with 74.4% of patients completing the session within 40 minutes. Acute grade (G) 3 toxicity was recorded in 1.6% of the cases, while, on a total of 858 patients available for late toxicity, G3 was recorded in 0.3% of the cases, with no >G3.

Conclusion: Our experience confirms that MRL treatments are feasible for different tumour entities in several anatomical sites. We showed that most of the patients could be treated within 40 minutes and that the MRL field size did not limit RT indications when larger targets were prescribed. Treatments were very well tolerated. Protocols for dose escalation and margin reduction, by adopting new comprehensive motion monitoring strategies, are under development.

Bowel motion: Is it a concern for multi-isocenter treatments?

Saskia Damen, Astrid van Lier, Cornel Zachiu, Bas Raaymakers

UMC Utrecht, Utrecht, Netherlands

Abstract

Purpose

While the MR-Linac allows for accurate observation of the treated area over the course of the treatment, its treatment field is currently limited to only 22 cm in craniocaudal direction. This excludes patients with extensive disease, such as pelvic tumors with lymph node involvement¹. A potential solution for this limitation is to move towards multi-isocenter treatments². However, this approach increases treatment times and the risk of dosimetric impact of intra-fractional changes. Due to its high radiosensitivity and mobility, this can become problematic for the small bowel. Previous feasibility studies have shown a 2 cm overlap in structures and 4 cm overlap in dose², which can become a safety concern due to the potential bowel displacements³. Here, we analyze bowel motion and investigate the risk of overdosage in multi-isocenter treatments due to bowel displacements.

Methods

The cohort consisted of 18 patients ($t_{\text{acquisition}} = 7.5 \text{ min.}$, $N = 245 \text{ frames}$) and 10 volunteers ($t_{\text{acquisition}} = 15 \text{ min.}$, $N = 495 \text{ frames}$), all wearing corset (Aspen Lumbar support). For estimating bowel motion we employed a previously-developed framework, showing largest motion in CC, which is also the axis along which multi-isocenter fields overlap. Therefore, we focus on bowel displacements on this axis.

First, the peak-to-peak motion (2.5% - 97.5%) of each voxel was analyzed, giving the near-maximum position difference of each voxel, which we summarized in a motion volume histogram (MVH)⁴. The percentage of voxels experiencing > 2 and 4 cm positional difference was calculated for each subject.

Second, we calculated the likelihood of voxels to move in the cranial or caudal direction, relative to their average starting position.

Results

The MVHs (Fig. S1) showed that in 9/28 of the cases $\geq 1\%$ of the bowel bag experiences ≥ 2 cm peak-to-peak motion. In 3 of those cases $> 10\%$ of the bowel bag had a peak-to-peak motion of ≥ 2 cm. In 1 case there was even a low percentage (0.2%) of voxels experiencing ≥ 4 cm displacements.

The percentages of the voxels with a specific predominant direction, showed that in most cases (20/28) more than half of the voxels experienced a more cranial motion over the duration of imaging. Furthermore, in the cases where the caudal motion was predominant, the percentage difference was lower.

Conclusions

The study shows that small bowel displacements in the order of 2 cm, for a significant percentage of the bowel, are observed in more than 30% of the cases, introducing the risk of dosimetric relevant impact during a multi-isocenter treatment. Moreover, since the anticipated treatment times for multi-isocenter treatments are longer than the 7.5-15 minutes acquired here, the displacements are expected to become larger⁵.

In most cases, more than half of the bowels experience a more cranial than caudal displacement over time. This information could be used to reduce the risk in multi-isocenter treatments, for example, by irradiating the cranial field first or determining safe overlap lengths based on the penalty maps. Further research is needed to investigate the best approach.

Synthetic 3D MRI generation from CBCT for deep-inspiration breath-hold (DIBH) abdominal treatments

Paulo Quintero, Victoria Yu, Can Wu, Lauren Smith, Ricardo Otazo, Laura Cerviño, Wendy Harris

Memorial Sloan Kettering, New York City, USA

Abstract

Background-Objective: Deep-inspiration breath-hold (DIBH) for abdominal treatments has demonstrated dosimetric and clinical benefits by reducing the dose to organs-at-risk allowing smaller additional margins to the target volume. However, in a conventional LINAC with kV-based imaging, onboard CBCT has limited soft-tissue contrast, making accurate tumor localization for patient setup challenging, especially in the abdomen. To address this issue, a novel method is proposed to synthesize MRI (*synMRI*) from CBCT images using a convolutional neural network (CNN) that predicts the eigenvalues of a prior DIBH motion (from the same patient) modeled by principal component analysis (PCA).

Material/methods: Six simulation MRIs were acquired under similar DIBH conditions with deformable image registration (DIR) performed between a reference DIBH condition (*refMRI*) and each of the five other MRIs. This *refMRI* corresponded to the first DIBH-MRI acquired. A reference synthetic CT (*refsCT*) was generated from the *refMRI* and a 3D CT. PCA is then implemented on the respective deformation vectors. The resulting first three eigenvalues were sampled 1000 times, generating new deformations that were applied to the *refsCT*, creating 1000 DIBH conditions over the CT images. These conditions were used to assemble a dataset (70% for training, 20% for validation, and 10% for testing) to train a CNN model to predict the eigenvalues. Once the CNN model predicted the new eigenvalues for any specific *onboard* condition, these were applied to the deformation vectors to transform the *refMRI* to match the actual anatomic conditions. This method was developed and tested using the digital phantom, XCAT, simulating one reference condition and four different onboard scenarios. Additionally, this method was validated retrospectively with data from four patients. The CNN model performance was evaluated with mean absolute error (MAE) and root mean square error (RMSE). The image quality between the ground truth MRI (*gtMRI*) and the *synMRI* from the testing dataset was evaluated with structure similarity index (SSIM) and normalized RMSE (nRMSE). In the XCAT data, the tumor was contoured in the GT *synMRI* and compared with the contours in the predicted *synMRI* using Volume Dice Coefficient (VDC) and Hausdorff Distance (HD). For the patient data, the liver dome position and internal fiducials were compared between the onboard CBCT and the predicted synthetic MRI using HD and center of mass shift (COMS).

Results: For XCAT, the MAE, RMSE, SSIM, and nRMSE were 0.11 ± 0.02 , 0.11 ± 0.07 , 0.999 ± 0.001 , and 0.10 ± 0.06 , respectively. Across all patients, the MAE, RMSE, SSIM, and nRMSE values were 0.13 ± 0.03 , 0.15 ± 0.03 , 0.997 ± 0.001 , and 0.48 ± 0.04 , respectively. For XCAT, the liver dome differences and target volume COMS between the ground truth *synMRI* (GT-*synMRI*) and predicted *synMRI* (Pred-*synMRI*) were <0.3 mm and < 0.4 mm, respectively. Similarly, for all patient data, the liver dome differences were <1 mm and the fiducials' COMS were < 1.2 mm between the *synMRI* and CBCT.

Conclusion: Results from the digital phantom and patient validation demonstrate the feasibility of the novel method to generate onboard 3D MRI to aid patient positioning and motion monitoring during DIBH treatments on a conventional LINAC.

Toward Personalized Automation in MR-Linac Workflows: Transforming Adaptive Radiotherapy with Advanced Monaco TPS Scripting

Sean Domal¹, Tsuicheng Chiu¹, Justin Visak¹, Jingying Lin¹, Chris Kabat¹, Fan-Chi Su¹, Arnold Pompos¹, Ying Zhang¹, Ruiqi Li¹, Siqui Wang¹, Roberto Pellegrini², Mu-Han Lin¹

¹University of Texas Southwestern Medical Center, Dallas, USA. ²Elekta, Milan, Italy

Abstract

Purpose: The Elekta Unity MR-Linac combines advanced imaging with precise radiotherapy delivery, offering the potential for adaptive treatment planning tailored to individual patients. However, in multi-vendor environments common among MR-guided radiotherapy (MRgRT) users, the planning process can become labor-intensive due to the need to translate data between systems. Furthermore, the diverse range of planning objectives available in the Monaco treatment planning system (TPS) provides flexibility but also heightens the reliance on the planner's expertise to achieve optimal plan quality. These factors can introduce planner variability, impacting workflow efficiency and consistency. To address these challenges, we present an automated planning solution integrating advanced scripting, a streamlined user interface (GUI), and refined constraint-setting rules leveraging novel features in Monaco 6.2.2. We hypothesize that integrating this automated solution will accelerate the planning process, reduce human error, and ensure a more standardized approach to generating high-quality treatment plans.

Methods: The automated workflow introduces a user-friendly GUI that streamlines the customization of dose-volume histogram (DVH) criteria and intensity-modulated radiotherapy (IMRT) constraints. The script reads physician-defined dosimetric goals and simultaneously converts these goals to the dosimetric scorecard in Monaco, applying enhanced rule-based logic to generate corresponding IMRT constraints. This enhancement builds upon existing methods for electron density assignment and structure layering, generating a seamless method to quickly convert an MR simulation volume and dosimetric goals into a "ready-to-optimize" plan. The solution dynamically generates patient-specific planning templates incorporating these parameters, rather than relying on population-based templates. The workflow was evaluated in a clinical MR-Linac environment to assess its impact on usability, efficiency, and consistency.

Results: The automated workflow was evaluated across various treatment sites, including prostate, head and neck, and liver cases. For prostate treatments, plan setup time decreased from 20 to approximately 2 minutes. In complex cases like head and neck, planning time reduced from 45 to about 2 minutes. Automation ensured consistent application of DVH criteria and IMRT constraints, reducing the occurrence of manual errors observed in the manual planning process. Clinical users reported that the streamlined interface enhanced usability, allowing for faster and more accurate customization of planning parameters. Overall, the automated solution significantly improved planning efficiency and consistency, enhancing the quality and reliability of treatment plans using Monaco TPS for MR-Linac therapy.

Conclusions: The automated planning solution presented addresses key challenges in MR-Linac treatment planning using Monaco TPS by integrating advanced scripting, a refined user interface, and robust planning rules. By automating these aspects of the planning process, we minimized the need for repetitive manual inputs and reduced the potential for human error. This solution enhances efficiency, reduces human error, and standardizes plan quality, supporting the broader adoption of automated and adaptive radiotherapy workflows. Future efforts will focus on expanding adaptability by automating self-iterative plan optimization using advanced Monaco 6.2.2 scripting. These advancements have the potential to enable clinicians to deliver consistent, high-quality care with a reduced workload.

Comparative Plan Quality and Dosimetric Analysis of Two Commercially Available MR-Linac Systems in Prostate and Pancreas Cancers

Huiming Dong¹, Jonathan Pham¹, Michael Lauria¹, Brett Sloman², Paul Barry², Jennifer Davis², Daniel Hyer³, Caiden Atienza³, Amar Kishan¹, Ann Raldow¹, X. Sharon Qi¹, Michael Saracen², James Lamb¹

¹University of California, Los Angeles, Los Angeles, USA. ²Elekta, Los Angeles, USA. ³University of Iowa, Iowa City, USA

Abstract

Purpose

The purpose of this study was to perform a planning comparison in prostate and pancreas between the Elekta Unity and ViewRay MRIdian, two commercially available MR-linac systems. Technical differences between the systems include the magnetic field strength, treatment planning system, beam energy and the MLC design, all of which may contribute to different dosimetric characteristics. In addition to the technical differences, the MRIdian system has been employed in two major clinical trials studying hypofractionation with MRgRT: the MIRAGE and SMART trials. It is important to establish whether the Unity system would yield similar plan quality in these two practice-defining trials.

Methods

Twenty clinical plans previously treated on the MRIdian at our institution were randomly selected for replanning on Unity (N=20). Ten were treated for prostatic adenocarcinoma (MIRAGE trial: 8Gy×5=40Gy, N=10) and the other ten were treated for pancreatic adenocarcinoma (SMART trial: 10Gy×5=50Gy, N=10).

Unity plans were generated using the Monaco treatment planning system (Version 5.59.11) following the same site-specific planning guidelines. The same planning MR images, structure set, number of beams, and beam orientations were maintained for both systems. For plan optimization and dose calculation, the maximum number of segments, does calculation grid size were kept the same for both systems. A dose calculation grid of 2mm and 3mm were employed for the prostate and pancreas plans, respectively. To evaluate the plan quality, Unity plans were normalized to the same target coverage as the MRIdian plans.

Finally, plan deliverability was investigated via IMRT QA on a Unity MR-linac system. The criteria of Gamma analysis were dose difference=3%, distance-to-agreement (DTA)=2mm, and a threshold of 10% of the global maximum dose.

Results

Similar dose distributions and dose volume histograms were observed across both systems. For the pancreas plans, there were no significant differences of organ-at-risk doses except for the liver where Unity had lower mean dose (difference=1.40Gy, P=0.0371). For the prostate plans, significantly lower rectum V36Gy (difference=0.52%, P=.0095), V38Gy (difference 0.31%, P=.0043), V40Gy (difference=0.26%, P=.0469) was observed in Unity plans when compared to the MRIdian plans. Additionally, significantly lower left (difference=0.96cc, P=.0137) and right femur V20Gy (difference=1.18cc, P=.0020) was observed in Unity plans compared to the MRIdian plans. Despite the statistical significance, the mean difference between the MRIdian and Unity plans was negligible, and may not be clinically significant.

The mean number of MUs of the prostate plans was 3398 ± 791 and 2478 ± 372 for MRIdian and Unity, respectively. The mean number of MUs of the pancreas plans was 5758 ± 1375 and 4142 ± 1423 for MRIdian and Unity, respectively. The Unity plans used a smaller number of MUs than the MRIdian plans for both prostate (difference=920MUs, P=.0036) and pancreas (difference=1616MUs, P=.0076).

Unity plans were highly deliverable. The mean Gamma passing rate was $96.93 \pm 1.32\%$ and $95.51 \pm 2.25\%$ for the prostate and pancreas plans, respectively.

Conclusion

Similar plan quality was observed between the Elekta Unity and ViewRay MRIdian systems. Unity is capable of delivering plans with equal quality as MRIdian plans delivered in the MIRAGE and SMART clinical trials.

Investigating the dosimetric impact of intrafractional motion in prostate cancer patients during MR-guided adaptive radiotherapy

Shu Xing¹, Nima Hassan Rezaeian¹, Chengcheng Gui¹, Victoria Brennan¹, Ergys Subashi², Neelam Tyagi¹

¹Memorial Sloan Kettering Cancer Center, New York, USA. ²The University of Texas MD Anderson Cancer Center, Houston, USA

Abstract

Purpose: To evaluate the impact of intrafractional motion on the dose distribution and clinical outcome in prostate cancer patients, treated with MR-guided adaptive radiotherapy on a 1.5T MR-linac system.

Methods: Fifty-five prostate cancer patients treated using the adaptive workflow on 1.5 T MR linac were included in this study. All patients received five-fraction stereotactic radiotherapy (SBRT) of 40 Gy to the prostate and a boost of 45 Gy to the dominant intraprostatic lesion. Multiplanar 2D cine MR images were acquired at 1.6 frames/s prior and during treatment. The first 90 frames were used to create a template, to which the subsequent images were registered, generating a motion trace that captured the center of mass shift of the target in the anterior-posterior (AP), superior-inferior (SI) and left-right (LR) directions. The average and maximum shifts along the AP, SI and LR directions were analyzed for all treatment fractions. To assess the dosimetric effect of motion, the daily planned dose distribution was shifted in all three directions based on the recorded motion traces. The cumulative shifted dose distributions were averaged over all frames to produce a motion blurred dose distribution (Figure 1). The difference between the planned and motion blurred dose distributions was calculated. The 3D motion displacement, accounting for motion in all three directions, was analyzed to evaluate its dosimetric impact on prostate CTV, bladder, and urethra dose metrics. In addition, these patients were followed for 24 months post-treatment. Urinary toxicities including urinary frequency, retention, incontinence, and hematuria were evaluated using the Common terminology criteria for adverse events (CTCAE), with Grade > classified as clinically significant. CTCAE grades were collected both within 6 months (acute toxicity) and beyond 6 months (long-term toxicity) post-treatment.

Results: A total of 275 treatment fractions were analyzed in this study. The average prostate motion over all fractions was -0.02 ± 0.21 mm in the LR direction, 0.3 ± 0.5 mm in the AP direction and -0.3 ± 0.6 mm in the SI direction. Maximum prostate motion ranged from -6.0 to 8.6 mm, -12.8 to 5.9 mm and -15.6 to 33.8 mm in the LR, AP and SI directions, respectively (Figure 2). 3D motion displacement less than 1mm was found in 76% of the fractions, which led to less than 6 cGy dose difference between the planned and motion blurred dose for our clinical CTV, bladder, and urethra dose metrics. Larger displacements were associated with increased dose differences for bladder and urethra metrics (Table 1). Among 55 patients, 3 patients experienced > Grade 2 acute toxicities, and 2 patients reported > Grade 2 long term toxicities. All patients with clinically significant toxicities had at least one fraction with an average 3D displacement greater than 1.4mm.

Conclusion: This study investigated the dosimetric impact of intrafractional motion in prostate cancer patients receiving MR-guided adaptive radiotherapy. Our findings suggested insignificant dosimetric impact for 3D displacement less than 1mm. However, larger displacements may result in dose difference and could lead to clinically significant urinary toxicity.



THE 11TH ANNUAL SYMPOSIUM ON MAGNETIC RESONANCE IN RADIATION THERAPY

Posters

Patient-specific deep learning for daily adaptive MRI-guided radiotherapy of rectal cancer

Koen Kuijjer¹, Jeroen de Groot^{1,2}, Martijn Intven¹, Matteo Maspero¹, Mark Savenije¹, Stella Mook¹, Gert Meijer¹

¹University Medical Centre Utrecht, Utrecht, Netherlands. ²Technical University Eindhoven, Eindhoven, Netherlands

Abstract

Purpose:

Manual contour adaptation in daily adaptive radiotherapy is time-consuming, limiting its feasibility for long-course treatments. Automating this process using deep learning (DL) could significantly reduce patient on-table times. Despite the substantial time and expertise in creating pretreatment delineations, this valuable information is typically not utilized in DL models for daily target segmentation. This study investigated integrating patient-specific information into these models and evaluated the impact on segmentation performance.

Materials and Methods:

Three DL strategies for daily mesorectal CTV segmentation were evaluated on 124 MRIs from the daily fractions of 26 rectal cancer patients, each treated with five fractions on a 1.5T MR-linac (Unity, Elekta AB, Sweden). (1) **DL-Base**: a non-patient-specific 3D nnUNet model was trained on 512 pretreatment and online MRIs from 83 patients, using manual mesorectal CTV delineations as ground truth. (2) **DL-Tune**: transfer learning was applied to fine-tune the DL-Base model with the patient's pretreatment MRI and manual delineation. (3) **DL-Scratch**: 3D nnUNet models were trained from scratch, using only the pretreatment MRI and delineation specific to each patient. Adding data from initial fractions to the pretreatment MRI was also evaluated for DL-Tune and DL-Scratch. All methods were compared against deformable image registration (DIR) using MIM version 7.2.8 (MIM Software Inc., Cleveland, Ohio, USA).

Manually adjusted delineations from the clinical workflow were considered as the reference. For each delineation, we calculated the Dice similarity coefficient (DSC), 95th percentile Hausdorff distance (HD95), mean surface distance (MSD), and added path length (APL). Paired t-tests were used to compare all methods, while unpaired t-tests assessed the impact of adding fractions within each method.

Results:

The DL-Tune strategy, incorporating pretreatment patient-specific information, significantly enhanced DL-based segmentations. It achieved a median DSC of 0.94 and HD95 of 3.0 mm, substantially improving over the 0.90 and 9.0 mm for DL-Base ($P<0.001$) (Figure 1). Notably, DL-Tune excelled in defining the

cranio-caudal CTV boundaries compared to DL-Base (Figure 2). Furthermore, DL-Tune outperformed DIR, demonstrating higher DSC (median 0.94 versus 0.92 ($P<0.001$)) and lower APL (median 305 mm vs 549 mm ($P<0.001$)). DL-Tune's performance is able to manage large inter-fraction variations, such as rectal filling, where DIR methods often struggle (Figure 2).

Integrating segmentation data from one fraction modestly improved the DL-Tune models, reducing the median APL from 305 mm to 232 mm ($P=0.009$). DL-Scratch models trained solely on pretreatment data, performed poorly compared to the other methods. However, including data from the first fraction significantly improved performance (median DSC from 0.89 to 0.93 and median MSD from 1.7 mm to 0.93 mm ($P<0.001$)) (Figure 1). Although DL-Tune still outperformed DL-Scratch ($P<0.001$), DL-Scratch shows potential for tumor sites lacking a generic model.

Conclusions

Integrating patient-specific information into DL models significantly improved target segmentation performance, with the best results obtained by fine-tuning a generic model on the patient's pretreatment data. Furthermore, DL-Tune outperformed DIR, the current standard for daily contour generation. Further qualitative and dosimetric analyses are crucial to assess the clinical value of these methods in daily adaptive MRI-guided radiotherapy for rectal cancer.

MRIidian Multiparametric MRI Working Group Assessment of Diffusion-Weighted Imaging Protocols on the 0.35 T MRI-Linear Accelerator

Natalia Lutsik¹, Sungheon Gene Kim², Gage Redler³, Joseph Weygand⁴, Matteo Nardini⁵, Ryan Pennell², Siamak Nejad-Davarani¹, Tess Armstrong⁶, Eric Mellon¹

¹Department of Radiation Oncology, Sylvester Comprehensive Cancer Center, University of Miami Miller School of Medicine, Miami, USA. ²Department of Radiology, Weill Cornell Medical College, New York, USA. ³Department of Radiation Oncology, H. Lee Moffitt Cancer Center and Research Institute, Tampa, USA. ⁴Department of Radiation Oncology and Applied Sciences, Geisel School of Medicine, Dartmouth College, Hanover, USA. ⁵Fondazione Policlinico Universitario Agostino Gemelli IRCCS, Rome, Italy. ⁶Diagnostic Imaging and Interventional Radiology, H. Lee Moffitt Cancer Center and Research Institute, Tampa, USA

Abstract

Purpose: The integration of MRI-Linear Accelerator (MRI-Linac) systems into radiotherapy (RT) presents a unique opportunity to enhance treatment monitoring through functional imaging techniques such as diffusion-weighted imaging (DWI). Although the Quantitative Imaging Biomarkers Alliance (QIBA) recommendations are tailored for high-field MRI systems, this study focuses on validating DWI protocols for the 0.35 T MRI-Linac, optimizing signal-to-noise ratio (SNR), and assessing the consistency of acquisition parameters, image quality, and apparent diffusion coefficient (ADC) values across multiple institutions. The goal is to establish standardized DWI protocols for RT response assessment across the body. In this work we generated and tested consensus protocols for brain, rectum, sarcoma, and prostate.

Methods, Materials: This study included four cancer centers across the USA and Europe, all equipped with 0.35 T MRI-Linac (MRIidian, ViewRay, Mountain View, CA). DWI protocols were developed and optimized for four anatomical regions: brain, rectum, sarcoma, and prostate. The NIST/QIBA Diffusion Phantom (CaliberMRI, Boulder, CO) was scanned with an echo planar imaging DWI sequences at three participating centers in the USA using the designated protocol parameters for each body site (Table 1) at a gantry angle of 0 degrees. Images were acquired with two types of vendor supplied coils: the head-and-neck coil for the brain protocol, and the torso coil for the rectum, sarcoma, and prostate protocols. ADC values were measured in a region of interest in all 13 vials of the phantom, each containing different concentration of polyvinylpyrrolidone (PVP), representing a range of ADC values. ADC values were calculated by fitting the data to a mono-exponential diffusion model using custom Matlab code, and compared with the published references. Temperature correction was applied for eliminating the differences in environmental conditions. SNR was evaluated for each protocol on the DWI images, with SNR defined as the ratio of the signal intensity in the object to the noise signal intensity in the background. The percentage differences of ADC values across all centers were calculated.

Results: For the brain protocol, the ADC differences compared to 3 T reference values at 22 °C ranged from 0.25% to 8%, while inter-center variation was between 0.18% and 14%. In the rectum protocol, ADC discrepancies ranged from 1% to 12% compared to references, and from 0.12% to 18% across

centers. The prostate protocol showed ADC differences of 0.16% to 18% against reference values, and 0.9% to 18% across centers. For the sarcoma protocol, ADC differences ranged from 0.2% to 12% when compared to reference values, and from 0.5% to 18% across centers (Fig. 2). The SNR values for max b-value images were 5 for the brain protocol, 4-5 for rectum, 5-7 for prostate, and 5-10 for sarcoma.

Conclusion: The study demonstrated that ADC differences across centers and 3 T published references did not exceed 20 %, indicating acceptable reproducibility. The SNR for max b-value DWI-images was consistently above 5, representing a good compromise between QIBA recommendations and the capabilities of the 0.35 T MRI-Linac. Optimized protocols allow reliable standardized DWI measurements for RT response assessment across various anatomical regions.

Correcting k-space trajectory errors and slice profile imperfections to improve the accuracy of T_1 and T_2 mapping with MR fingerprinting on a 1.5 T MR-Linac

Magali Nuixe¹, Rosie Goodburn¹, Bastien Lecoeur^{1,2}, Prashant Nair¹, Andreas Wetscherek¹

¹Joint Department of Physics, The Institute of Cancer Research and The Royal Marsden NHS Foundation Trust, Sutton, United Kingdom. ²Department of Computing, Imperial College London, London, United Kingdom

Abstract

Purpose

Hybrid MR-Linac systems enable the integration of quantitative magnetic resonance imaging (qMRI) into the radiotherapy treatment workflow [1]. Daily qMRI could be used to assess treatment response and thus to adapt radiotherapy plans [2]. The purpose of this work is to evaluate k-space trajectory and slice profile corrections for measuring T_1 and T_2 with MR fingerprinting (MRF, [3]) on an MR-Linac.

Materials and Methods

A NIST/ISMRM phantom Model 130, serial number 0064 (CaliberMRI, Inc, Boulder, CO) was scanned four times on a 1.5 T MR-Linac Unity scanner (Elekta AB, Stockholm, Sweden). A 2D gradient-spoiled MRF sequence with an adiabatic inversion pulse, a sinusoidal flip angle scheme with a maximum of 66.9°, and a tiny golden angle radial trajectory was employed [4]. Coil sensitivities were estimated using ESPiRiT [5] included in BART v0.8.00 [6]. K-space trajectory errors were corrected using the first and/or zeroth orders gradient impulse response function (GIRF) [7]. Images were reconstructed using the low-rank inversion method [8] included in BART. The slice profile (SP) was calculated in Julia v1.10.0 [9] using Bloch simulations with 101 isochromats over a distance four times the nominal slice thickness. Two dictionaries, with the same T_1 and T_2 bases and assuming perfect rectangular SP or the calculated SP, were generated using extended phase graphs [10]. Both dictionaries were compressed using randomised singular value decomposition with a power of iteration index q of 2 [11] to achieve an energy ratio of at least 0.999. To evaluate the accuracy of the technique, inversion recovery and multi-echo spin-echo sequences were acquired for gold standard (GS) T_1 and T_2 measurements. Phantom vials with physiologically relevant values (T_1 [150;1500] ms and T_2 [15;260] ms) were delineated using ImageJ (1.54d, NIH, Bethesda, MD, USA), and linear regressions between mean MRF T_1 and T_2 values within each vial and GS measurements were performed for each correction tested.

Results

All linear correlations between T_1 and T_2 MRF and GS values were high ($R^2 > 0.99$, p-value < 0.001). Overall, the mean absolute relative error for T_1 and T_2 decreased with slice profile correction (T_1 : from between 6.3% and 10.2% without it to between 3.9% and 7.7% with it; T_2 : from between 58.2% and 65.0% without it to between 17.4% and 19.9% with it). The correction of radial trajectory errors (GIRF_1st) permitted a better estimation of relaxation times, with a particularly noticeable effect for short T_1 (<412 ms) and T_2 (<30 ms). Correcting for phase errors from B_0 eddy currents (GIRF_1st_0th) did not further improve the results.

Conclusion

This study shows that slice profile correction is essential for accurate T_1 and T_2 mapping using MRF on an MR-Linac, in agreement with previous findings on conventional MR scanner [12]. While SP correction had a significant impact on T_2 estimation, k-space trajectory correction had a greater impact on T_1 estimation. However, some T_2 values within the physiologically relevant range still exhibited high errors despite the corrections.

Real-Time Prediction of Target Displacements Using LightGBM to Mitigate MR-LINAC Latencies

Indu Jyoti Das, Elodie Lugez

Toronto Metropolitan University, Toronto, Canada

Abstract

Purpose: Novel Magnetic Resonance-guided Linear Accelerators (MR-LINACs) enable real-time imaging of patient anatomy during radiation therapy. Cine 2D sagittal and/or coronal images are acquired to monitor any target position deviation. These cine images are compared with a pre-treatment 3D reference image that defines the treatment plan.

MR-LINACs are encumbered by system latencies, notably in image acquisition (~ 200 ms) and image processing (~ 200 ms). This study aims to tackle delays in real-time target tracking by predicting upcoming target displacements. Renowned for its predictive performance -- even with limited data -- and computational efficiency, we propose leveraging LightGBM for accurate target displacement prediction and online training.

Methods: The target's displacement was computed by registering each cine image to the 3D reference image upon availability. The registration was performed using the strategy described by Keiper et al. [1] which leverages the first 30 cine images per acquisition plane as a training set. Building on this strategy, the target's upcoming displacements were predicted. A patient-specific LightGBM model was initially trained using displacement data measured by the image registration on the training set. As new tracking data became available during the treatment delivery, the LightGBM model predicted the next three displacements and was subsequently re-trained with the updated data (Figure 1).

The proposed methods were evaluated using nine datasets curated from public resources, each comprising a 3D reference image, 2D cine images, and ground truth displacement data. These cine datasets featured interleaved sagittal and coronal images; the 3D and 2D images within the same dataset were acquired using different MR pulse sequences and conditions.

Due to the interleaved image acquisition strategy, the methods were evaluated based on their ability to predict the target displacement 400 ms and 600 ms ahead. The prediction accuracy was defined as the average Euclidean distance between the forecasted displacements and their corresponding ground truths. The impact of mitigating system delays was evaluated by measuring the average Euclidean distance between delayed measurements and the ground truth displacements.

Results: Table 1 summarizes the tracking performance. The image registration strategy achieved an average tracking error of 1.19 mm. Most 2D-to-3D image registration errors stemmed from target shape deformations and inconsistencies in imaging acquisition parameters. Simulated system latencies resulted in increased tracking errors of 2.62 mm (400 ms delay) and 3.46 mm (600 ms delay). LightGBM significantly ($p < 0.05$) reduced errors to 1.37 mm and 1.83 mm, respectively, compensating for impacts of system latencies by over 47%.

Conclusions: The proposed methods demonstrated potential for patient-specific real-time tracking of diverse targets with enhanced accuracy. These improvements hold promise for reducing treatment margins, thereby increasing treatment efficacy.

[1] Keiper, T.D., Tai, A., Chen, X., Paulson, E., Lathuilière, F., Bériault, S., Hébert, F., Cooper, D.T., Lachaine, M. and Li, X.A., 2020. Feasibility of real-time motion tracking using cine MRI during MR-guided radiation therapy for abdominal targets. *Medical physics*, 47(8), pp.3554-3566.

Feasibility of reduced contrast dosing for MRI-guided adaptive radiotherapy in glioblastoma

Faisal Mahmood^{1,2}, Uffe Bernchou^{1,2}, Anders Bertelsen¹, Anne Bisgaard¹, Rasmus Lübeck Christiansen¹, Bahar Celik¹, Elisabeth Kildegaard¹, Tine Schytte^{3,2}, Rikke Hedegaard Dahlrot^{3,2}

¹Laboratory of Radiation Physics, Department of Oncology, Odense University Hospital, Odense, Denmark. ²Department of Clinical Research, University of Southern Denmark, Odense, Denmark.

³Department of Oncology, Odense University Hospital, Odense, Denmark

Abstract

Purpose

Glioblastomas are known to evolve during radiotherapy [1,2]. MRI-linac radiotherapy enables daily MRI-guided adaptation, potentially improving treatment of this disease. Standard of care includes gadolinium-based contrast agent (GBCA)-enhanced MRI to delineate glioblastoma boundaries. While studies suggest GBCAs are chemically stable under irradiation [3,4], concerns remain about GBCA retention and potential late adverse effects with repeated use [5]. This study evaluates the feasibility of low-dose GBCA MRI in adaptive radiotherapy for glioblastoma.

Methods

Patients eligible for post-operative radiotherapy were included under the MOMENTUM Study [6] and treated with hypo-fractionation (10 fractions of 3.4 Gy, 5 days per week) on a 1.5 T MRI-linac (Unity, Elekta AB). Daily imaging included a T1W 3D gradient echo scan (TE=3.6 ms, TR=8 ms, FA=8, slice=1.1 mm, in-plane pixel=1.1x1.1 mm², matrix=256x254). GBCA (Gadobutrol, Bayer A/S) was administered every other fraction in either full or half dose (Table 1).

The gross tumour volume (GTV) was adapted by an oncologist at fractions where either full- or half-dose GBCA was administered (fractions 1,3,5,7,9), and the new plan was used as reference for the next fraction without GBCA (fractions 2,4,6,8,10), where the GTV was transferred rigidly without modifications. GTV to clinical target volume was zero, and a planning target volume (PTV) margin of 3 mm was used.

Otsu's method [7] was applied for automatic thresholding within a 2 mm expansion of the GTV, for objective assessment of the enhancing tumour region.

Results

Significant tumour changes were observed in three out of the nine patients included (10-15% GTV increase (n=2), 10-15% GTV decrease (n=1), occurring midway through treatment and stabilizing (example Fig. 1A). Auto-thresholding revealed a less sharply defined enhancing region in half-dose images compared to the full-dose images, resulting in increased volumes (Fig. 2). Volumes reduced when a full-dose threshold was used. Half-dose images provided sufficient contrast for GTV surveillance (Fig. 1A), however in small lesions, half-dose GBCA led to too low contrast enhancement even for

surveillance (Fig. 1B). Images without GBCA enhancement were unsuitable for surveillance/adaptation (Fig. 1A).

Conclusion

The use of GBCA is essential for adaptive MRI-guided radiotherapy of glioblastoma. Half-dose contrast-enhanced MRI may be sufficient for monitoring during radiotherapy, but full-dose imaging is preferable for adaptation. A feasible low-dose workflow may include full-dose MRI at the first fraction and midway through treatment, with optional half-dose MRI at the end. For small lesions, only full-dose images are recommended and should be acquired more frequently.

Exploring respiratory-motion irregularities over 30 minutes and 1 week and enhancing external-to-internal correlation for respiratory-gated radiotherapy

Andrew Milewski^{1,2}, Can Wu², Yilin Liu², Victoria Yu², Jouke Smink³, Ramin Jafari³, Guang Li²

¹Weill Connell Medicine, New York, USA. ²Memorial Sloan Kettering Cancer Center, New York, USA.

³Philips Healthcare, Best, Netherlands

Abstract

Purpose: Dynamic cine magnetic resonance imaging (MRI), including time-resolved (TR) 4DMRI (2Hz), provides unique opportunities to investigate respiratory-motion irregularities over long timeframes relevant to radiotherapy treatments. The MR navigator ascertains the diaphragm's motion, which can be saved concurrently with an external bellows waveform to unveil the external-to-internal motion relationship. Such concurrent motion waveforms provide a unique opportunity to study the statistics of stability, variation, and distribution of patient-specific respiratory-induced organ motions. Using concurrent navigator and bellows waveforms, we will investigate motion variations and evaluate the plausibility of enhancing surrogate-based, respiratory-correlated (RC) motion over the super-long timeframe—spanning from simulation to treatment—needed for respiratory-gated radiotherapy (RGRT) and/or for motion-inclusive radiotherapy based on internal tumor volume (ITV).

Methods: Under an IRB-approved protocol, three volunteers were scanned twice, one week apart, on a 3T Philips MRI scanner. During each imaging session, two sets of concurrent navigator and bellows waveforms intervened by 30 minutes were obtained. A T1-weighted 3D gradient-echo sequence was used with a navigator to monitor diaphragmatic motion in the superior-to-inferior direction at 20Hz for 4–9 minutes depending on the gating efficiency (30–60%). A bellows placed on the upper abdomen recorded external respiratory motion in the anterior-to-posterior direction at 100Hz, which was down-sampled to match the navigator's sampling frequency. The simultaneous waveforms were saved together in a log file. The waveforms' periodicity was evaluated every 30sec using a breathing periodicity index (BPI-5), defined as the energy of the five largest frequency components over the total energy in the signal: BPI-5→1 for highly regular waveforms and BPI-5→0 for highly irregular waveforms. The correlation between the concurrent external and internal waveforms was calculated with and without phase-shift correction. The maximum time-domain cross-correlation method was applied to calculate phase shifts dynamically in 30-second windows. Correlations were analyzed to quantify the enhancement.

Results: The BPI-5 identified fluctuations in breathing periodicity: BPI-5 ranged from 0.48 to 0.90 for the navigator and from 0.48 to 0.95 for the bellows. The average correlation between external and

internal BPI-5 was 0.55 across all scans, ranging from 0.17 to 0.95. Owing mainly to relatively large, but steady phase shifts, the native external-to-internal motion correlation averaged across all scans and subjects was $C=0.75\pm0.09$, significantly enhanced to $C=0.88\pm0.06$ after phase-shift correction. The phase-shift correction consistently improved the correlation without exception. The enhanced external-to-internal correlation reflects greater concordance between the bellows and navigator, suggesting that phase-shift correction renders the bellows a more reliable surrogate for RC-4DMRI or RC-4DCT reconstruction.

Conclusion: Respiratory-motion irregularities—common in 30-sec, 5-min, 30-min, and one-week timescales—affect the correlation between the external bellows and the internal navigator. The enhanced external-to-internal motion correlation indicates that the phase-shift-corrected external surrogate better represents internal motion, suggesting a means to improve the quality of RC-4DMRI or RC-4DCT and the accuracy of respiratory gating in RGRT. When data from more subjects becomes available, further investigations are warranted to evaluate whether deep-learning approaches can address subject-specific or population-based respiratory-motion variations over the protracted timeframe spanning from simulation to treatment.

Exploring imaging biomarkers from tensor-valued diffusion-MRI for predicting treatment response in brain metastases during stereotactic radiotherapy

Minna Lerner^{1,2}, Patrik Brynolfsson^{1,2,3}, Filip Szczepankiewicz⁴, Joakim Medin², Pia C. Sundgren^{5,6}, Lars E. Olsson^{1,2}, Sara Alkner^{2,7}

¹Dept. of Translational Medicine, Division of Medical Radiation Physics, Lund University, Malmö, Sweden.

²Dept. of Hematology, Oncology and Radiation Physics, Skåne University Hospital, Lund, Sweden.

³Hero Imaging AB, SE-90738, Umeå, Sweden. ⁴Dept. of Medical Radiation Physics, Lund University, Lund, Sweden.

⁵Dept. of Diagnostic Radiology, Clinical Sciences Lund, Lund, Sweden.

⁶Lund BioImaging Centre (LBIC), Lund University, Lund, Sweden. ⁷Dept. of Clinical Sciences Lund, Oncology and Pathology, Lund University, Lund, Sweden

Abstract

Purpose

To investigate the feasibility of advanced diffusion MRI parameters as predictive imaging biomarkers for assessing treatment response and tumour radiosensitivity in brain metastases undergoing stereotactic radiotherapy (SRT).

Methods

Patients prescribed SRT (30 Gy/3 fractions) for intracranial metastases underwent four MR-examinations on a 3T MR-scanner: 1-2 weeks prior to SRT, before the last SRT-fraction and post-SRT at 3 and 6 months. The MR-protocol at each session included a tensor-valued diffusion sequence with b-values 100, 700, 1400, 2000 s/mm² acquired for linear and spherical diffusion encodings in several directions and orientations. Diffusion parameter maps were calculated using Q-space trajectory imaging (QTI), estimating mean diffusivity (MD), fractional anisotropy (FA and μ FA) and diffusional variance caused by isotropic (MKI) and anisotropic (MKA) diffusion. Statistical evaluation of the parameter values within the tumour volume were compared before and during SRT and correlated to treatment response based on standard MRI follow-up. Overall survival was analysed using the Kaplan-Meier method.

Results

A total of 26 patients signed informed consent for study participation. Nine patients were excluded due to missing MR-examinations for reasons including technical issues, withdrawal, or death. Four more were excluded due to inadequate signal-to-noise ratio in the MR-images (n=3) or cystic tumour (n=1). QTI analysis was conducted on thirteen patients, comprising six males and seven females. The mean age was 60 years. Primary diagnoses were cancer in the breast (n=4), lung (n=4), colon (n=2), testis (n=1), malignant melanoma (n=1) and unknown primary (n=1). Median volume of the analysed metastases was 5.6 cm³.

Median overall survival in the cohort (n=26) was 12 months. Three months after SRT, a standard MRI follow-up of the analysis cohort (n=13) identified ten responders with tumour volume reductions of at least 30%, and three non-responders. None of the estimated QTI parameters showed statistical significance when comparing mean values for responders and non-responders, or when comparing timepoints before and during SRT within each response group. However, responders demonstrated numerically higher MD and lower values for all other parameters compared to non-responders. The parameter distributions (median \pm mean error) before SRT, pooling all tumour voxels, was statistically significant ($p<0.05$) for MD ($1.017\pm0.007 \mu\text{m}^2/\text{ms}$ vs $0.979\pm0.028 \mu\text{m}^2/\text{ms}$) and FA (0.18 ± 0.002 vs. 0.30 ± 0.012) for responders and non-responders, respectively. Significance remained also during SRT with MD ($1.076\pm0.008 \mu\text{m}^2/\text{ms}$ vs $0.994\pm0.026 \mu\text{m}^2/\text{ms}$) and FA (0.18 ± 0.002 vs. 0.28 ± 0.015), for responders and non-responders, respectively.

Conclusions

The analysis faced significant challenges due to the severity of illness of the patients, leading to extensive exclusions. Consequently, the small sample size prevented general conclusions based on strong statistical evidence. Nevertheless, an explorative approach indicated that it is possible to detect changes in advanced diffusion parameters during SRT of brain metastases. The higher MD in responders is in line with looser tissue in less aggressive tumours, leading to a better treatment response. Increased knowledge on tumour sensitivity to SRT, extracted from MRI images, could help us individualise the patient treatments in the future. Hence, these findings should be further investigated in a larger patient cohort.

Balancing target dose coverage and treatment delivery efficiency during automatic beam gating in MR-guided radioablation of pancreatic tumours

Uffe Bernchou^{1,2}, Rana Bahij³, Tine Schytte^{3,2}, Carsten Brink^{1,2}, Anders Bertelsen¹, Faisal Mahmood^{1,2}

¹Laboratory of Radiation Physics, Department of Oncology, Odense University Hospital, Odense, Denmark. ²Department of Clinical Research, University of Southern Denmark, Odense, Denmark.

³Department of Oncology, Odense University Hospital, Odense, Denmark

Abstract

Purpose

Respiration and drift motion can challenge the target dose coverage during MR-guided radioablation of pancreatic tumours. However, real-time target tracking and beam gating may mitigate such challenges. To manage respiration motion, irradiation can be automatically paused if part of the target moves outside a fixed gating window. For drift motion, baseline shift re-planning adjusts the MLC positions if the target moves outside a chosen drift window [1]. Both methods reduce the treatment delivery efficiency, i.e., the fraction of time the beam is on during a treatment session. This study aims to determine optimal gating and drift window sizes to balance the target dose coverage and treatment delivery efficiency in patients with pancreatic cancer.

Methods

The study included 20 consecutive patients with locally advanced pancreatic cancer, treated in five fractions on a 1.5 T MRI-Linac. 3D target motion data were extracted from the cinematic MR images acquired during treatment using an in-house tracking algorithm. Adaptive treatment plans followed a consensus protocol for treating pancreatic tumours in 5x10 Gy with a 2 mm PTV margin [2]. Treatment sessions were simulated using various gating and drift windows, defined as an isotropic 2 to 5 mm expansion of the GTV (see Figure 1). The delivered dose was accumulated for each simulated session to monitor the target coverage.

Results

The treatment delivery efficiency, number of baseline shift re-plans, and changes in target coverage (GTV D98% and mean dose) were analysed as a function of the gating and drift window size for each of the 100 adaptive fractions (see Figure 2). As expected, the delivery efficiency increased, and target dose coverage decreased with larger gating windows. Reducing the drift window size mitigated the worst target coverage reductions but can lead to excessive usage of baseline shift re-planning. Using 4 mm for both the gating and drift windows provided a compromise, maintaining reasonable target coverage compared to smaller window sizes and achieving over 75% delivery efficiency and a maximum of one baseline shift re-plan in 95% of the fractions.

Conclusion

The target dose coverage can be maintained through beam gating and baseline shift re-planning at the cost of reduced treatment delivery efficiency during radioablation of pancreatic tumours with a 2 mm PTV margin on a 1.5 T MRI-Linac. A good compromise is obtained using 4 mm for both gating and drift window size.

References

- [1] Grimbergen G, et al. Gating and intrafraction drift correction on a 1.5 T MR-Linac: clinical dosimetric benefits for upper abdominal tumors. *Radiother Oncol*. 2023;109932.
- [2] Grimbergen G, et al. Treatment planning for MR-guided SBRT of pancreatic tumors on a 1.5 T MR-Linac: A global consensus protocol. *Clinical and Translational Radiation Oncology*. 2024.

DVH performance evaluation of commercially available synthetic CT for proton therapy of prostate cancer

Emilie Alvarez Andres^{1,2}, Franciska Lebbink^{1,3}, Rudi Apolle³, Aswin L. Hoffmann^{1,2,4}, Esther G. C. Troost^{1,2,3,4}

¹OncoRay – National Center for Radiation Research in Oncology, Faculty of Medicine and University Hospital Carl Gustav Carus, Technische Universität Dresden; Helmholtz-Zentrum Dresden-Rossendorf, Dresden, Germany. ²Department of Radiotherapy and Radiation Oncology, Faculty of Medicine and University Hospital Carl Gustav Carus of Technische Universität Dresden, Dresden, Germany. ³National Center for Tumor Diseases (NCT/UCC), Dresden, Germany: German Cancer Research Center (DKFZ), Heidelberg, Germany; Faculty of Medicine and University Hospital Carl Gustav Carus, Technische Universität Dresden, Dresden, Germany; Helmholtz-Zentrum Dresden-Rossendorf (HZDR), Dresden, Germany. ⁴Institute of Radiooncology – OncoRay, Helmholtz-Zentrum Dresden-Rossendorf, Dresden, Germany

Abstract

Purpose

Magnetic resonance imaging (MRI) has long been the reference anatomical imaging modality for delineation in radiation therapy (RT) of the prostate, and now offers new treatment strategies, such as MR-only RT. For this, MRI-derived synthetic computed tomography (sCT), mandatory for dose calculation, is being explored (1). Currently, commercial solutions are only available for photon-based RT. The goal of this study was to dosimetrically compare three commercial sCT algorithms for proton-based RT (PT) against dual-energy CT based PT.

Material & Methods

Data from ten prostate cancer patients treated with PT between 2020 and 2021 were retrieved. T1-weighted Dixon MRI was processed with two algorithms available for syngo.via (versions VB40 and VB60; Siemens Healthineers, Erlangen, Germany) to generate sCT (respectively termed SV40 and SV60). T2-weighted MRI served as input to MriPlanner v2.2 [(MriP); Spectronic Medical, Helsingborg, Sweden]. SV60 and MriP were both based on deep learning, while SV40 relied on a combination of bulk density assignment and multi-atlas.

The sCT were then deformably registered to the original dual-energy planning CT (pCT). In RayStation 2023B-R (RaySearch Laboratories, Stockholm, Sweden), the initial pencil beam scanning proton plans were transferred to the sCT and doses were re-calculated using two laterally opposed beams [58]

Gy(RBE) to prostate and seminal vesicles followed by 20 Gy(RBE) to the prostate]. To evaluate the sCT, dose volume histogram (DVH) metrics were computed, including D_{mean} , $D_{2\%}$, $D_{98\%}$ for the clinical target volume (CTV) and V_{50Gy} , V_{65Gy} and V_{70Gy} for organs-at-risk (OARs). These metrics were compared between the pCT and the three investigated algorithms. Wilcoxon tests were performed, and a significance threshold of 0.008 was selected, including a Bonferroni correction.

Results

For the CTV, the D_{mean} significantly differed between pCT and SV40 (77.11 ± 0.06 Gy versus 76.83 ± 0.11 Gy, respectively; $p=0.002$; Table 1). Moreover, the average relative CTV $D_{2\%}$ differences between pCT and SV40, SV60 and MriP, respectively, were 0.16%, 0.05% and -0.15%, with the last difference being statistically significantly different from the others ($p \leq 0.004$). Similarly, the mean relative differences for the CTV $D_{98\%}$ were 0.30%, 0.05% and 0.03%, with the first and last performances statistically significant ($p=0.004$).

For the OARs, only statistically significant differences were found for V_{70Gy} of the rectum between pCT ($10.61 \pm 1.68\%$) and SV60 ($10.70 \pm 1.66\%$; $p=0.002$), and for the femoral heads $D_{2\%}$ (33.18 ± 0.90 Gy, 33.09 ± 0.88 Gy and 33.04 ± 0.89 Gy for the pCT, SV60 and MriP, respectively; $p \leq 0.002$). All other DVH metrics of the investigated algorithms were not found to significantly differ from the pCT (Table 1 and Figures).

Conclusion

The investigated algorithms were proven to be equivalent for PT, with a slight advantage for MriP. This finding should be consolidated with the computation of additional metrics, such as local gamma indices and range differences, before a potential use in PT.

Reference

1. Villegas F, Dal Bello R, Alvarez-Andres E, u. a. Challenges and opportunities in the development and clinical implementation of artificial intelligence based synthetic computed tomography for magnetic resonance only radiotherapy. Radiother Oncol. 1. September 2024;198:110387.

Repeatability of apparent diffusion coefficient (ADC) and feasibility of diffusion-weighted prostate imaging at a 0.35T MRIdian MR-Linac.

Evangelia Kaza¹, Kaitlyn Raiber², Jonathan Leeman¹

¹Department of Radiation Oncology, Dana Farber/Brigham and Women's Hospital, Harvard Medical School, Boston, USA. ²Johns Hopkins University, Baltimore, USA

Abstract

Purpose: Prostate cancer is the second most common and fifth most deadly cancer in men worldwide. Image-guided adaptive radiotherapy is a state-of-the-art treatment of prostate cancer, allowing for daily treatment adaption. Apparent diffusion coefficient (ADC) from diffusion-weighted imaging (DWI) represents a promising biomarker of cancer response to radiotherapy, which may inform treatment planning. However, DWI has not yet been implemented for more challenging body sites outside the brain on ViewRay MR-Linacs. We aimed to assess ADC repeatability and to optimize DWI for prostate imaging on a 0.35T MRIdian MR-Linac.

Methods: A QAlibreMD Diffusion phantom was imaged in the MRIdian brain coil with two axial DWI sequences (S1, S2) at 0 and 20 °C temperature and 0° gantry angle. The b-values and slice thickness of S1 and S2 matched the prostate DW-MR simulations in the department and the manufacturer recommended sample protocol, respectively, while the rest parameters were adjusted for the lower B_0 field (table 1). Phantom scans for each temperature were repeated in 1 or 2 months. The mean and standard deviation of each phantom tube were extracted from the scanner produced ADC maps. ADC repeatability between repeated acquisitions of the same sequence at the same temperature was calculated as the absolute difference of the mean ADCs of each scan relative to their average value. Subsequently, a consented healthy male volunteer was imaged with a torso coil surrounding his pelvis. The sequences S1 and S2 were modified and resulting images were compared for SNR, artifacts, prostate conspicuity, and acquisition time.

Results: Phantom temperature varied less than 1 °C between repeated scans. S1 ($b= 100, 800 \text{ s/mm}^2$) demonstrated mean ADC repeatability of 8.0% and 6.6% at 0 and 20 °C, respectively. For S2 ($b= 0, 500, 900, 2000 \text{ s/mm}^2$), mean ADC repeatability was 7.2% and 6.8% at these temperatures (Figure 1). Notably, the 0.35T ADC values obtained by both sequences were close to the manufacturer provided reference ADC values for the tubes at 3T, except for the water filled tubes at room temperature.

Among the two DWI sequences, a version of S1 with voxel size 1.5x1.5x2 mm³ (S3, table 1) was selected as providing the optimal combination of sufficient image quality and spatial resolution as well as short acquisition time (3min 45s) for volunteer imaging. The prostate was discerned well from surrounding tissues on the obtained trace-weighted images and ADC maps (Figure 2).

Conclusions: Overall, the phantom DWI scans showed good ADC repeatability with an average < 10% within a couple months' time. The demonstrated feasibility to acquire prostate DW images and ADC maps with sufficient spatial resolution in a clinically acceptable time will enable the future implementation of the optimized DWI sequence for prostate cancer patients at the 0.35T MR-Linac. Moreover, employing the same b-values as for prostate 3T MR simulations will allow for more direct comparisons between ADC maps from the two different scanners.

Quantitative MRI Biomarker Development for Personalised and Adaptive Stereotactic Body Radiation Therapy (SBRT) of Hepatocellular Carcinoma

Sirisha Tadimalla^{1,2}, Tim Wang², Fidel Navarro¹, Robbie Barnett³, David Farlow³, Sheryl Foster^{4,5}, Val Gebski⁶, Jonathan Sykes², Jacob George⁷, Verity Ahern², Steven Sourbron⁸, Annette Haworth^{1,2}

¹Institute of Medical Physics, The University of Sydney, Sydney, Australia. ²Sydney West Radiation Oncology Network, Westmead Hospital, Westmead, Australia. ³Department of Nuclear Medicine, PET and Ultrasound, Westmead Hospital, Westmead, Australia. ⁴Department of Radiology, Westmead Hospital, Westmead, Australia. ⁵Sydney School of Health Sciences, Faculty of Medicine and Health, The University of Sydney, Sydney, Australia. ⁶NHMRC Clinical Trials Centre, The University of Sydney, Sydney, Australia. ⁷Department of Gastroenterology and Hepatology, Westmead Hospital, Westmead, Australia. ⁸Division of Clinical Medicine, University of Sheffield, Sheffield, United Kingdom

Abstract

Purpose: Stereotactic body radiation therapy (SBRT) is an emerging treatment option for patients with hepatocellular carcinoma (HCC). The risk of radiation induced liver damage (RILD) remains high for patients with underlying cirrhosis.¹ The Personalised liver SBRT using magnetic resonance imaging (**PRISM**) clinical trial is investigating the use of MRI to personalise SBRT plans to minimise dose to high-functioning liver tissue while targeting tumours more effectively. The study aims to develop a quantitative MRI biomarker of liver function and establish a radiation dose-function relationship for personalised SBRT treatment planning and adaptation.

Quantitative DCE-MRI parameters have been used previously to demonstrate feasibility of functional sparing of liver tissue during SBRT.² However, many patients are also likely to have elevated fat in the liver tissue which will confound the T1 measurements used in DCE-MRI pharmacokinetic modelling. Furthermore, radiation-induced changes in liver fat content can complicate response assessment during and after SBRT. Here, we present a novel, in-scan quality assurance approach to identify fat-induced bias in liver T1 measurements in the PRISM clinical trial.

Methods:

A multi-parametric MRI protocol was developed on a 3.0 T MAGNETOM Prisma MRI scanner (Siemens Healthineers, Erlangen, Germany). The protocol included 3D multi-echo GRE for proton density fat fraction (PDFF) mapping; 3D SPGR T1 mapping with variable flip angles (6.5°, 15°, 27°) and fat-sat; B1 mapping for field inhomogeneity correction. Three healthy volunteers were scanned and PDFF and B1 corrected T1 maps were calculated. An in-scan fat-water phantom (Calimetryx, USA) containing 5 gel-filled vials with known fat concentrations (between 0% and 40%), was placed under the volunteer on the

scanner table and included in the imaging field of view during each scan. Mean PDFF and T1 values were extracted from each of the vials as well as the liver.

Results:

PDFF values in the vials were comparable to those reported by the manufacturer, with the largest absolute error seen in the vial with the highest fat concentration (-4.9%). No fat-water swaps were observed in any of the PDFF maps. A nonlinear relationship between the T1 and PDFF values was observed, with T1 underestimated by up to 27% at PDFF ~ 9% and then overestimated at higher PDFF. Liver PDFF measurements in the volunteers were < 5%, as expected for healthy liver. In this range, however, no correlation was observed between T1 and PDFF values in the liver.

Discussion and conclusion:

Presence of fat impacts liver T1 values and can subsequently influence changes in liver DCE-MRI parameters during and after liver SBRT. Preliminary results demonstrate feasibility of using an in-scan phantom to identify T1 bias due to fat. As the PRISM study progresses, data collected in patients with elevated PDFF will enable development of an empirical model for fat correction of liver T1 measurements. The novel in-scan quality assurance approach in the PRISM clinical trial will enable robust evaluation of quantitative MRI biomarkers of liver function radiation response during and after SBRT for patients with HCC.

References:

1. Apisarnthanarax et al, *10.1016/j.prro.2021.09.004*
2. Wei et al, *10.1016/j.ijrobp.2022.09.077*

Evaluating Geometric Distortion Correction Effects on ADC in Head and Neck Diffusion MRI: Applications in Radiotherapy

Minoo Gandomi^{1,2}, Minna Lerner^{1,2}, Lars E. Olsson^{1,2}, Maria Gebre-Medhin¹, Patrik Brynolfsson^{1,2}

¹Department of Haematology, Oncology, and Radiation Physics, Skåne University Hospital, Lund, Sweden. ²Department of Translational Medicine, Division of Medical Radiation Physics, Lund University, Malmö, Sweden

Abstract

Introduction and Purpose: Imaging biomarkers using diffusion MRI (dMRI) and its property to reflect tumour properties are promising for individualised radiotherapy. However, head and neck (H&N) tumours are challenging to image accurately due to geometric distortions caused by air-tissue susceptibility differences in the aerodigestive tract. Single-shot echo-planar-imaging (ssEPI), commonly used in dMRI is particularly prone to distortions. One way to reduce these artefacts include off-resonance distortion corrections. The aim of this study was to evaluate off-resonance distortion correction for two EPI sequences—ssEPI and multiplexed sensitivity encoding (MUSE)—using delineated structures and deformation transforms.

Method: MRI was performed on a GE Signa 3T scanner with the patient in radiotherapy fixation mask. The evaluation was performed on one patient with a squamous cell carcinoma stage T4N1 in the tonsil (ARTSCAN VI, NCT06248996). Diffusion images were acquired with $2 \times 2 \times 4 \text{ mm}^3$ voxels, $220 \times 220 \text{ mm}^2$ field of view, and with phase-encoding directions AP, PA for ssEPI, and AP, PA, RL, LR for MUSE. A T2w image was acquired for anatomical reference. The gross tumour volume (GTV) was 48.7 cc delineated on PET/CT images, according to clinical routine. Distortion correction was performed on diffusion images using TOPUP (FMRIB Software Library), generating a deformation field transform which was applied to the GTV. ADC maps were generated using $b = (0, 800) \text{ s/mm}^2$. To evaluate distortion correction efficacy, original structures were applied on corrected images, while deformed structures were applied on distorted images. The Dice coefficient between distorted and original structures was calculated. The difference in ADC between the deformed GTV in the distorted images and the GTV in the corrected images was calculated.

Results: The visible tumour in the distortion corrected MUSE images agree better with the GTV, encapsulating the tumour with minimal normal tissue at the edges, compared to ssEPI. The GTV was deformed to a larger extent for the ssEPI. The Dice coefficient shows better agreement between original structures and those deformed by the MUSE TOPUP-field compared to ssEPI (0.89 and 0.81 respectively). Further, the alignment is visually better between deformed structure and tumour in the distorted MUSE images. Conversely, the tumour extends beyond the GTV boundary in several ssEPI image slices, both corrected and distorted. The imperfect corrections are reflected in ADC values. Mean and median ADC discrepancies between corrected and distorted images lie within 10% for MUSE and ssEPI AP images, but around 25% for ssEPI PA.

Conclusion: MUSE images demonstrate less distortion and greater geometric accuracy compared to ssEPI, making MUSE a more suitable sequence for H&N diffusion imaging in radiotherapy. The results show that MUSE images are also better corrected, likely due to higher phase-encoding bandwidth causing less distortions. Effective distortion correction is necessary to unlock the potential of these imaging techniques, particularly for developing imaging biomarkers to improve radiotherapy outcomes. While MUSE shows promising results, further investigation on additional patients is needed to fully understand the impact of correction on ADC consistency and the clinical relevance of these findings.

Deep-learning based intravoxel incoherent motion magnetic resonance imaging with fewer b-values: simulation and evaluation in head and neck cancer

Marte Kåstad Høiskar, Amalie Toftum Hop, René M. Winter, Kathrine Røe Redalen

Norwegian University of Science and Technology, Trondheim, Norway

Abstract

Purpose

There is a growing interest in the use of quantitative biomarkers from diffusion-weighted magnetic resonance imaging (DW-MRI) for radiotherapy purposes. Intravoxel incoherent motion (IVIM) modelling of DW-MRI can quantify tissue perfusion and diffusion. The model is described by three parameters pure tissue diffusion coefficient D_t , perfusion fraction f_p , and pseudo-diffusion coefficient D_p , which are promising biomarkers for radiotherapy. In conventional IVIM modelling, the accuracy of parameters increases with the number of b-values used during acquisition of DW-MRI. Due to the limitations in clinical scan time, few b-values are often used, resulting in poor parameter accuracy. Deep neural networks (DNNs), with their unique ability to discover complicated patterns, have the potential to improve the precision in IVIM parameter calculation. Our aim was to investigate whether deep-learning IVIM algorithms could produce more accurate parameters using fewer b-values for head and neck cancer (HNC) than conventional algorithms.

Methods

Two DNNs, one supervised (DNN_{SL}) and one self-supervised (DNN_{SSL}), were evaluated in silico before they were evaluated for HNC patients. They were compared to two conventional algorithms: least square fitting (LSQ) and segmented fitting (SEG) algorithms.

Synthetic DW-MRI signals were generated using 4, 5, and 11 b-values by inserting pseudorandom IVIM parameters into the IVIM model. Rician noise was added to the synthetic signal, resulting in synthetic data sets with signal-to-noise ratio (SNR) between 8 and 100. For all synthetic data sets, IVIM parameters were estimated with all four algorithms. The accuracy of all algorithms was evaluated by calculating the normalized mean absolute error (NMAE) between the estimated and ground truth parameter values.

For 11 HNC patients, DW-MRI was acquired with 11 b-values before radiotherapy. IVIM parameters were predicted by all four algorithms using 4, 5 and 11 b-values, where the data set with 11 b-values will function as a reference. The analysis of the 11 b-value data set is still ongoing.

Results

For simulations with 11 b-values and SNR of 20, similar to the SNR in patient data, the DNN_{SL} and DNN_{SSL} calculated more accurate IVIM parameters (lower NMAE) compared to LSQ and SEG (NMAE(D_t) = 0.12/0.14 vs 0.19/0.20; NMAE(f_p) = 0.17/0.19 vs 0.29/0.24; NMAE(D_p) = 0.30/0.36 vs 0.66/0.67) (Figure 1). DNN_{SL} and DNN_{SSL}, in contrast to LSQ and SEG, maintained accurate parameter estimation when reducing to 4 or 5 b-values (NMAE(D_t) < 0.18/0.15 vs 0.27/0.21; NMAE(f_p) < 0.24/0.20 vs 0.48/0.28; NMAE(D_p) < 0.49/0.40 vs 2.01/1.97). Although DNN_{SL} was somewhat more accurate than DNN_{SSL} for SNR of 20, it overestimated low parameter values and underestimated high parameter values. This trend was enhanced when reducing the number of b-values (Figure 2). Preliminary results from patient data showed that parameter maps estimated by DNNs stayed more consistent, compared to conventional models, when reducing number of b-values.

Conclusions

The simulations suggest that DNNs can achieve similar accuracy with fewer b-values than conventional algorithms achieve with 11 b-values for all parameters. IVIM analysis with fewer b-values using DNNs seems promising for HNC patients, but validation with analysis of clinical data with 11 b-values is warranted.

Implementation of T2 –weighted Turbo Spin Echo MR-sequences as new pelvic protocol for Comprehensive Motion Management with 1.5T MR-linac

Michele Rigo, Chiara De-Colle, Luca Nicosia, Niccolò Giaj-Levra, Edoardo Pastorello, Francesco Ricchetti, Carolina Orsatti, Andrea Romei, Nicola Bianchi, Riccardo Filippo Borgese, Antonio De Simone, Davide Gurrera, Stefania Naccarato, Gianluisa Sicignano, Ruggero Ruggieri, Filippo Alongi

Advanced Radiation Oncology Department, Negrar di Valpolicella, Italy

Abstract

Purpose/Objective

1.5T MR-Linac represents a breakthrough innovation in radiotherapy and one of its major features compared to conventional linacs is the possibility to define the target and surrounding organs-at-risk with high precision due to MR imaging. Continuous studies are ongoing in order to further improve the MR sequences.

Recently Elekta released the new Unity MR R5.8.1 Service Pack software introducing new software functionalities and protocol changes such as new pelvic MR-sequences.

These new sequences, and mainly T2 –weighted Turbo Spin Echo, seem guarantee better pelvic soft tissues resolution and a great improvement in target visualisation, that is crucial to evaluate its right position during template acquisition in Comprehensive Motion Management workflow. Moreover, the intrafraction target tracking and gating during treatment delivery depends on the correct evaluation of the target position in this phase.

Herein we report our first experience in the daily adapted MR-guided prostate treatment based on the new T2 –weighted Turbo Spin Echo scans.

Materials/Methods

In May 2024 MR R5.8.1 was installed by Philips on Marlin CMM was installed at our Institution and used for all PC patients treated on the MR-linac.

Herein we report our experience on the new pelvic protocols used for the first 15 treatment sessions of prostate cancer patients treated on 1.5T MR-Linac with daily-adapted RT and target tracking by means CMM.

Results

Between May 2024 and March 2024, 2 PC patients were treated using the new MR pelvic protocol that replaces the previous balanced Turbo Field Echo sequence used for template acquisition and for motion monitoring during treatment delivery. The selected sequences were T2 –weighted Turbo Spin Echo with a refresh rate of 0.5 frame per second for 1 patient treated in 5 fractions and T2 –weighted Turbo Spin Echo with a refresh rate of 1 frame per second for the first 10 fractions of the other patient.

The acquisition of T2 TSE sequence lasts about 2 minutes more compared to the previous one, but the new scan offers an unprecedent resolution of the pelvic anatomy with higher definition of the intraprostatic tissues and organ bounderies, reducing also the artifact at the crossing of sagittal and coronal planes on the target and air bubble artifacts into the rectum. Moreover, patients report less sequence noise compared to the previuos resulting so in a better patient tolerability during treatment delivery.

All patients completed the planned treatment sessions without technical issues.

No overall treatment duration lengthening was reported.

Conclusion

This is the first report of a clinical application of T2 –weighted Turbo Spin Echo in the CMM workflow in a series of 15 treatment sessions of prostate cancer patients treated on 1.5T MR-Linac with daily-adapted RT. In our opinion the implementation of the new pelvic protocol represents an essential step towards empowering the potential of MR-guided RT.

In conclusion, the new pelvic protocol was efficaciously implemented in our daily clinical routine. Treatment duration doesn't change and the patients report optimal tolerability.

MRI-guided stereotactic radiotherapy for multiple kidney tumors within a solitary kidney

Claire van Vliet, Joyce Caro, Omar Bohoudi, Miguel Palacios, Ben Slotman, Anna Bruynzeel

Amsterdam UMC, Amsterdam, Netherlands

Abstract

Purpose

For patients with multiple tumors in a solitary kidney standard treatment consisting of (partial) nephrectomy is not feasible. Stereotactic ablative body radiotherapy (SABR) is an emerging alternative treatment option. The delivery of SABR using Stereotactic MRI-guided adaptive radiotherapy (SMART) enables daily plan adaptation, gated treatment and therefore small safety margins. We report on the use of SMART for multiple tumors in a solitary kidney.

Methods

Patients with a solitary kidney and multiple renal tumors treated with SMART were included. Multiple lesions were treated in separate or combined target structures depending on location. A PTV margin of 3 mm was used and daily online plan adaptation and gated delivery were regularly performed at all fractions. Fractionation schedule was based on tumor size and location. Dose constraints for the ipsilateral kidney were Dmean of 9 Gy and V15 of 33%, maximum nephron-sparing was attempted because of the solitary kidney. Follow up was according to local guidelines and carried out by the urologist. Recurrences outside the radiation field were scored as new lesions and separate treatments when referred for SABR again.

Results

Between 2021-2024, 10 treatments in 7 solitary kidney patients were analyzed.

Median age was 68 years (55-86). Most patients were male (85.7%) and all patients had a solitary kidney because of earlier radical nephrectomy for RCC. Median tumor size was 2.9 cm (1.2-4.7), and most tumors were treated with 5 fractions of 8 Gy or a single fraction of 26 Gy.

Six patients were treated for multiple tumors simultaneously; three of these had one GTV structure of 2-3 combined lesions, resulting in GTV volumes of 6.5-26.6 cc. Dmean kidney was 8.18 Gy (6.5-9.93) and V15 was 20.3% (16.5-24). Three other patients were treated on 2 separate GTV's of 1.7-12.2 cc, resulting in mean kidney doses of 9.25 Gy (8.15-10.7) and V15 of 23.1% (19.6-28.7).

Of the latter, two patients developed a new tumor lesion outside the radiation field and were treated again on GTV's of 3.9 and 7.3 cc, combined mean kidney doses of 12.04 and 12.15 and combined V15 of 25.1% and 29.4% were achieved.

The seventh patient was treated on two lesions of 1.5 and 4.2 cc on two separate occasions which resulted in a combined Dmean kidney of 8.3 Gy and V15 of 11.6%.

All treatments were completed as scheduled, and only grade 1 fatigue and nausea occurred in three patients.

Mean baseline eGFR was 48.1 ml/min (\pm 13.8). Mean change in eGFR after SMART was -4.6 ml/min (\pm 3.9) and none of the patients required dialysis.

After a median follow up of 21.4 months (4.7–39.2), local control of treated lesions and overall survival was 100%.

Conclusions

In patients with a solitary kidney, the use of SMART enables treatment of multiple tumors simultaneously and in subsequent sessions without significant decrease in renal function.

Daily adapted prostate re-SBRT with significantly PTV margin reduction and intrafraction drift checking and compensation by means of Comprehensive Motion Management

Michele Rigo, Chiara De-Colle, Luca Nicosia, Niccolò Giaj-Levra, Francesco Ricchetti, Edoardo Pastorello, Andrea Gaetano Allegra, Carolina Orsatti, Andrea Romei, Nicola Bianchi, Riccardo Filippo Borgese, Antonio De Simone, Davide Gurrera, Stefania Naccarato, Gianluisa Sicignano, Ruggero Ruggieri, Filippo Alongi

Advanced radiation Oncology Department, Negrar di Valpolicella, Italy

Abstract

Purpose/Objective

Almost one third of the patients undergo biochemical or macroscopical relapse after primary treatment, of which 30–47% were previously subjected to RT.

The optimal therapeutic approach for local relapses of previously irradiated prostate cancer (PC) is not still standardized. Whole gland re-SBRT could represent a treatment option in highly selected patients.

The critical issue in re-SBRT is the tolerability of organs-at-risk (OARs) that could lead to severe radiation-induced complications. However, the implementation of modern MR-linac technology is showing promising results in terms of treatment accuracy.

Continuous monitoring of the target during treatment delivery, automatic gating when the target moves outside of the beam and plan adjustments by means Comprehensive Motion Management (CMM) allow high treatment precision and lower side effects.

Materials and Methods

In September 2023 CMM was installed at our Institution and used for all prostate re-SBRT on the MR-linac. Patients included in this report had the following characteristics: 1) age >18 years; 2) radiological diagnosis of recurrent PC by means of MRI and Choline- or PSMA-PET/CT due to a rising PSA value; 3) previous RT treatment to prostate. Exclusion criteria were clinical contraindications to MRI or IPSS >15.

We report the treatments of the first eight patients who met the inclusion criteria. The SBRT schedules consisted 30 Gy in 5 fractions for 4 patients and 32.5 Gy in 5 fractions for 4 patients, respectively. A PTV margin of 1 mm was applied in all cases. Adapt-to-shape (ATS) or adapt-to-position (ATP) workflows were chosen based on daily anatomy. The SBRT could have been delivered every day or every other day.

We reported patients and treatment characteristics, beam-on time, beam-hold time due to gating, duty cycle (% of the total beam-on time of the entire delivery phase), positioning shifts.

Results

Between November 2023 and August 2024, 8 patients with intraprostatic cancer recurrence were treated with prostate re-SBRT using daily CMM. Five (63%) out of 8 patients were treated with 5-fraction SBRT every day and three (37%) every other day. ATS workflow was applied for 17 fractions and ATP for 23 sessions. The target was represented by the whole prostate gland.

All patients completed the planned treatment. The mean duty cycle for the 40 treatment fractions was 96.88% (95%CI 94.7-98.3%). The mean beam-on time was 469 seconds (95%CI 432.5-536 seconds).

Globally, beam-hold occurred in all treatment fractions for a mean beam-hold count of 27.4 instances (95%CI 22-33). The mean beam-hold time of those treatment fractions was 115 seconds (95%CI 79-147). No baseline shift plan was performed.

Acute toxicity assessed by CTCAEv5.0 was: 3 case of grade 1 cystitis, 2 case of grade 2 cystitis, 1 case of hematuria. No G \geq 3 toxicity occurred.

Conclusion

This is the first report of a clinical application of CMM for prostate re-SBRT. The CMM implementation is crucial to safely reduce GTV-PTV due to target tracking, gating and intrafraction shifts compensations by performing baseline shift plans with minimal treatment elongation. The procedure was well tolerated by patients and the acute toxicity rates were mild.

Initial clinical experience of stereotactic body radiotherapy (SBRT) for liver metastases with target intrafraction tracking and gating by means Comprehensive Motion Management with 1.5T MR-Linac

Michele Rigo, Chiara De-Colle, Luca Nicosia, Niccolò Giaj-Levra, Francesco Ricchetti, Edoardo Pastorello, Andrea Gaetano Allegra, Carolina Orsatti, Andrea Romei, Nicola Bianchi, Riccardo Filippo Borgese, Antonio De Simone, Davide Gurrera, Stefania Naccarato, Gianluisa Sicignano, Ruggero Ruggieri, Filippo Alongi

Advanced Radiation Oncology Department, Negrar di Valpolicella, Italy

Abstract

Purpose/Objective

SBRT is well known treatment option for the management of non-resectable liver oligometastases.

The 1.5T MR-Linac permit to improve the target delineation accuracy due to high soft tissue image quality compared to CT, better sparing the surrounding organs-at-risk. Dose escalation appears directly related to improvement of local control and clinical outcomes. The clinical introduction of CMM on 1.5T MR-Linac may ensure higher safety and efficacy. Moreover, it allows for treatment of lesions close to critical structures that cannot be treated by means radiofrequency ablation or other liver-directed treatments.

Materials/Methods

In September 2023 CMM was installed at our Institution and used for all liver SBRT on the MR-linac. Patients included in this report had the following characteristics: 1) age >18 years; 2) radiological diagnosis of liver metastases. Exclusion criteria were clinical contraindications to MRI.

We report the treatments of the first fifteen patients who met the inclusion criteria. The SBRT schedules ranges from 3 to 10 fractions with a total dose that ranges from 40 to 60 Gy using 5 mm PTV expansion in all directions. The SBRT was delivered every day. Adapt-to-shape (ATS) or adapt-to-position (ATP) workflows were chosen based on daily anatomy. We analyzed patients and treatment characteristics, beam-on time, beam-hold time due to gating, duty cycle (% of the total beam-on time of the entire delivery phase), positioning shifts.

Results

Between September 2023 and November 2024, 15 patients with a total of 18 liver metastases were treated on 1.5T MR-linac using daily CMM.

ATS workflow was applied for 23 fractions and ATP for 63 sessions. The treatments were delivered in free-breathing.

All patients completed the planned treatment. The mean duty cycle for the 86 treatment fractions was 91.92% (95%CI 87.86-94.95%). The mean beam-on time was 759 seconds (12 minutes and 39 seconds; 95%CI 682.8-885.5 seconds).

Globally, beam-hold occurred in all treatment fractions for a mean beam-hold count of 57.4 instances (95%CI 49.2-107.3). The mean beam-hold time of those treatment fractions was 257 seconds (95%CI 178-301). No baseline shift plan was performed due to persistent target drifts.

At the last treatment session, treatment-related toxicity (acc. CTCAE v5.0) was: 8 cases of grade 1 nausea and 5 case of grade 1 abdominal pain. No grade 2 or higher toxicity occurred.

Conclusion

This is the first report of a clinical application of CMM in a series 18 liver metastases treated with SBRT on 1.5T MR-linac. The implementation of CMM led to reduced treatment margins, decreasing the amount of healthy tissue within the high dose region. In combination with online motion management it also allows for high precision treatment delivery with real-time target tracking and gating when intrafraction motion occurs. CMM can guarantee high treatment precision without significant beam-on time increase.

In conclusion, CMM was efficaciously implemented in our daily clinical routine also in liver SBRT. Treatment duration was minimally increased and the procedure was well tolerated by patients. Moreover, the acute toxicity rates were mild.

Daily adapted pancreas SBRT with target intrafraction tracking and gating by means Comprehensive Motion Management with 1.5T MR-Linac

Michele Rigo, Chiara De-Colle, Luca Nicosia, Niccolò Gaj-Levra, Francesco Ricchetti, Andrea Gaetano Allegra, Edoardo Pastorello, Carolina Orsatti, Andrea Romei, Nicola Bianchi, Riccardo Filippo Borgese, Antonio De Simone, Davide Gurrera, Stefania Naccarato, Gianluisa Sicignano, Ruggero Ruggieri, Filippo Alongi

Advanced Radiation Oncology Department, Negrar di Valpolicella, Italy

Abstract

Purpose/Objective

MR-guided stereotactic body radiotherapy (SBRT) provide the much needed breakthrough treatment option for patients with pancreatic cancer, where other radiotherapy treatment modalities often lack efficacy due to dose-limiting normal tissue toxicity, poor soft tissue contrast and weak capability to account for internal target motion without invasive surrogates.

The clinical introduction of CMM on 1.5T MR-Linac allows for target intrafraction tracking and gating, increasing the sparing of normal tissue without placement of fiducials and spacers, ensuring the delivery of highly focused radiation to the tumor while further limiting the dose to adjacent organs at risk. This feature gives also the opportunity to escalate the dose of radiotherapy improving local control.

Materials/Methods

In September 2023 CMM was installed at our Institution and used for all pancreas SBRT on the MR-linac. Patients included in this report had the following characteristics: 1) age >18 years; 2) diagnosis of pancreas carcinoma. Exclusion criteria were clinical contraindications to MRI.

We report the treatments of the first fifteen patients who met the inclusion criteria. The SBRT schedules ranges from 5 to 10 fractions with a total dose that ranges from 45 to 60 Gy. The SBRT was delivered every day and adapt-to-shape (ATS) workflow was adopted for all treatment sessions. The following variables were reported: patients and treatment characteristics, beam-on time, beam-hold time due to gating, duty cycle (% of the total beam-on time of the entire delivery phase), positioning shifts.

Results

Between February and November 2024, 15 patients with pancreas cancer were treated with SBRT at our Institution on 1.5T MR-linac using daily CMM. The median age was 69 years (range 55-79). In all cases

we chose as online motion management the gating envelope selecting GTV as “Anatomic Position Monitoring” (APM) target structure and PTV as “Gating Envelope” and we set the VOICE threshold at 95%.

The PTV margin was 5 mm and the treatments were delivered in free-breathing without compression belt or abdominal mask.

All patients completed the planned treatment. The mean duty cycle for the 93 treatment fractions was 95.56% (95%CI 93.6-98.1%). The mean beam-on time was 691.3 seconds (95%CI 391.3-844.7 seconds).

Globally, beam-hold occurred in all treatment fractions for a mean beam-hold count of 47.4 instances (95%CI 36-59). The mean beam-hold time of those treatment fractions was 207 seconds (95%CI 159-264). No baseline shift plan was performed due to persistent target drifts.

At the last treatment session, treatment-related toxicity assessed by CTCAE v5.0 was: 8 cases of grade 1 nausea and 5 case of grade 2 abdominal pain. No grade ≥ 3 toxicity occurred.

Conclusion

This is our first experience of a clinical application of CMM in a series of 15 consecutive patients with pancreas cancer treated with SBRT on 1.5T MR-linac. CMM can guarantee high treatment precision without significant beam-on time increase and it can allow for PTV margin reduction and dose escalation. CMM was efficaciously implemented in our clinical routine also in pancreas SBRT. The procedure was well tolerated by patients and the acute toxicity rates were mild.

FID navigator for unwrapping phase in real-time field mapping in a 0.35 T MRI-Linac

H Michael Gach, Barnali Brahma, Austen Curcuru

Washington University in St. Louis, St. Louis, USA

Abstract

Purpose: MRI-guided radiotherapy (MRgRT) systems use a rotating gantry that can produce significant off-resonances (eddy currents, center frequency shifts, and B_0 inhomogeneities). The off-resonance varies with gantry angle, velocity, and composition. Off-resonances can be measured globally using free induction decays (FIDs) or locally by acquiring B_0 field maps. Fast sequences are required to measure time-varying off-resonance while the gantry rotates.

Quantitative MRI techniques like B_0 mapping and flow velocimetry depend on phase encoding typically with a phase range of $[-\pi, \pi]$. However, phase aliasing and unwrapping may be unavoidable due to pulse sequence limitations and the large off-resonances (± 300 Hz) associated with the gantry rotation. The accuracy of phase unwrapping depends critically on the choice of starting point, direction, and baseline.

The goal of our research is to develop fast B_0 mapping to allow real-time updates to the center frequency and linear gradient (first order) shimming. Free induction decay (FID) navigators are being integrated with phase maps acquisitions to guide the phase unwrapping. The resonant frequency and linear terms of the spherical harmonics can be modeled and calculated using the phantom calibrations. The off-resonance corrections can be supplied to the MRI and adjusted during treatment using the off-resonance model.

Methods: Off-resonance was measured using a 0.35 T MRI-Linac (ViewRay MRIdian) and a 24 cm diameter spherical phantom. Center frequency offsets were measured by acquiring FIDs at 3.4 FIDs/s (TR: 290 ms, BW: 2000 Hz) during full clockwise ($35^\circ \rightarrow 180^\circ \rightarrow 360^\circ \rightarrow 30^\circ$) and counterclockwise ($30^\circ \rightarrow 0^\circ \rightarrow 270^\circ \rightarrow 35^\circ$) gantry rotations. Single-slice phase maps were also acquired from three different low-resolution ($9 \times 9 \times 7$ mm³) gradient recalled echo (GRE) sequences. Two of the sequences acquired an FID navigator immediately before each acquired phase map with the navigator serving as the ground truth. Phase maps were typically axial and acquired at isocenter.

A custom MATLAB phase unwrapping tool was developed for comparison with the FSL (FMRIB Software Library) unwrapping tool. The MATLAB tool assumes that the mean off-resonance of the phase map and its temporal continuity (voxel off-resonances) follow the FID off-resonance.

The correlation and root mean squared error (RMSE) were calculated between the FID off-resonances and the mean off-resonance from the phase maps after subtracting the off-resonance baseline (mean off-resonance over all of the measurements).

Results: Off-resonances measured using the FIDs ranged from +/-250 Hz (+/- 17 ppm), and were typically larger than those derived from the phase maps. We found superior phase unwrapping using our MATLAB tool vs FSL. We noticed significant differences (up to 3 ppm) between the FID navigator measurement and the prescan measured center frequency.

Conclusions: The FID navigator was beneficial for unwrapping phase maps. Currently, the MATLAB temporal unwrapping technique provided better results than the FSL spatial unwrapping technique. Ideally, the unwrapping algorithm should address both spatial and temporal information. Further work is required to verify the unwrapped phase maps are accurate since the FID off-resonance is a global measurement while the phase map is local.

Hybrid Learning: A Novel Combination of Self-Supervised and Supervised Learning for Joint MRI Reconstruction and Denoising without High-Quality Training Reference

Haoyang Pei^{1,2,3}, Yao Wang³, Hersh Chandarana^{1,2}, Li Feng^{1,2}

¹Bernard and Irene Schwartz Center for Biomedical Imaging, Department of Radiology, New York University Grossman School of Medicine, New York, USA. ²Center for Advanced Imaging Innovation and Research (CAI2R), Department of Radiology, New York University Grossman School of Medicine, New York, USA. ³Department of Electrical and Computer Engineering, NYU Tandon School of Engineering, New York, USA

Abstract

Purpose

MRI-guided radiotherapy (MRgRT) can be performed using commercial MRI-Linacs operating at either 0.35T or 1.5T field strengths. Imaging at 0.35T, in particular, is challenged by low signal-to-noise ratio (SNR), which necessitates either prolonged scan times to achieve adequate image quality or the use of advanced reconstruction and/or denoising techniques. The application of deep learning for MRI reconstruction and denoising has been transformative in the field of rapid MRI. However, obtaining high-quality reference images for standard supervised training is often difficult at low field strengths. In such scenarios, self-supervised learning offers a viable alternative, although its performance can be compromised when applied to highly accelerated imaging.

This work introduces a novel approach called hybrid learning for joint MRI reconstruction and denoising in applications where only low-quality reference images are available. Hybrid learning incorporates a two-stage network training process. In the first stage, self-supervised learning is used to generate high-quality images from low-quality reference data, such as images acquired at low field strengths with reduced SNR. In the second stage, the high-quality images produced in the first stage are used for supervised training to enable higher acceleration rates and enhanced denoising beyond that can be achieved with standard self-supervised learning. The performance of hybrid learning is demonstrated for lung MRI at 0.55T with low-SNR training references.

Methods

A total of 56 fully sampled 3D lung datasets were used in this study. All data were acquired on a 0.55T MRI scanner using a 3D stack-of-spirals sequence with ultrashort echo times (spiral-UTE) in single breath-hold acquisitions. 41 datasets were allocated for training and validation, while the remaining 15 datasets were reserved for evaluation.

In the first stage of hybrid learning, self-supervised denoising was applied to the fully sampled datasets to enhance SNR and generate high-quality reference images. In the second stage, supervised training was performed for joint image reconstruction and denoising using the high-quality reference images generated during the first stage. The objective of the second stage was to reconstruct and denoise the original datasets with both low SNR and an acceleration rate of 2 or 3. More details about the workflow of hybrid learning can be found in the supporting document.

Quantitative evaluation, including the computation of nMSE and SSIM, was conducted to compare the performance of hybrid learning against two approaches: (a) standard supervised learning using low-quality images as training references and (b) standard self-supervised learning without the use of training references.

Results

Hybrid learning consistently outperforms both standard supervised and self-supervised learning methods in lung MRI, demonstrating significantly improved SSIM and nMSE. Representative lung images, included in the supporting document, highlight the superior visual image quality and enhanced SNR achieved with hybrid learning.

Conclusion

This work introduces a novel hybrid learning strategy to overcome challenges when high-quality reference data is unavailable for standard supervised deep learning in image reconstruction and denoising. This approach is particularly beneficial for MRI at low field strengths (e.g., $\leq 0.5\text{T}$). In the context of MRgRT, it has potential applications for the 0.35T MRI-Linac system.

33

Beam modelling and performance evaluation of RadCalc for the Elekta Unity MRI-Linac

Samuel Rusu, Caiden Atienza, Yen-Po Lee, Joel St-Aubin, Blake Smith, Daniel Hyer

University of Iowa Health Care, Iowa City, USA

Abstract

Purpose: As adaptive radiotherapy gains popularity, the ability to perform an accurate and fast secondary dose calculation with the patient on the table becomes a critical need. This work investigates RadCalc version 7.3.2.0 as a secondary dose calculator and data transfer integrity check for adaptive therapy on the Elekta Unity 1.5 T MR-Linac. This is a particularly timely investigation as this version of RadCalc is the first to account for the lateral shift of dose profiles due to the transverse magnetic field.

Methods: Dosimetry data was imported and machine-specific settings were configured in RadCalc for the Unity using the graphical interface. Two Unity beam models were created to account for differences between dose to water (Unity_Dw) and dose to medium (Unity_Dm). These models were identical except for a 0.99 cGy/MU calibration factor applied to Unity_Dm. The Unity_Dw was used for all situations that measurements were done in water or in cases that Monaco was set to report dose to water while the Unity_Dm model was used for all patient plans. Commissioning tests outlined in AAPM MPPG5b were completed to validate the model. Point dose comparisons and 2D dose comparisons between RadCalc and Monaco were performed for patient plans to quantify agreement.

Results: RadCalc agreed within 2% or better for all MPPG5b measurements. A total of 355 plans (3579 individual beams) were created in Monaco and used for RadCalc point dose comparisons. The mean point dose deviation between the two systems was found to be $0.33 \pm 4.11\%$ ($n=3579$) per-beam and $0.34 \pm 1.00\%$ per-plan ($n= 355$). The 2D dose comparison 3%/2mm gamma pass rate was found to be 90.65 ± 2.42 per plan ($n=11$) and 90.56 ± 4.22 per beam ($n=116$) excluding plans greater than 22 cm off-axis. The data transfer integrity check correctly verified plan and machine parameters to ensure the correct plan was delivered for adaptive patients.

Conclusions: RadCalc version 7.3.2.0 provides an accurate and fast calculation of dose for adaptive radiotherapy on the Unity and allows for accurate data transfer checks.

Deep Learning Based Correction of Patient Specific Distortions from Neuro to Uro

Cornelius Eichner¹, Shihan Qiu², Radu Miron³, Yahang Li², Nirmal Janardhanan², Bryan Clifford⁴, Mahmoud Mostapha², Mariappan Nadar², Omar Darwish¹, Thorsten Feiweier¹

¹Siemens Healthineers AG, Forchheim, Germany. ²Siemens Healthineers, Princeton, USA.

³Siemens Industry Software România, Brasov, Romania. ⁴Siemens Medical Solutions USA, Inc., Boston, USA

Abstract

Purpose

Magnetic Resonance Imaging (MRI) is increasingly used in radiotherapy (RT) simulation for its high tissue contrast. In particular, diffusion-weighted imaging (DWI) is highly valuable for RT due to its sensitivity to tumor cellularity [1]. DWI enables the calculation of biomarkers that support treatment adaptation and monitoring. For these applications, high-quality, distortion-free images that accurately align with anatomical data are essential. However, the inherent B0 sensitivity of echoplanar imaging (EPI) often manifests in susceptibility-induced distortions, which may limit the reliability of the data for segmentation and dose planning. A simple method to correct B0 distortions is acquiring a reversed phase-encoding (PE) volume and applying 1D nonlinear registration between PE directions [2]. However, this method, which is optimized for neuroimaging, requires time-consuming iterative reconstruction and manual parameter tuning, restricting its broader use in RT. The aim of this research is to develop a generalized and fast deep learning (DL) approach for distortion correction in DWI suitable for multiple RT-relevant anatomies, including the pelvis, head/neck, and brain, thereby supporting improved accuracy in RT planning and treatment adaptation.

Methods and Materials

We acquired a diverse DL training dataset covering RT-specific anatomies, including the pelvis, head/neck, and brain. Data were collected from 50 healthy volunteers using 1.5T and 3T MRI systems (MAGNETOM Sola and Vida, Siemens Healthineers AG, Forchheim, Germany), following protocols optimized for each anatomy based on clinical guidelines. This approach resulted in approximately 2 hours of data acquisition per participant, generating a total of 35k slice pairs for training. Ground truth for DL training was computed using 1D non-linear co-registration between alternating PE directions.

A DL model combining the Conv2Former architecture [3] and deformable convolutional layers [4] was trained to estimate the B0 map from the input DWI pair (Fig.1). DWI images are corrected for distortion by applying unwarping and intensity correction using the estimated field [5]. A combination of unsupervised loss (i.e., similarity between the corrected image pair) and supervised loss (i.e., similarity between the DL results and the targets) was used to optimize the DL model.

Results

The proposed DL method demonstrated stable performance across all included anatomies (Fig. 2a,b). DL achieved significantly faster registration, processing approximately (0.120 s/vol), compared to iterative methods, such as TopUp (24.2 min/vol). This >10,000x speed-up enables real-time distortion correction directly at the scanner (MAGNETOM Vida), using a research sequence with one preceding reversed PE EPI volume and the DL method (Fig. 2c). Further, the DL method achieved better distortion corrected than TopUp in various cases (Fig 2d)

Conclusion

We developed a DL-based method for correcting B0 distortions in DWI across multiple RT-relevant anatomies, extending beyond neuroimaging. Distortion correction is achieved by adding a reversed PE step before actual data acquisition, requiring only one additional TR. Our method offers faster, more anatomically accurate results than traditional iterative approaches. The substantial reduction in reconstruction time enabled integrated inline correction, directly at the scanner. Our suggested method may enhance DWI accuracy, crucial for dose planning, segmentation, and biomarker-based monitoring in RT.

Automatic segmentation of prostate and urethra on T2w MRI

William Holmlund¹, Attila Simko², Karin Söderkvist², Peter Palasti³, Zsuzsanna Fejes³, Zsigmond Tamas³, Patrik Brynolfsson⁴, Tufve Nyholm²

¹Umeå University, Umeå, Sweden. ²Umeå University, Umeå, Sweden. ³University of Szeged, Szeged, Hungary. ⁴Lunds University, Lund, Sweden

Abstract

Purpose

In the context of prostate cancer treatment, radiotherapy has traditionally been delivered with a homogeneous dose to the entire prostate. Recent studies have demonstrated the efficacy of a local dose escalation to a subvolume of the prostate, so called focal boost. With the increased dose inside the prostate this highlights the importance of delineating the intraprostatic organ-at-risk (OAR) urethra, to minimize side-effects [1].

Manual segmentation of the prostate and urethra on MRI are tedious and time-consuming. Therefore, the development of an individualized, automatic method to segment the prostate and urethra is highly relevant in present medical practice.

In this work, we train and evaluate a deep learning algorithm on segmentations of the prostate and urethra and compare the results with the inter-reader variability of two radiologists.

Methods

We trained a 3D nnUNet model with five-fold cross-validation using the T2w images from the PROSTATEx [2] dataset and the ProstateZones [3] segmentation dataset. The ProstateZones dataset consists of manual segmentations of the urethra and prostatic zones on a cohort of 200 randomly selected patients from the PROSTATEx data. This cohort is divided into a training set ($n=160$) and a test set ($n=40$). In the training set, each structure was delineated once, whereas in the test set each patient were independently delineated by two different radiologists, resulting in 240 segmentations for 200 patients.

An automatic postprocessing scheme were included to output the predicted urethra in a slice-wise circular shape with a 6 mm diameter to match the structure of the manual segmentations

Model performance was evaluated using the Dice Similarity Coefficient (DSC), Surface Dice measurement and Centerline Distance (CLD). Evaluations were performed in Hero (version 2024.2.0).

Results:

An example from the test set comparing the model segmentation and the two readers is provided in Figure 1.

A full summary of the results is available in Tables 1 and 2, which displays the model performance relative to both readers on the test set and the inter-reader variability, respectively. All metrics are presented as medians with the 5th and 95th percentiles.

The model achieves prostate and urethra segmentations with median DSC scores of 0.92 and 0.41, as well as a CLD of 2.9mm for the urethra, when compared to both radiologists on the test set. For the same structures, the inter-reader variability has a median DSC of 0.92 and 0.33, and CLD of 3.6 mm.

Conclusions

In this work we show an automatic method capable of segmenting the prostate and urethra at a comparable level as two experienced radiologists.

References

- [1] – Groen, V.H. et al. (2022) ‘Urethral and bladder dose–effect relations for late genitourinary toxicity following external beam radiotherapy for prostate cancer in the flame trial’, Radiotherapy and Oncology, 167, pp. 127–132. doi:10.1016/j.radonc.2021.12.027
- [2] – Geert Litjens, Oscar Debats, Jelle Barentsz, Nico Karssemeijer, and Henkjan Huisman. "ProstateX Challenge data", The Cancer Imaging Archive (2017). DOI: 10.7937/K9TCIA.2017.MURS5CL
- [3] – Holmlund, W., Simkó, A., Söderkvist, K. *et al.* ProstateZones – Segmentations of the prostatic zones and urethra for the PROSTATEx dataset. *Sci Data* **11**, 1097 (2024). <https://doi.org/10.1038/s41597-024-03945-2>

Combining CBCT-based treatment delivery with offline MRI-guided adaptive radiotherapy: a virtual MR-linear accelerator

Silvia Fabiano, Klara Kefer, Michael Baumgartl, Riccardo Dal Bello, Michael Christian Mayinger, Jens von der Grün, Lotte Wilke, Matthias Guckenberger, Stephanie Tanadini-Lang

University Hospital Zurich, Zurich, Switzerland

Abstract

Purpose: Magnetic resonance imaging (MRI) guidance might play a pivotal role as radiotherapy advances toward daily treatment adaptation to account for inter-fractional changes in patient anatomy. Modern hybrid MR-linear accelerators (MR-linacs) enable online adaptive radiotherapy (ART) but face limited adoption due to the high costs of construction, purchase, and maintenance. Moreover, the substantial time and resource demands of each treatment session reduce patient throughput. As an alternative, this study proposes offline ART at a C-arm linac, using MR images acquired immediately before treatment for contouring and plan adaption.

Methods: The workflow illustrated in Figure 1 has been established. A base plan is prepared upfront, following institutional guidelines. On the day of adaption, T2-weighted and Dixon MR images are acquired in the treatment position using the 1.5T Magnetom Sola MR within the department. A synthetic Computed Tomography (sCT) is then generated and registered to the original planning sCT. Target structures are rigidly copied, while organs at risk (OARs) are deformed. Next, the contours are adapted by a physician using the T2-weighted image, and the plan is reoptimized by a physicist on the new sCT. Patient-specific quality assurance (PSQA) includes independent dose calculation, comparison of target volumes and monitor units with the original plan, an MLC opening complexity test, and plan recalculations with a water override. Finally, a cone beam CT (CBCT) is performed for patient setup correction, before treatment delivery.

Results: This new approach was tested on twenty patients with lymph node lesions in the pelvis. Figures 2(a-b) highlight its advantages: plan adaptation often results in improved bowel sparing, and in cases where OAR sparing is minimal, it enhances target coverage. PSQA was successful for all patients and fractions with an average passing rate of 99.6%, a mean deviation in tumor volume of 6.6%, a change in monitor units of -0.5%, and a mean target average dose variation of 1.6% after water override recalculations. On average, adapting a treatment currently takes 103 minutes, with the planning step being the most time-consuming (21 minutes).

Conclusions: The virtual MR-linac approach presented in this study offers a promising alternative to hybrid machines, that could be easier to implement in standard radiotherapy settings. It has the potential to optimize resource utilization and enhance patient throughput while exploiting advanced MR imaging using a diagnostic scanner tailored to radiotherapy needs. Although adaptation time can still be improved, the new workflow may significantly enhance patient comfort by minimizing the time spent on the treatment table.

Clinical commissioning and validation of a deep learning-based synthetic CT algorithm for MRI-only prostate radiotherapy

Jessica Scholey, Qihui Lyu, Alon Witztum, Steven Seyedin, Julian Hong, Evan Porter, Hui Lin, Ke Sheng, Emily Hirata

Department of Radiation Oncology, University of California San Francisco, San Francisco, USA

Abstract

Purpose: Despite substantial interest in MRI-derived synthetic CT (sCT) for MRI-only radiotherapy, limited recommendations exist on clinical commissioning, validation, and implementation, particularly for deep-learning (DL) techniques. The purpose of this work is to share a single institution's experience commissioning a DL sCT model for MRI-only prostate stereotactic body radiotherapy (SBRT).

Methods/Materials: Between 01/2023 and 08/2023, 135 patients undergoing prostate SBRT received gold fiducial placement for image guidance and same-day CT- and MRI-simulation. CTs were acquired at 120kVp ($1\times1\times1.5\text{mm}^3$; SOMATOM Definition, Siemens, Erlangen, Germany). MRIs were acquired at 3T (MAGNETOM Vida, Siemens) using a 3D T1-VIBE-Dixon sequence (TE1/TE2/TR=1.23/2.46/4ms, bandwidth=1090Hz/pixel, $1\times1\times1.5\text{mm}^3$, 176–224 slices, ~5min.). Selection criteria for MR-only simulation included patients weighing 150–280lbs., no pelvic/hip prostheses (Figure2c,d) and standard candidacy per institutional safety policy. A commercial deep learning-based algorithm (syngo.via, Siemens) was used to generate sCTs from in-phase and out-of-phase MRIs. A commercial, clinically validated DL-based auto-contouring model (LimbusAI, RadFormation, New York) was used to generate contour structures on CTs and sCTs. Dosimetry and image guidance was analyzed in a randomly selected subset (n=20). Clinical, CT-based treatment plans were generated using 6MV volumetric-modulated-arc-therapy and forward calculated onto sCTs using fixed plan parameters. Plans were compared using gamma analysis and dose to 95% prostate volume (D95%). A sCT-specific CT calibration curve was created by tuning Hounsfield Unit (HU)-to-mass density to best match CT vs. sCT gamma metrics and prostate D95% (population averaged). Fiducial markers were defined using the T1-VIBE-Dixon water-only sequence. CBCT-to-sCT validation was performed through blinded, fiducial-based alignment of datasets on the C-arm linear accelerator used for treatment. Patient-specific quality assurance (QA) of sCTs was achieved through visual inspection of sCT-vs-T1-water-only MRI.

Results: Versus CTs, sCTs saw significant disagreement in rectum HU (due to rectal gas present in CTs but not in sCTs) and bladder HU and volume (due to difficulty maintaining full bladder for duration of MR-simulation). No statistically significant differences were seen in volumes or HUs of bony structures. The CT calibration curves were identical, except for mass density of 1g/cc defined as -10HU instead of +10HU for the sCT versus CT curve, respectively. Gamma passing rates between dose distributions in the clinical CT plan versus distributions in the forward calculated sCT plan were $99.5\pm0.6\%$, $98.9\pm0.8\%$, and $96.4\pm1.8\%$ at 3%/3mm, 2%/2mm, and 1%/1mm, respectively. Dose to 95% of the PTV on the CT vs. sCT plans agreed to within $0.51\pm0.1\%$. sCT-based versus CT-based fiducial alignment agreed to within -

0.05 ± 0.25 mm, 0.03 ± 0.69 mm, and 0.02 ± 0.67 mm in the lateral, longitudinal, and vertical directions, respectively. Visual patient-specific QA was effective in identifying model failures (Figure2a,b).

Conclusion: The clinically commissioned DL-based MR-to-sCT model with sCT-specific calibration curve provided excellent dosimetric agreement with CT. Fiducials can be visualized on MRI and used for on-board alignment. Auto-contouring is a useful tool for sCT evaluation due to its speed, practicality, and reduced bias relative to manual users. The proposed method provides an effective framework for commissioning and validating a DL-based method for MRI-only radiotherapy.

MR-Guided Adaptive Radiotherapy in Prostate Cancer Patients: Deformable Dose Accumulation and Toxicity Analysis

Nima Hassan Rezaeian¹, Chengcheng Gui¹, Lando Bosma², Sudharsan Madhavan¹, Sarah Burleson¹, Nicolas Cote¹, Victoria Brennan¹, Neelam Tyagi¹

¹Memorial Sloan Kettering Cancer Center, New York, USA. ²UMC Utrecht, Utrecht, Netherlands

Abstract

Purpose/Objective(s): To conduct deformable dose accumulation for prostate cancer patients receiving MR-guided radiotherapy (MRgRT).

Materials/Methods: Over 100-intermediate-risk prostate cancer patients received daily online MR-guided adaptive re-planning on a 1.5-Tesla MR-LINAC system, with a prescribed dose of 40Gy in 5fractions and a 45Gy boost targeting the dominant-intraprostatic-lesion(DIL). Daily target and normal organ contours were generated based MR images prior to treatment, followed by adaptive plan creation. A workflow in MIM was developed to register and deform pre- and post-treatment MR images for each fraction, capturing intra-fraction displacement-vector-fields(DVFs) using a multimodality deformable image registration method with a normalization and smoothness factor of 0.5. Inter-fraction deformation was applied across daily fraction images. Quality assurance of deformable image registration(DIR) and deformed contours was assessed using metrics such as the Hausdorff-Distance at the 95th percentile(HD95), Jacobian determinant(JD), Curls, and DICE coefficient. Additionally, a ground truth prostate dataset with an empty bladder was simulated, based on biomechanical properties of pelvic organs, and then deformed to represent a full bladder state. Ground truth contours and displacement-vector-fields(DVFs) were compared to results from the MIM deformable-image-registration (DIR) method. Accumulated dose metrics—Dmax, D10%, and D50%—for the bladder, urethra, and rectum were extracted and assessed against our institutional dose constraints: bladder(Dmax<42Gy, D10%<36Gy, D50%<20Gy); urethra(Dmax<42Gy); and rectum(Dmax<41.2Gy, D1cc<38.5Gy). Genitourinary(GU) toxicity was evaluated using an increase of more than 10-points in the International-Prostate-Symptom-Score(IPSS) and by CTCAE criteria for acute events (within-180-days of the first adaptive RT fraction) and late events(>180-days). We also estimated the average normal tissue complication probability(NTCP) for rectum.

Results: Dose accumulation analysis was completed for the first 73-patients. Comparison of Jacobian-determinant(JD) between the MIM DIR method and the ground truth dataset yielded values of 1.04 ± 0.73 vs. 0.94 for the bladder, 1.02 vs. 0.96 for the rectum, and 0.93 vs. 1.01 for the prostate. For these cases, prostate, rectum, and bladder metrics for HD95, JD, Curl, and DICE were as follows: prostate ($1.38 \pm 0.64, 1.08 \pm 0.12, 0.16 \pm 0.06, 0.88 \pm 0.06$); rectum ($1.10 \pm 0.58, 1.05 \pm 0.09, 0.21 \pm 0.06, 1.10 \pm 0.58$); and bladder ($2.50 \pm 1.38, 0.84 \pm 0.22, 0.21 \pm 0.06, 0.83 \pm 0.07$). Due to its small size, the urethra presented the lowest values for DICE, Curl, and HD95. The average accumulated Dmax doses were 4124 ± 135 cGy for the bladder, 4263 ± 1.17 cGy for the urethra, and 3978 ± 502 cGy for the rectum. Bladder D10% and D50% doses averaged 3484 ± 274 cGy and 1953 ± 783 cGy, respectively. The rectum's average accumulated D1cc dose was 3409 ± 466 cGy. Acute urinary toxicity was observed in two patients, with late toxicity in one patient. Urethra Dmax exceeded institutional

constraints by more than 100cGy in average for five patients, and one patient's bladder D_{max} exceeded constraints by 150cGy. We estimated the average NTCP for rectum 0.97%±0.15%.

Conclusions: D_{max}for urethra exceeded our constraints for 59out of 73patients. Considering statistical uncertainty for our Monte-carlo calculation only 32out of 73exceeded D_{max}for urethra. NTCP for rectum is with the expected institutional range. Institutional constraints need to be reevaluated based on accumulated doses rather than planned dose.

Deep-Learning-Enabled Segmentation of Intraprostatic Gold Fiducial Markers for MR-only Radiotherapy Planning

Ashley Stewart¹, Jonathan Goodwin^{2,3}, Matthew Richardson², Simon Robinson^{4,5}, Kieren O'Brien^{6,1}, Jin Jin^{6,1}, Markus Barth¹, Steffen Bollman¹

¹University of Queensland, Brisbane, Australia. ²Calvary Mater Hospital, Newcastle, Australia.

³University of Newcastle, Newcastle, Australia. ⁴Medical University of Vienna, Vienna, Austria.

⁵Medical University of Graz, Graz, Austria. ⁶Siemens Healthcare Pty Ltd, Brisbane, Australia

Abstract

Purpose

Radiotherapy (RT) in prostate cancer (PCa) often requires insertion of gold fiducial markers (FMs) for treatment planning and prostate position matching on the day of treatment. In MRI, FMs and calcifications appear as signal voids, complicating differentiation. In this work we evaluate a deep-learning-enabled model for automated segmentation of FMs that may facilitate MR-only workflows in patients with visual ambiguity in FM location due to the presence of calcifications.

Methods

25 PCa patients with FMs underwent CT and MRI, including T1 and GRE acquisitions. Calcifications were present in 12 patients. GRE data were processed using QSMxT producing quantitative susceptibility maps (QSM), susceptibility-weighted imaging (SWI), and R2* maps. FMs and calcifications were manually segmented using ITK-SNAP, with CT as a reference. 3D U-Nets were implemented (fastMONAI) to segment calcification and FM regions. U-Nets used five levels with channels (16, 32, 64, 128, 256). The loss function combined Dice loss and cross-entropy loss with one-hot encoding applied to the target masks. Performance was evaluated using precision / recall calculated at FM level with leave-one-out cross-validation. Separate U-Nets were trained for each contrast.

Results

Trained U-Nets generated segmentations and confidence maps for each label (see **Fig.1**).

U-Nets trained on CT achieved perfect recall and 99% precision (see **Table 1**). MRI-based contrasts achieved 92-99% recall and 81-87% precision, indicating MRI-based models are excellent at identifying markers, but cannot always distinguish from calcification.

Conclusion

MRI can reliably identify intraprostatic gold FMs. However, challenges remain in differentiating FMs from calcification. Future work explores model consensus-based approaches, increasing information gained across MR contrasts. Approaches to clean model outputs using morphological operations and hyperparameter tuning may aid in segmentation precision, and automation of the MR-only workflow.

Synthesis of 3T T2-weighted MRI from TrueFISP MRI acquired on a 0.35T MR-Linac system

Yu Gao, Lawrie Skinner, Dimitre Hristov, Cynthia Chuang, Lianli Liu, Lei Xing, Hilary Bagshaw, Mark Buyounouski

Department of Radiation Oncology, Stanford University, Palo Alto, USA

Abstract

Purpose

MR-guided radiation therapy represents a significant advancement in cancer treatment, allowing for optimized treatment delivery by adapting to changes in patient anatomy. The low-field MR-guided system primarily utilizes the TrueFISP sequence, which, while effective for anatomical alignment, lacks the rich diagnostic detail that can be provided by multiparametric MRI. Additionally, images from the low-field onboard MR scanner have higher noise level due to the inherent limitations of lower magnetic field strength. The purpose of this work is to synthesize high-quality diagnostic T2-weighted (T2-w) MR images from the TrueFISP MRI of the low-field MR-Linac system to better assist the MR-guided program.

Materials and Methods

Fifteen prostate cancer patients treated using the ViewRay MRIdian system were selected for this study. For each patient, T2-weighted reduced field of view SPACE MRIs were acquired using a 3T diagnostic scanner (Siemens MAGNETOM Skyra), and TrueFISP MRIs were obtained from the ViewRay onboard 0.35T MRI scanner. The low-field MR images were cropped to match the dimensions of the 3T reduced field of view T2-w MRI. A CycleGAN network was trained and optimized to perform image-to-image translation between the two sets of MRIs. A total of 796 slices from 12 patients were used for training, and 192 slices from the remaining 3 patients were allocated for testing. The network was trained on NVIDIA GeForce RTX™ 4090 with 200 epochs.

Results

The training took approximately 3.5 hours to complete. The network converged well on the training dataset. With the trained network, the reconstructed images matched closely with the real MRI. It was observed that the synthetic images demonstrated pronounced T2-weighted contrast, which drastically enhanced the visualization of tissue characteristics in comparison to the low-field TrueFISP MRI. Mild breathing motion artifacts were observed in the second and third testing patients. The network is robust to motion and generated artifact-free T2-weighted images despite the presence of mild breathing motion artifacts in the original TrueFISP scan.

Conclusions

A deep learning-based model was trained to synthesize 3T T2-weighted MRI from 0.35T TrueFISP MRI. This preliminary study demonstrated the feasibility of translating MRI contrast as well as improving the image quality for the low-field MR-Linac system. This improvement could potentially allow for more precise tumor and organ at risks delineation.

Motion management in MR-guided prostate radiotherapy – are the technical advancements living up to the expectations?

Emilia Persson^{1,2,3}, Björn Eiben¹, Simeon Nill¹, Alex Dunlop¹, Andreas Wetscherek¹, Alison C. Tree⁴, Uwe Oelfke¹

¹Joint Department of Physics, The Royal Marsden Hospital and The Institute of Cancer Research, Sutton, United Kingdom. ²Radiation Physics, Department of Hematology, Oncology and Radiation Physics, Skåne University Hospital, Lund, Sweden. ³Department of Translational Medicine, Lund University, Malmö, Sweden. ⁴Royal Marsden NHS Foundation Trust and the Institute of Cancer Research, Sutton, United Kingdom

Abstract

Purpose

With the clinical introduction of motion management strategies in MR-guided radiotherapy, such as automatic beam gating, an increased precision in the treatment delivery is expected. This would boost confidence to reduce margins and increase fraction doses, with an expectation of improved target coverage and protection of critical organs. The question is however, are the technical advancements living up to the expectations?

This work investigates the dosimetric impact of introducing gated MR-guided prostate treatments in combination with a margin reduction. Gating was compared to MLC-tracked treatments, further exploring future possibilities of advanced motion management techniques.

Methods

Five prostate cancer patients, treated in the two-fraction arm of the HERMES-trial (NCT04595019, Westley et al., 2022), were retrospectively investigated in this work. Patients received treatments on the Unity MR-linac (Elekta AB, Stockholm, Sweden), prescription dose of 24Gy to cover 95% of the PTV (3mm CTV to PTV margin). Additional treatment plans with a reduced margin of 2mm were created using the initial clinical optimization template with manual adjustments where required.

Intra-fraction prostate motion was estimated using an optical-flow registration method based on 2D-cine MR-images. Treatment delivery for the original plan was simulated and delivered dose reconstructed using gating with a 3mm threshold and MLC-tracking, where the MLC-aperture was shifted according to detected prostate motion. A simulation using a 2mm gating threshold was added to the 2mm margin plan. Patient specific fraction doses were reconstructed using the software TrackAdapt (Persson et al. 2024), combining treatment plan information from research Monaco (v.6.09.01, Elekta AB, Stockholm, Sweden), DynaTrack (Fast et al. 2014), GPUMCD (Ahmad et al. 2016, Hissoiny et al. 2011) and patient specific motion. Reconstructed doses were compared to a baseline simulation assuming

zero target motion. Wilcox signed-rank test was used to compare methods with significance level of 0.05.

Results

Intra-fraction prostate motion was below 3mm and 2mm for 85% and 75% of the fractions respectively. For the 3mm margin, the CTV D95% was fulfilled for all but three fractions, violating 24Gy by 0.41Gy, 0.28Gy and 0.04Gy for three gated fractions. For two of these fractions, planning with 2mm margin increased the target dose by 0.5Gy and 0.3Gy, and the CTV D95% was above 24Gy.

There was no statistically significant difference in using a 2mm or 3mm gating window for the CTV D95%, PTV D95%, or the D2% for rectum, bladder, urethra. Compared to gating, MLC-tracking increased the dose to targets and organs at risk for both margins.

Median gated treatment duty cycle was 0.99 (2mm) and 1.00 (3mm) with a minimum of 0.94 and 0.95 respectively. There was no statistical difference in duty cycle between 2mm or 3mm gating window.

Conclusions

Gated MR-guided treatment delivery is robust for intra-fraction prostate motion and margin reduction. Ensuring target coverage for the majority of fractions, without compromising on organs at risk and with minimal impact on duty cycle, gating is living up to its expectations. MLC-tracking may enable higher target doses, however, requires careful consideration of the dose to organs at risk.

Computed diffusion-weighted imaging and apparent diffusion coefficient for monitoring treatment response in prostate cancer: an MR-Linac feasibility study

Satomi Higuchi^{1,2}, Jonathan Goodwin^{2,3}, Hilary Byrne¹, Michael Jameson^{1,4}, Jeremy de Leon¹

¹GenesisCare, Sydney, Australia. ²University of Newcastle, Newcastle, Australia. ³Calvary Mater Newcastle Hospital, Newcastle, Australia. ⁴University of Wollongong, Wollongong, Australia

Abstract

Purpose The integration of MRI and linear accelerator in the 1.5T MR-Linac system enables precise visualization and accurate treatment delivery in prostate cancer, making it a valuable tool for adaptive and image-guided workflows due to intra-fraction motion and inter-fraction anatomical changes. Furthermore, the use of Diffusion-weighted imaging (DWI) and its derivative, the apparent diffusion coefficient (ADC), may provide an additional functional approach to treatment adaptation based on treatment response. However, the qualitative and quantitative capabilities of DWI on the 1.5T MR-Linac remain underexplored in prostate cancer patients, particularly due to the system's limitations, such as restricted gradient power, which restricts the use of b-values > 500 sec/mm²; significantly less than typical b-values ~1400 sec/mm² used in prostate cancer DWI. This study explores the use of computed high b-value DWI to overcome the limitations in gradient power, and qualitatively assesses ADC values in the phantom model as well as radiation induced changes in a cohort of prostate cancer patients.

Methods An isotropic diffusion phantom (CaliberMRI, Colorado, USA), was scanned four times. The design of this phantom includes an inner and outer ring of vials with varying concentrations (10, 20, 30, 40, and 50%) of polyvinylpyrrolidone. Computed DWIs (cDWI) for b-values of 800, 1000, 1500, and 2000 s/mm² were generated using b-values of 150 and 500 s/mm². DWI image data from nine prostate cancer patients with a PI-RADS score of 4 or 5 and Gleason score 4+3 = 7, treated with a 1.5 T MR-Linac (Unity, Elekta AB, Stockholm, Sweden), were included in an ethically approved retrospective study. The treatment protocol delivered 45 Gy to the gross tumour volume (GTV) and 40 Gy to the whole prostate as a clinical target volume (CTV) over five fractions in 10 days. DWI was performed daily before treatment when possible. Computed b=2000 s/mm² DWIs were generated from b-values of 150 and 500 s/mm² using a mono-exponential model. ADC values were extracted from the radiation oncologist-contoured GTV on T2-weighted images, as well as from threshold-based contour on the cDWI, and CTV, urethra and spacer gel.

Results Signal intensity of the vials with concentrations of 10% to 50% were not distinguishable on the measured b=500 DWI, whereas 10% to 40% were distinguishable using computed b=2000 DWI (Figure 1). High b-value cDWI generated using b-values of 150 and 500, demonstrated better contrast-to-noise ratio (CNR) compared to measured b=500 DWIs in the tumor regions of prostate cancer patients. ADC values within the contours, derived from both measured low b-value DWI and cDWIs, showed an increase compared to pre-treatment values. ADC values extracted from cDWI contours revealed a more pronounced increase in response to radiation therapy (see Figure 2).

Conclusions Computed high b-value DWI is effective in identifying tumor regions. ADC values increased within the GTV, where cancer was present, while no consistent ADC changes were observed in the CTV or spacer gel areas. These findings highlight the potential of ADC measurements to monitor daily treatment response in prostate cancer patients using MR-Linac systems.

Enhancing accuracy and precision of IVIM estimates as imaging biomarkers for radiation therapy

Elina Petersson¹, Maria Ljungberg^{1,2}, Maja Sohlin^{1,2}, Oscar Jalnefjord^{1,2}

¹Department of Medical Radiation Sciences, Institute of Clinical Sciences, Sahlgrenska Academy, University of Gothenburg, Gothenburg, Sweden. ²Department of Medical Physics and Biomedical Engineering, Sahlgrenska University Hospital, Gothenburg, Sweden

Abstract

Introduction

Diffusion-weighted MR imaging (DWI) is sensitive to microscopic tissue structures, enabling characterization of tumor composition. Given the critical role of the tumor microenvironment in influencing therapeutic responses, particularly radiotherapy (RT)¹, DWI holds promise for RT planning and response assessment. In intravoxel incoherent motion (IVIM) analysis, DWI signals are modeled with diffusion and perfusion compartments², but parameter estimates are heavily influenced by b-value schemes and model selection. This study optimizes b-value schemes for the simplified diffusive IVIM model (sDiffusive)^{2,3} to reduce variability and bias and introduces a simplified ballistic flow IVIM model (sBallistic)⁴. These advancements aim to deepen insights into brain tumor microstructure, aiding effective RT planning.

Methods

Simplified diffusive IVIM:

We optimized the b-value scheme for the sDiffusive model by minimizing a cost function combining the Cramér-Rao lower bound of f and bias from estimation errors based on an intermediate model⁵. Typical brain parameters ($f=1\text{--}3\%$, $D=0.8\times 10^{-3}\text{ mm}^2/\text{s}$, $K=0.5\text{--}1.5$, $\tau=100\text{--}300\text{ms}$, $v=2\text{ mm/s}$, $\text{SNR}=70$)⁵⁻⁷ were used. Simulations (1000 noise realizations) and *in vivo* 3T MRI scans validated the scheme. Data preprocessing with FSL tools generated parameter maps via a Bayesian approach. Regions of interest (ROIs) in white and gray matter were analyzed.

Simplified ballistic IVIM:

To address uncertainties and scan time for the ballistic IVIM model, we propose the sBallistic model, assuming significant perfusion attenuation in non-flow-compensated scans:

$$S=S_0 \cdot [(1-f)e^{-b \cdot D} + f e^{-b \cdot D_b} \delta(c)]$$

with blood-diffusion coefficient $D_b=1.75 \cdot 10^{-3}\text{ mm}^2/\text{s}^2$, and c denotes sensitivity to ballistic flow. The model was tested via simulations using flow- and non-flow-compensated b-values (0;10;20;30;50;100;200s/mm²) with tissue parameters matching diffusive models.

Results

The optimized b-value scheme for the sDiffusive model reduced parameter estimation errors for f and D compared to reference schemes. In vivo analysis showed comparable dispersion of f and D between optimized and sDiffusive reference schemes, both outperforming the diffusive reference scheme. The optimized scheme produced slightly higher D, potentially indicating reduced kurtosis bias. The sBallistic model reduced parameter estimation errors relative to the conventional ballistic model.

Discussion

The optimized b-value scheme for the sDiffusive model enhances precision, potentially enabling shorter scans and broader clinical use of IVIM imaging. The higher D-values suggest reduced kurtosis bias, with findings indicating that brain imaging may require a lower maximum b-value ($\sim 600\text{s/mm}^2$) than the conventional 1000s/mm^2 . The absence of this effect for f warrants further study. The sBallistic model demonstrated promising error reduction in simulations, and ongoing efforts will refine this model and validate the sDiffusive scheme.

Conclusion

The sDiffusive IVIM model with optimized b-value scheme improves parameter precision and reduces kurtosis bias in brain imaging. The sBallistic model offers additional potential for improving parameter estimates, supporting its further development.

References

- 1.Barker et al. Nat Rev Cancer 15(7):409–25(2015)
- 2.Le Bihan et al. Radiology 168:497–505(1988)
- 3.Sénégas et al. ISMRM(2012)
- 4.Ahlgren et al. NMR Biomed 29:640–649(2016)
- 5.Rosenqvist et al. ISMRM(2024)
- 6.Lätt et al. J Magn Reson Imaging 37:610–618(2013)
- 7.Jalnefjord et al. Magn Reson Med 92(1):303-318(2024)

Determine the isocenter and its size for MR Linac UNITY Part1: (U V) of CAX

Tanxia Qu, Hesheng Wang, Ting Chen, Siming Lu

NYU Langone Health, NYC, USA

Abstract

[Purpose]

This is the first of two-part series aimed at determining the isocenter position (the point in 3D space that minimizes the sum of distances (Euclidean Norm) to the MLC's central axis (CAX) and isocenter size (the largest distance) for a MR LINAC UNITY. A system named Source Target Guide framework is used. UNITY's Source Subsystem (SS) consists of an MLC with and JAW hosted on an non-rotational collimator fixed on an O-ring. Its Target Subsystem (TS) is a table which can only move in Z direction. Its Guide Subsystem (GS) consists of an MV EPID for machine QA and an MRI for patient position and motion management. This work aims to measure SS's (U V) of CAX to verify vendor provided.

[Methods and Materials]

We measured and calculated U values for 12 gantry angles by detecting the outer edges of the field formed by MLC leaves 39, 40, 41, and 42 (Figure 1), using an in-house MATLAB pixel-level Canny edge detection algorithm. The V values of the 12 gantry angles were measured and calculated by detecting the edges of the triangles (Figure 2), and calculated the cross points on both sides, and average the V values.

[Results]

The measured [U, V] have mean values in [512.5, 651.1] compared with vendor's [511.3, 651.4], respectively.

The small standard deviation (<0.1%) suggests that the O-ring structure is robust. The relative positioning between the MLC and EPID is stable and independent of gantry angles. The small diff between different measurement time suggests that the system is stable, and we can feel comfortable to measure (U, V) and BB's (u, v) separately.

The largest discrepancy in U and V between the institute and Elekta measurements were observed 0.3 mm and 0.4 mm at gantry angle of 300° and 120°, respectively. The average U and V are .2 pixel and .1 pixel different from that at gantry zero, respectively. The pink '+' in EPID is an accurate marker to line up physics QA instrument such as profiler.

[Conclusions]

Our independent measurements verify the vendor's (U, V) values for the CAX, with a maximum discrepancy of 0.4 mm. This confirms the rigidity and stability of the Elekta MR-LINPAC's Source Subsystem, as the position of the MLC relative to the EPID/MVI remains unchanged across varying gantry angles.

61

Determine the isocenter and its size for MR Linac UNITY Part2: (u v) of BB and isocenter position and size

Tanxia Qu, Hesheng Wang, Ting Chen, Siming Lu

NYU Langone Health, NYC, USA

Abstract

[Purpose]

This is the second of a two-part series aimed at determining the isocenter position (the point in 3D space that minimizes the sum of distances (Euclidean Norm) to the MLC's central axis (CAX) for the chosen gantry angles) and isocenter size (the largest distance) for our MR Linac UNITY.

The isocenter point is determined by Source Subsystem (SS), and shall be the reference point to calibrate the Guide Subsystem (GS), and to which the Target Subsystem shall move to.

The isocenter size is the first part of the three components to estimating/calculating CTV-PTV margin. The other two are the GS's accuracy of treatment isocenter of TPS to radiation isocenter, and the target motion during treatment. MR_Linac offers real time motion management.

We measured the (u, v) of a BB and calculate the isocenter position and its size with the (U, V) from another abstract (part 1).

Two cases of 4 cardinal gantry angles and 12 gantry angles are chosen to compare.

[Methods and Materials]

The stationary BB is used as the origin for a 3D XYZ coordinate system, which is gantry angle independent. Case 1 chosen the four cardinal angles. The isocenter in XY plane is the center of the box formed by the four CAX lines (Figure 1). This intuitive result is used to verify the in-house matlab algorithm. Case 2 chosen the 12 gantry angles of 0:30:360 degrees. Our method does not assume the origin of all CAX don't change.

[Results]

With the current BB position as the origin, the isocenter position and size are listed in two cases of 4 gantry angles and 12 gantry angles.

Defined by 4 cardinal gantry angles, Isocenter position in: (3.5, -3.3, 3.0) pixels, or (0.8, -0.7, 0.6) mm. Isocenter size = 1.5 pixel, or 0.4 mm, in both 0 and 180 degrees.

Defined by 12 cardinal gantry angles, Isocenter position in: (3.8, -1.3, 3.1) pixels, or (0.8, -0.3, 0.7) mm. Isocenter size = 3.1 pixel, or 0.7 mm, at gantry of 270 degree.

Next, we shall choose 36 or 72 gantry angles to see if the dependency of isocenter size to the number of gantry angles.

[Conclusions]

The results verified vendor performed parameters. The isocenter size in MRL is determined by SS only. For rotation able table, the BB moves and the isocenter size could be different.

Advanced denoising enables high-resolution diffusion MRI in radiotherapy

Patrik Brynolfsson^{1,2}, Ivan Rashid², Minna Lerner^{1,2}, Lars E. Olsson^{1,2}

¹Radiation physics, Dept. of Hematology, Oncology and Radiation Physics, Skåne University Hospital, Lund, Sweden. ²Dept. of Translational Medicine, Medical Radiation Physics, Lund University, Malmö, Sweden

Abstract

Purpose

Diffusion measurements often suffer from low signal-to-noise ratio (SNR). Advanced diffusion techniques such as multidimensional diffusion (MDD) measurements for microstructural imaging faces even greater challenges due to higher b-values, longer echo times, and diffusion gradients that do not fully utilize available gradient strengths because of varying b-tensor shapes. Previous studies demonstrated that MDD can be performed in a radiation therapy (RT) setup using RT coils and fixation masks at a resolution of $3 \times 3 \times 3 \text{ mm}^3$, with no applied denoising methods [1]. Noise in conventional magnitude images is not gaussian and imparts a bias signal for low SNR, so optimal denoising must be performed on the complex signal as part of the image reconstruction. This study aimed to determine the highest achievable resolution for MDD imaging using different denoising methods.

Methods

MDD imaging with spherical diffusion encoding was performed on a healthy volunteer using 31 spherical b-tensor acquisitions with $b=2000 \text{ s/mm}^2$. Seven resolutions were tested: 3^3 , 2.8^3 , $2 \times 2 \times 4$, $2 \times 2 \times 3$, 2^3 , 1.6^3 , and 1.25^3 mm^3 . Data were collected using an RT coil configuration on a 3T Signa Architect (GE Healthcare, Milwaukee, WI, US) with a moderate gradient strength of 43 mT/m.

SNR was calculated as the mean signal divided by the standard deviation in each voxel across the 31 images. To evaluate SNR performance, two metrics were used: the fraction of voxels within a white matter ROI with $\text{SNR} > 3$ (Q3) and $\text{SNR} > 6$ (Q6). These metrics were compared to the Q3 and Q6 values of the 3^3 mm^3 resolution image. Analysis was performed using Hero 2024.2.0 (Hero Imaging AB, Umeå Sweden)

Two denoising methods were tested. Air Recon DL (ARDL), an AI-based technique developed by GE Healthcare, processes complex data directly on the scanner. Tensor Marchenko-Pastur PCA (tMPPCA) [2], which uses principal component analysis and a noise floor estimate, was applied to manually reconstructed complex signal data to preserve signal integrity.

Results

At 3^3 mm^3 resolution, the Q6 value without denoising was 0.74. Using tMPPCA, resolutions of 1.6^3 mm^3 and 1.25^3 mm^3 achieved Q6 values of 0.77 and 0.71, respectively. ARDL produced a Q6 of 0.605 for the 3^3 mm^3 resolution. For Q3, the 3^3 mm^3 resolution yielded a value of 1. tMPPCA maintained similar Q3

values for resolutions of 2^3 mm 3 (1.00), 1.6^3 mm 3 (0.99), and 1.25^3 mm 3 (0.98). In contrast, ARDL yielded a Q3 of 0.98 at $2 \times 2 \times 3$ mm 3 but dropped to 0.73 at 2^3 mm 3 .

Conclusions

Denoising MDD measurements with tMPPCA applied to complex data achieves SNR levels comparable to 3 3 mm 3 resolution without denoising at resolutions as high as 1.6 3 mm 3 . These results highlights the potential to enhance the clinical utility and precision of advanced MRI methods in a radiotherapy setting.

1. Brynolfsson P et al. Tensor-valued diffusion magnetic resonance imaging in a radiotherapy setting. *Physics and Imaging in Radiation Oncology*, 24, 144–151.
2. Olesen JL et al. Tensor denoising of multidimensional MRI data. *Magn Reson Med*. 2023 Mar;89(3):1160–72.

A Large foundation models for MRI abdominal OARs segmentation

Jue Jiang, Nicolas Cote, Ifeanyirochukwu Onochie, Sharif Elguindi, Neelam Tyagi, Harini Veeraraghavan

Memorial Sloan Kettering Cancer Center, New York, USA

Abstract

Purpose

To assess feasibility to leverage a pretrained foundation model created on commonly available computed tomography (CT) datasets for application to segment organs on magnetic resonance imaging (MRI) datasets.

Methods

A hierarchical shifted window transformer-based foundational model created on a large number of ($n = 10,412$) unlabeled CT scans using self-supervised learning (SSL) approach within a published self-distillation masked image transformer model (SMIT)[1] was utilized to create a segmentation model for MRI datasets. The pretrained model's encoder weights were retained and combined with a Unet style convolutional decoder to provide a hybrid transformer-convolutional network model for segmentation. The resultant model consisted of 0.56B parameters and was subjected to fine-tuning on a relatively small number ($n = 30$) of labeled T2-weighted fast spin echo (FSE) magnetic resonance images acquired on a 1.5 Tesla MR-Unity system from patients with locally advanced pancreatic cancer treated with 5 fraction ablative radiation therapy. The model was trained to generate automated segmentation of multiple organs at risk (OARs) including the large bowel, small bowel, stomach, duodenum, and the liver. Segmentation accuracy was computed on testing datasets that were provided only at the end of training after model weights were “locked” by comparing model segmentations against expert delineation using Dice similarity coefficient (DSC) and Harsdorf distance at 95th percentile (HD95). Testing was performed on ?? datasets.

Results

The segmentation accuracy of DSC and HD95 are summarized in Table 1. As shown, the AI model was capable of providing highly accurate segmentation for the liver, stomach and duodenum structures. However, its accuracy was relatively low for the large bowel (DSC of 0.77 ± 0.16) as well as the small bowel (DSC of 0.57 ± 0.22).

Conclusion: Our analysis showed that foundation model pretrained on large scale CT datasets has limited value for MR datasets, with high accuracy achieved for some organs such as the the liver, stomach and duodenum but the accuracy was limited for large and small bowel, indicating limited efficacy of models created in one modality for a different modality.

Reference

- [1] Jiang, Jue, Neelam Tyagi, Kathryn Tringale, Christopher Crane, and Harini Veeraraghavan. "Self-supervised 3D anatomy segmentation using self-distilled masked image transformer (SMIT)." In *International Conference on Medical Image Computing and Computer-Assisted Intervention*, pp. 556-566. Cham: Springer Nature Switzerland, 2022.

Enhancing MRI in Radiation Therapy (RT) Applications with Deep Learning Image Reconstructions

Ramin Jafari¹, Sandeep Panwar Jogi², Johannes M Peeters³, Sandeep Ganji¹, Can Wu², Victoria Yu²

¹Philips, Cambridge, MA, USA. ²Memorial Sloan Kettering Cancer Center, New York, NY, USA.

³Philips, Best, Netherlands

Abstract

PURPOSE:

In MRI-guided radiotherapy (RT), contouring is a crucial step where the tumor and surrounding organs-at-risk (OAR) are delineated, as the radiotherapy plan is inversely optimized using the delineated contours to maximize dose to the tumor while minimizing dose to surrounding OARs. MRI with high signal-to-noise ratio (SNR), high spatial resolution, and reduced distortions are desired for this purpose. In this work, we evaluate the ability for deep learning reconstruction to enhance image quality in RT with potential to further improve treatment management.

METHODS:

Twenty-two MR acquisitions were performed on seven pelvic cancer patients using two Philips 3.0T systems with anterior torso and posterior coils. cervical cancer cases, patients had multiple scans which were performed pre-treatment and weekly during the radiotherapy treatment course. Prostate cancer cases had one pre-treatment MR simulation study.

FDA approved compressed-SENSE (CS) acquisition and reconstruction was performed as the reference for this study. From the same acquisition and raw data, prototype vendor-specific deep learning reconstruction method known as Precise was used for reconstruction to improve SNR and increase resolution. CS and Precise reconstructions were compared qualitatively and quantitatively (SSIM and PSNR) in a representative slice with pathology. Deep-learning based organs-at-risk auto-segmentation was performed on both CS and Precise images for all cases to determine whether the proposed method would influence the delineation results of non-subjective auto-contouring. Mean Distance to Agreement (MDA) and Dice scores were calculated between the sets of resulting segmentations. In addition, for the prostate cases, the Dice score and MDA were also calculated by comparing the auto-segmentation results against the clinically utilized contours and correlation plots were generated.

RESULTS:

Qualitative comparisons of CS and Precise demonstrates enhancements particularly pertinent to RT. Notable improvements in lesion conspicuity were seen for prostate-dominant lesions. Precise demonstrates additional areas where the visualization of OARs or tumor boundaries were improved,

potentially improving the accuracy of OAR sparing in RT. The $\mu \pm \sigma$ of SSIM and PSNR calculated from all CS and Precise image pairs were 0.97 ± 0.006 and 0.97 ± 0.01 and 38.60 ± 1.17 , respectively, illustrating that Precise maintained structure similarity while achieving SNR boost. The $\mu \pm \sigma$ of MDA and Dice coefficient between all auto-segmentations from CS and Precise images were 0.24 ± 0.17 mm and 0.97 ± 0.02 for prostate cases and 0.88 ± 0.94 mm and 0.93 ± 0.06 for cervical cases, respectively, showing good agreement of auto-segmentations. When compared with clinically utilized contours for the prostate cases, Dice of all contours for CS and Precise were 0.82 ± 0.08 and 0.82 ± 0.09 , and MDA of all contours for CS and Precise were 1.64 ± 0.63 mm and 1.61 ± 0.70 mm. This result indicates a slight, although not statistically significant, improvement in agreement with clinical contours when Precise was utilized.

CONCLUSIONS:

The application of deep learning reconstruction in oncology to enhance image quality and potentially improve radiation treatment planning has been demonstrated. While the acquisitions in this study were 2D, moving to 3D acquisitions will not only improve segmentation and volumetric contouring confidence but also provide additional potential to accelerate image acquisitions.

Installation and Initial Evaluation of a New Low Field MR Simulator for Radiotherapy

Joshua Kim¹, Amanda DiCarlo¹, Anthony Doemer¹, Robert Rusnac¹, Rory Johnson², Mira Shah¹, Farzan Siddiqui¹, Parag Parikh¹, Benjamin Movsas¹, Kundan Thind¹

¹Henry Ford Health, Detroit, MI, USA. ²Siemens Medical Solutions USA, Cary, NC, USA

Abstract

Purpose

This study evaluates the initial performance of a newly installed low-field, large-bore MRI system and establishes clinical imaging protocols for radiotherapy across various anatomical sites.

Methods

The MAGNETOM Free.Max (Siemens Healthineers, Erlangen, Germany) is a 0.55 T MRI system with an 80 cm bore, enabling the use of immobilization devices during imaging in treatment positions. Acceptance and commissioning tests were performed following the recommendations of AAPM TG284 using vendor provided homogenous phantoms, the ACR Large Phantom, and a commercially available large field geometric distortion phantom (GRID phantom, Standard Imaging, Middleton, WI). Twenty-three healthy volunteers were scanned as part of an IRB-approved study to optimize clinical planning workflows for brain, head and neck, abdomen, and pelvis body sites. Brain scans were acquired with a dedicated 12-channel Head/Neck coil, while head and neck, abdomen, and pelvis scans utilized flexible BioMatrix Contour-L (6-channel), Contour-M (12-channel), and a 9-channel spine coil integrated into the patient table. Volunteers were immobilized using standard radiotherapy devices, including a 9-point thermoplastic mask for head and neck scans and Vac-Lok bags for abdomen and pelvis scans. Image quality was assessed by experienced radiation oncologists for clinical acceptability. Additionally, a stereotactic brain patient was scanned using a developed clinical protocol.

Results

All acceptance tests met AAPM TG-284 specified tolerances. ACR testing was performed verifying magnetic field drift, slice position accuracy, slice thickness accuracy, inter-slice RF interference, geometric accuracy, spatial resolution, and low contrast detectability. Residual gradient nonlinearity distortion after vendor 3D distortion corrections were applied was verified to be less than 1mm at 10 cm and 2mm at 20 cm from isocenter. Protocol scan times were less than 30 min for all sites. For the stereotactic patient, the brain protocol utilized consisted of an Axial T2-weighted turbo-spin echo sequence (TA= 4:57 min, TE/TR/α=116/8520ms/150°, pixel bandwidth = 100 Hz/pixel, and acquisition voxel=1.54 x1.15 x4.0 mm³), an Axial T2-weighted fluid attenuated turbo-spin sequence (TA= 6:13 min, TE/TR/TI=98/8500/2416 ms, pixel bandwidth =181 Hz/pixel, and acquisition voxel=0.89 x0.9 x4.0 mm³),

and post- contrast 3D, T1-weighted rapid gradient echo acquisition (TA= 6:41 min, TE/TR/ α =3.70/2080 ms/20°, pixel bandwidth = 150 Hz/pixel, and acquisition voxel=1.04 x1.04 x1.10 mm³). Both 2D acquisitions were acquired using Deep Resolve Boost, a CNN-based, deep learning reconstruction technique to accelerate acquisition time.

Conclusions

Optimized clinical protocols demonstrated high image quality using a low-field, large-bore MR simulator dedicated to radiotherapy. Protocols maintained scan times within 30 minutes, balancing patient comfort and compliance. The system's large bore, reduced susceptibility artifacts, lower safety barriers, and lower price compared to higher field strength units offer potential for widespread adoption in radiotherapy imaging workflows.

Internal Target Volume Estimation for Liver Cancer Radiation Therapy Using an Ultra Quality 4D MRI

Yen-Peng Liao¹, Haonan Xiao^{2,3}, Peilin Wang³, Tian Li³, Todd Aguilera¹, Justin Visak¹, Andrew Godley¹, You Zhang¹, Jin Cai³, Jie Deng¹

¹UT Southwestern Medical Center, Dallas, USA. ²Shandong Cancer Hospital, Shandong, China.

³The Hong Kong Polytechnic University, Hong Kong, China

Abstract

Purpose: To evaluate the clinical value of an ultra-quality four-dimensional magnetic resonance imaging (UQ 4D-MRI) technique for internal target volume (ITV) estimation in liver cancer radiation therapy. The technique uniquely maps motion information from low spatial resolution dynamic volumetric MRI onto high-resolution 3D MRI used for treatment planning, providing superior soft tissue contrast while maintaining accurate motion assessment.

Methods: The study validated the UQ 4D-MRI technique through both phantom and patient studies. For phantom validation, a ZEUS MR-guided-RT motion phantom was used to simulate respiratory motion with various amplitudes (5-15mm) and periods (4-12 seconds). The phantom study tested various displacement ranges to evaluate capability of the UQ 4D MRI technique in capturing motion trajectories across and beyond typical clinical ranges. For clinical validation, data from 13 liver cancer patients who received radiation therapy were analyzed. ITVs generated from UQ 4D-MRI (ITV_{4D} and ITV_{MIP}) were compared with conventional isotropic expansions (ITV_{2mm} and ITV_{5mm}) and those created using conventional 4D-CT (ITV_{CT}). Additionally, tumor motion measurements from UQ 4D-MRI were validated against single-slice 2D cine MRI for accuracy verification.

Results: The phantom studies showed a displacement measurement difference of less than 5% between UQ 4D-MRI and single-slice 2D cine MRI. In patient studies, the maximum superior-inferior displacements of the tumor on UQ 4D-MRI showed no significant difference compared to single-slice 2D cine imaging ($p = 0.985$). Both ITV_{4D} and ITV_{MIP} showed no significant differences compared with ITV_{CT} , with average volume differences of 5.8% ($p = 0.25$) and -1.3% ($p = 0.77$), respectively, demonstrating the technique's compatibility with current clinical standards. ITV_{2mm} and ITV_{5mm} significantly overestimated the volume by 31.1% ($p = 0.005$) and 124.3% ($p < 0.0001$) compared with ITV_{CT} , respectively.

Conclusions: UQ 4D-MRI enables accurate motion assessment for liver tumors, facilitating precise ITV delineation for radiation treatment planning using MR only. The technique can be readily implemented in clinical practice by adding just a one-minute dynamic scan to standard MR-simulation protocols. Despite variations in patients' respiratory patterns, UQ 4D-MRI excels at capturing tumor motion trajectories, potentially improving treatment planning accuracy and reducing margins in liver cancer radiation therapy. The method shows promise in streamlining the treatment planning workflow while maintaining clinical accuracy standards, particularly beneficial for MR-only simulation where CT simulation could be entirely omitted.

3D Wideband Late Gadolinium-Enhanced MRI for Radiotherapy of Ventricular Tachycardia: A Preliminary Study

Huiming Dong, Shu-Fu Shih, Fei Han, Robert Chin, Justin Hayase, Jason Bradfield, Arash Bedayat, J Paul Finn, Minsong Cao, Xiaodong Zhong

University of California, Los Angeles, Los Angeles, USA

Abstract

Purpose

Ventricular tachycardia (VT) is characterized by irregular or fast heart rhythm resulted from abnormal ventricular activation, carrying significant morbidity and mortality.

Cardiac stereotactic body radiotherapy (SBRT) is a promising treatment where VT-inducing scars are ablated with high doses. Treatment success relies on accurate target delineation, for which two-dimensional (2D) late gadolinium-enhanced (LGE) MRI helps identify scar tissues. However, images are often compromised by hyperintense artifacts resulted by implantable cardioverter devices (ICDs). Other 2D imaging limitations include thick slices, large slice gaps, and suboptimal spatial coverage, challenging radiotherapy planning. While wideband inversion recovery (WB-IR) pulses have been proposed to mitigate artifacts, 3D WB-LGE MRI has not been implemented or investigated for radiotherapy.

The goal of this study was to implement and investigate a 3D WB-LGE sequence for cardiac SBRT. Specifically, we aimed to (1) evaluate geometric distortion associated with the 3D WB-LGE sequence and (2) evaluate WB-IR for artifact mitigation in an ACR phantom and healthy participant.

Methods

The 3D WB-LGE technique was implemented using a 3D-GRE readout with ECG and respiratory navigator gating. The sequence applies a non-selective hyperbolic secant WB-IR pulse with a 4kHz bandwidth (vs. conventional 1.1kHz) to encompass the frequency shift of the heart resulted by ICDs to reduce hyperintense artifacts.

Imaging was performed at 1.5T (Sola, Siemens Healthineers, Forchheim, Germany). Imaging parameters were the same for phantom and in vivo experiments, including TE=1.25ms, TR=2.62ms, flip angle=20°, readout bandwidth=1395Hz/pixel, voxel size=1.5x1.5x2.5cm³, 40 k-space lines/RR interval, slice oversampling=40%. For comparison, the conventional protocol was also performed with the same imaging parameters except the narrowband IR pulse.

A MagPhan (MagPhanRT820, PhantomLaboratory, Greenwich, NY) was scanned without ICD using T1-MPRAGE and WB-LGE sequences to investigate the sequence-associated geometric distortion.

To evaluate artifact reduction, an ACR phantom was scanned with an ICD positioned near the phantom. Inversion time (TI) of 110ms was selected to null the phantom signal.

A healthy participant was imaged with an ICD placed near the heart, mimicking typical ICD locations in patients. 3D images were acquired in 4-chamber long-axis views. The free-breathing acquisition took approximately 5minutes. TI was 400ms.

Results

Geometric distortion of T1-MPRAGE and WB sequences was well within clinical tolerance (**Supporting Material Table 1**). The maximum distortion was -0.22mm and -0.62mm for T1-MPRAGE and WB-LGE at 200mm diameter spherical volume (DSV) respectively, and -0.15mm and -0.85mm at 350mm DSV respectively.

In the ACR phantom, the improved reduction of the ICD-induced artifacts was observed with the 3D WB sequence compared to the conventional narrowband sequence (**Supporting Material Figure 2a**).

In the health participant, comparing myocardium signal nulling between the WB and conventional sequences revealed improved artifact reduction with the WB sequence (**Supporting Material Figure 2b**).

Conclusion

A 3D WB-LGE sequence and protocol were implemented for stereotactic cardiac radioablation planning. MagPhan data showed clinically-acceptable geometric distortion. ACR phantom and healthy participant experiments demonstrated hyperintense artifact suppression. With future work validating the technique in VT patients and correlate treatment outcomes with target delineation, this 3D WB-LGE approach may improve treatment planning in cardiac SBRT of VT.

Feasibility of Longitudinal Relaxation Rate Mapping with Non-Cartesian Sampling and Compressed Sensing on a 1.5T MR-Linac

Lucas McCullum^{1,2}, Michael van Rijssel³, Ken-Pin Hwang⁴, Yao Ding⁵, Chad Tang⁶, Jinzhong Yang⁵, Peter Balter⁵, Jihong Wang⁵, Clifton Fuller¹, Ergys Subashi⁵

¹Department of Radiation Oncology, The University of Texas MD Anderson Cancer Center, Houston, USA. ²UTHealth Houston Graduate School of Biomedical Sciences, Houston, USA. ³Department of Radiotherapy, UMC Utrecht, Utrecht, Netherlands. ⁴Department of Imaging Physics, The University of Texas MD Anderson Cancer Center, Houston, USA. ⁵Department of Radiation Physics, The University of Texas MD Anderson Cancer Center, Houston, USA. ⁶Department of Genitourinary Radiation Oncology, The University of Texas MD Anderson Cancer Center, Houston, USA

Abstract

Purpose: The integrated MR-Linac (MRL) provides a novel platform for the delivery of precision MR-guided adaptive radiotherapy. While functional and metabolic imaging biomarkers are known to be predictors of malignancy and treatment response, the inclusion of these datasets in workflows for adaptive planning remains under investigation. Quantitative mapping of the longitudinal relaxation rate ($R_1=1/T_1$) is a major building block for several multiparametric MRI protocols. The implementation of these protocols is challenging in motion-sensitive anatomical sites. In this work, we investigate the feasibility of using non-cartesian k-space sampling and compressed sensing reconstruction for longitudinal relaxation rate mapping on a 1.5T MRL.

Materials: T1-mapping was implemented with the spoiled steady-state gradient-echo sequence using the variable-flip-angle method in two institutions using a 1.5T MRL. Bias and reproducibility were assessed in the NIST/ISMRM phantom, Eurospin II TO5 phantom, and healthy volunteers. The pseudo-randomized 3D radial and 3D stack-of-stars (SoS), each with half or full-spoke coverage were investigated. A Cartesian acquisition was included for benchmarking. The imaging parameters were: TR/TE=10/0.2 ms and 10/1.7 ms for half and full spoke respectively, FA={3°,20°}, FOV=25x25x25 cm³, acquisition voxel=2x2x2 mm³. The discrepancy between nominal and actual trajectories was estimated by varying gradient trajectory delays in the range 0-5 us. We analyzed the effect of regularization in the spatial, wavelet, Fourier, contrast, and joint domains across several regularization parameters and number of iterations. Total acquisition time was maintained within 5 mins. Repeat scans were acquired over five days to determine longitudinal bias and reproducibility. The analysis was constrained for T1 between 0-1500 ms. Reproducibility was assessed using the coefficient-of-variation (CoV), and Spearman's test was used to evaluate the correlation of bias with T1.

Results: Image artifacts due to gradient delay mismatches were minimized at 3 us. In the combined data from both institutions, bias and reproducibility were comparable across sampling methods. Median bias was less than 7.3% with respect to nominal values and 3.4% with respect to Cartesian values and reproducibility was within 8.7%, with minimal dependence on undersampling factor. Short term bias and

reproducibility over five days were within 3.1% and 4.4%, respectively. The correlation of bias with measured T1 was not significant. In volunteer scanning, T1 values in paravertebral muscle, kidney cortex/medulla, prostate, and parotids reveal a large bias and uncertainty in structures affected by motion artifacts as shown in Table 1. Figure 1 presents a representative dataset from the NIST/ISMRM phantom acquired with a 3D half-spoke radial sampling function and reconstructed with native algorithm or compressed sensing with L1-wavelet regularization in spatial and contrast domain. Figure 2 outlines the relationship between reconstruction, undersampling, and bias/reproducibility. In this dataset we find that undersampling up to 20x introduced negligible bias with improved CoV up to a factor of 2 in the NIST/ISMRM phantom vials.

Conclusion: In this work we implement and evaluate clinically feasible T1-mapping methods using clinically available non-Cartesian sampling on a 1.5T MR-Linac. The methods complement current protocols of quantitative MRI in anatomical regions with large physiological motion.

Quantifying longitudinal changes in tumor habitats during radiotherapy via multiparametric MRI in a murine glioma model: Preliminary results

Ayesha Das¹, David Hormuth¹, Jack Virostko^{1,2}, Thomas Yankeelov^{1,2,3}

¹University of Texas at Austin, Austin, USA. ²Dell Medical School, Austin, USA. ³MD Anderson Cancer Center, Houston, USA

Abstract

Introduction:

We have implemented an MRI protocol consisting of a dynamic contrast enhanced MRI (DCE-MRI) scan to estimate perfusion, a diffusion weighted MRI (DW-MRI) sequence to estimate cellularity, and an oxygen enhanced MRI (OE-MRI) scan to estimate hypoxia. We then applied clustering analysis to define "habitats"¹ within the tumor to quantify the changes in intra-tumoral heterogeneity in response to radiotherapy.

Methods:

MRI acquisition

A Bruker 7.0 T MRI system was used to collect DCE-MRI, DW-MRI, OE-MRI, and T_1 -mapping data on animals with C6 rat brain tumors ($n = 5$). Animals were imaged twice before the first dose of radiotherapy and then divided into a control group (0 Gy), and four treatment groups each receiving a total of 20 Gy over four schedules (i.e., 20 Gy divided into 1, 2, 3, or 4 fractions). Follow-up MRI data were obtained 72 hours after radiation. Figure 1 summarizes the experimental design, and all data analysis employed MATLAB.

MRI analysis

DCE-MRI data was collected using a gradient echo sequence ($TE/TR/a = 2.6\text{ ms}/90\text{ ms}/24^\circ$). The DCE-MRI data was analyzed by subtracting the pre-contrast images from the post-contrast images, ΔSI . Tumor regions of interest were identified on the post-contrast DCE signal intensity data.

DW-MRI data were analyzed to yield apparent diffusion coefficient (ADC) maps constructed from diffusion weighted spin echo data collected at b -values of 150, 300, 800 s/mm^2 .

OE-MRI data was collected using a gradient echo sequence ($TE/TR/a = 3.4\text{ ms}/11\text{ ms}/24^\circ$). This acquisition contain a gas challenge from air to oxygen to air with each section lasting 5 minutes. The OE-MRI scan data is summarized as the change in T_1 (ΔT_1) which is calculated as the average difference in T_1 value between oxygen and air inhalation.

T_1 maps were constructed from gradient echo images acquired at flip angles of 5° , 10° , 15° , 20° , and 45° .

Habitat Identification

Tumor voxels from all imaging sessions were combined to yield a multiparametric dataset, and the distributions for ΔT_1 , ADC , T_1 , and ΔSI were scaled to that the distributions had a mean of 0 standard deviation of 1. Habitats were then constructed using bootstrap k-means clustering on this scaled dataset.

Results

Figure 2A displays a heatmap of the identified habitats and normalized parameters. Each group includes a representation of animals and visits, indicating no bias from any single animal or visit. Figure 2B-2D describe the longitudinal changes in habitat composition in response to treatment stratified by radiotherapy schedule. At the end of the experiment, we observed that all animals receiving radiotherapy had a significantly higher ($p < 0.022$) percentage of voxels in the third habitat compared to the control group.

Discussion and Conclusion:

We have implemented a multiparametric MRI protocol to monitor changes in tumor habitats in response to radiotherapy. We observed that our quantitative MRI protocol effectively captured significant differences in tumor composition in response to variations in the radiotherapy schedule. Ongoing studies are seeking to integrate this dataset into a biologically based mathematical model to predict and optimized response to radiation.

